Active Photonic Crystal Waveguides

Ek, Sara

Publication date:
2012

Document Version
Publisher's PDF, also known as Version of record

Active Photonic Crystal Waveguides

Sara Ek

Technical University of Denmark

February 2012

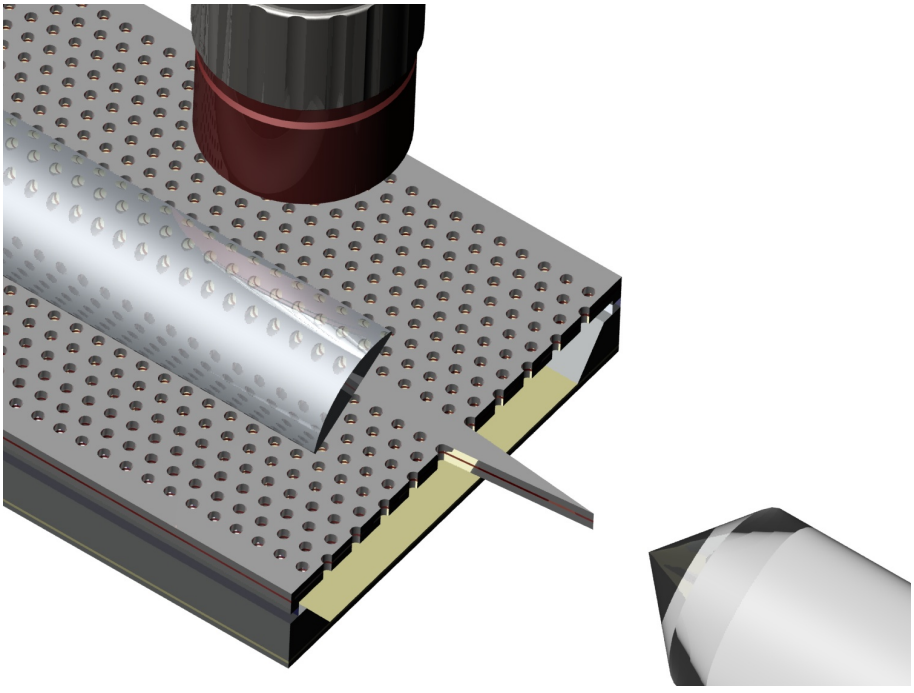

Abstract

This thesis deals with the fabrication and characterization of active photonic crystal waveguides, realized in III-V semiconductor material with embedded active layers.

The platform offering active photonic crystal waveguides has many potential applications. One of these is a compact photonic crystal semiconductor optical amplifier. As a step towards such a component, photonic crystal waveguides with a single quantum well, 10 quantum wells and three layers of quantum dots are fabricated and characterized. An experimental study of the amplified spontaneous emission and amplified transmission are presented in this thesis. A variation of photonic crystal design parameters are used leading to a spectral shift of the dispersion, it is verified that the observed effects shift accordingly. An enhancement of the amplified spontaneous emission was observed close to the band edge, where light is slowed down due to photonic crystal dispersion. The observations are explained by the enhancement of net gain by light slow down.

Another application based on active photonic crystal waveguides is micro lasers. Measurements on quantum dot micro laser cavities with different mirror configurations and photonic crystal designs are shown. Laser emission is observed at wavelengths corresponding to the slow light regions of the cavity mode, where the enhanced gain lead to lower lasing threshold.

Gain dynamics of the quantum dot gain material, used in both amplifier and laser structures, are investigated. The measurements are based on degenerate pump-probe transmission spectroscopy using $180fs$ pulses. The characteristic gain recovery times are measured to be $\sim 2ps$ and $\sim 0.2ps$, with little variation over a wavelength span of $260nm$. Sub-assemblies of quantum dots which vary in height by one monolayer are observed. No noticeable changes in carrier dynamics can be associated with dots of different number of monolayers.

Resumé

Denne PhD afhandling omhandler fremstilling og karakterisering af aktive fotoniske krystal bølgeledere, realiseret i III-V halvledermaterialer med indlejrede aktive lag.

Platformen, der muliggør aktive fotoniske krystal bølgeledere, har mange potentielle anvendelsesmuligheder. En af disse er en kompakt fotonisk krystal halvleder optisk forstærker. Som et skridt i retning af sådanen komponent, er der fabrikerat og karakteriserat fotoniske krystal bølgeledere med en enkelt kvantebrønd, 10 kvantebrønde og tre lag af kvantepunkter. En eksperimentel undersøgelse af den forstærkede spontane emission og forstærkede transmission præsenteres i denne afhandling. Variationer af fotoniske krystal fabrikationsparametre anvendes og fører til en spektral forskydning af dispersionen, og det bliver verificeret, at de observerede effekter skifter som følge heraf. En forstærkning af den amplificerede spontane emission blev observeret tæt ved båndkanten, hvor lyset bliver langsommere på grund af dispersionen i det fotonisk krystal. Observationerne er forklaret ved forstærkning af netto-gainet ved langsomt lys.

En anden anvendelse der er baseret på aktive fotoniske krystal bølgeledere, er mikro-lasere. Målinger på kvantepunkt mikro-laserkaviteter med forskellige spejlkonfigurationer og fotoniske krystal design er præsenteret. Laseremission iagttages ved de bølgelængder, der svarer til langsomt lys i kavitets-tilstanden, hvor en forstærkning af gainet fører til lavere tærskel-verdier.

Ultra hurtig dynamik af forstærkningen af kvantepunkt materialet, der anvendes i både forstærker og laser strukturer, undersøges. Målingerne er baseret på degenererede pumpe-probe transmission spektroskopi med $180fs$ pulser. De karakteristiske relaksationstider er målt til at være $\sim 2ps$ og $\sim 0.2ps$, med lille variation over et bølgelængde interval på $260nm$. Under-grupperinger af kvantepunkter, som varierer i højden med et monolag er observeret. Ingen mærkbare ændringer i ladningsbærer-dynamiken forbundet med kvante punkternes forskellige højder er observeret.

Acknowledgements

Many people have contributed to the work presented in this thesis. I would like to start with a special thank you to my supervisors Professor Jesper Mørk, Associate Professor Kresten Yvind, and postdoc Per Lunnemann for encouragement and guidance. Our numerous discussions have been very educational and invaluable for this work. I am grateful to Per Lunnemann (alias "the laser whisperer") for his efforts to transfer his pump-probe experimental skills to me. I also thank Professor Jørn Hvam for the many fruitful discussions.

I highly appreciate the nice collaboration with Alfredo De Rossi, Sylvain Combrié and Pierre Colman at Thales Research and Technology, France. The visits to your laboratory have been as pleasant as productive. I am also thankful that you shared your taper design with me, which have improved the performance of my devices.

I have been fortunate to collaborate with many talented colleagues in different parts of the project; Martin Schubert and Luisa Ottaviano in cleanroom processing, Jin Liu in characterization of localized lasing modes, Yaohui Chen provided theoretical insights in the physics of the devices and Fengwen Wang contributed with topology optimized designs. I am in particular thankful for all the wafers, grown by Elizaveta Semenova and Kresten Yvind.

The nice working environment on DTU with many inspiring people makes it an enjoyable place to work. There are many people who have put a silver lining on my past three years at DTU, both through professional collaborations and friendships. It has truly been a joy to share office with Thor Ansbæk, Róza Shirazi, Troels Shur and Andrei Andryieuski. The nice atmosphere where the smallest achievements were big enough to celebrate with a cake meant a great deal to me.

I would also like to express my gratitude to family and friends for their love and support. Especially to my personal coach and boyfriend who have boosted me with energy and motivation in a loving and effective way throughout the project.

Publications

Journal Publications

- M. Schubert, T. Suhr, S. Ek, E. Semenova, J. M. Hvam, and K. Yvind. *Lambda shifted photonic crystal cavity laser*, Applied Physics Letters, **97**, 191109 (2010).
- P. Lunnemann, S. Ek, K. Yvind, R. Piron, and J. Mørk. *Nonlinear carrier dynamics in a quantum dash optical amplifier*, New Journal of Physics, **14**, 013042 (2012).
- S. Ek, P. Lunnemann, K. Yvind, and J. Mørk *Slow light enhanced net gain in photonic crystal amplifiers* , *Under preparation.*
- J. Liu, S. Ek, T. Suhr, M. Schubert, P. D. Garcia, H. Thyrrestrup, S. Stobbe J. Mørk and P. Lodahl. *Slow light controlled microcavity random lasing in photonic crystal waveguides*, *Under preparation.*

Conference Proceedings

- S. Ek, M. Schubert, K. Yvind, and J. Mørk,*Enhanced amplified spontaneous emission in III-V semiconductor photonic crystal waveguides*, Integrated Photonics Research (IPR), 2010, Monterey, CA, USA
- M. Schubert, T. Suhr Skovgård, S. Ek, E. Semenova, J. M. Hvam, and K. Yvind, *Quarter-lambda-shifted photonic crystal lasers*, International Semiconductor laser Conference (ISLC), 2010, Kyoto, Japan
- S. Ek, Y. Chen, M. Schubert, E. Semenova, P. Lunnemann, K. Yvind, and J. Mørk, *Active III-V Semiconductor Photonic Crystal Waveguides*, 13'th International Conference on Transparent Optical Networks (ICTON), 2011, Stockholm, Sweden
- Y. Chen, F. Wang, S. Ek, J. S. Jensen, O. Sigmund, and J. Mørk, *Modelling of Active Semiconductor Photonic Crystal*

Waveguides and Robust Designs based on Topology Optimization, 13'th International Conference on Transparent Optical Networks (ICTON), 2011, Stockholm, Sweden

- S. Ek, P. Lunnemann, E. Semenova, K. Yvind, and J. Mørk, *Enhanced Gain in Slow-Light Photonic Crystal Waveguides with Embedded Quantum Dots*, International Quantum Electronics Conference / Conference on Lasers and Electro-Optics (IQEC/CLEO) Pacific Rim, 2011, Sydney, Australia
- S. Ek, Y. Chen, E. Semenova, P. Lunnemann, K. Yvind, and J. Mørk, *Slow-light enhancement of spontaneous emission in active photonic crystal waveguides*, SPIE Photonics West, 2012, San Fransisco, CA, USA

Book Chapters

- N. Gregersen, T. Suhr, S. Ek, W. Xue, I. Chung, and J. Mørk, *The optical chip : high speed and diminutive size*, Beyond optical horizons : today and tomorrow with photonics, 2009, DTU, pp. 235-249
- S. Ek *We can fabricate and image nano-sized structures!*, Beyond optical horizons : today and tomorrow with photonics, 2009, pp. 250

Contents

Chapter 1

Introduction

1.1 Ultrafast communications

There is an ongoing race to increase the speed of devices and systems used in communication networks. In ten to twenty years from now the conventional techniques will fail to scale the capacity to meet the operating speed (i.e. bandwidth) demands [1]. The ever increasing amounts of internet traffic at higher data rates call for basic research in wideband optical components, because if only a few functions could be done optically instead of electronically there would be much to gain in terms of bandwidth. It will be necessary to process signals in terabit per second regime and photons are better candidates than electrons to represent and transmit data at such high rates. Most information is already represented by light pulses, transmitted through low loss optical fibres with large bandwidth. However, the full bandwidth is not utilized today. One bottleneck is the numerous electro-optical conversions required, since most operations performed on the signal are done using electronics. Recent progress in communication systems has led to more complex architects with many components, each component performing only one specific function. As a result such systems require large storage areas and demands huge amounts of energy. Only to cool the racks of electronics demands huge amounts of energy, hence server farms are often built at geographical locations with cold climate.

Photonic integrated chips have been a hot research topic for many years, striving to create an optical equivalent to the silicon electronic chip. Integration is desired on order to reduce the power consumption and footprint area. It remains to be seen if fundamental functionalities for signal processing in the terabit per second data rate can be realized. One promising platform for photonic integrated chips is photonic crystals [2].

1.2 Photonic Crystals

Photonic crystals (PhCs) have the potential of integrating several different functionalities on the same lattice; such as lasers, amplifiers and switches. Even though it might sound contradictive, one of the key properties which brings PhC to the top of the candidate list for the realization of ultra-fast optical devices, is its ability to slow down light.

1.2.1 Brief Historical Background

During the past century, the interaction of electromagnetic waves with periodic media have been studied. During the first years of the 18'th century theoretical and experimental reports were communicated by Lord Rayleigh and Wood respectively [3, 4]. Around the same time Bragg demonstrated that the diffraction pattern from a periodic media may be explained by single and multiple scattering events [5]. Following these reports, multi-layered films received intense study. The concept of photonic crystal was first introduced by Othaka in 1979 [6], and the impact of photonic band gap materials were discussed theoretically by Yablonovitch and John [7, 8]. A number of natural photonic crystals exist; the iridescent colour of the opal gemstone, the eye of the peacock feather and the wing-scales of the Morpho butterfly arise from a periodic nano-structure of the material [9, 10, 11]. Despite the absence of pigments they all exhibit striking colour effects. Lightwaves in a structural periodic material experience a periodic perturbation from the structure causing them to behave very different compared to lightwaves in an

homogeneous media. This situation is analogous to electrons in a semiconductor crystal, which due to the interaction with the periodic potential are confined to certain energy bands and are forbidden to occur at a certain range of energies. This analogy suggests that the dispersion of lightwaves in a photonic crystal should be described in terms of a (photonic) band structure, just like electronic bands in condensed matter physics. One important consequence of the band formation in photonic crystals is the appearance of a photonic band gap (PBG), which forbids propagation of certain frequencies of light.

Experimental demonstrations of photonic crystals had at first band gaps for micro wavelengths [12]. A PhC for microwave control has millimeter dimensions, while a crystal for infrared waves require micrometer dimensions. The design of the PhC may be scaled to tune the bandgap region to desired wavelength. As the dimensions decrease, the demands on high resolution fabrication technology increase. The first PhC with sharp band edges for telecommunication wavelengths was demonstrated by Krauss in 1996 [13]. Their fabrication was based on semiconductor processing, making the technology assessable for other laboratories. There are several advantages in creating PhC devices out of semiconductor materials. First, a strongly modulated crystal can be created. By etching air-holes into a high refractive index semiconductor material ($n > 3$) a refractive index ratio of at least 2 is achieved, which is a requirement to obtain 2D or 3D PBGs [14, 15]. Secondly, it is possible to use direct band gap semiconductors which could be manipulated to emit light at a wavelength within the photonic band gap of the PhC. It enables experimental verification of Yablonovitch's original idea; that it should be possible to control the spontaneous emission in a PhC. It has been demonstrated that there is a modification in the spontaneous emission decay time [16], originating from the Purcell effect. In this work we show experimentally that also the output intensity of the amplified spontaneous emission in a PhC waveguide is enhanced due to the PhC.

1.2.2 Types of Photonic Crystals

PhCs may be one, two or three dimensional. A quarter wave stack of alternating layers of different dielectric materials is an example of one dimensional PhC. An incoming wave at the Bragg wavelength will be partly reflected at each interface. At each low-to-high index interface the light will be phase shifted 180 degrees, compared to at the high-to-low interface. This leads to constructive interference; the total reflection depends on the number of dielectric layers. This low loss dielectric mirror has proven to be incredible useful in many devices, for example as dielectric Fabry-Perót filters and in distributed feedback lasers. The main limitation is it only reflects light at normal incidence to the layer stack. In order to fully confine light of all polarizations and in any direction the PhC needs to be extended into all three dimensions. With proper design and with sufficient refractive index contrast it is possible to achieve a complete PBG, but it is a challenging task. Many efforts have been made to achieve a 3D PhC; such as stacking two dimensional slabs of PhC on top of one another [17], or creating a "woodpile" structure by layer-by-layer lithography [18]. Neither of the methods are suitable for large scale production. One of the most promising methods to fabricate 3D PhC is by using self-assembly to create a colloidal crystal, also named artificial opal. Monodisperse microspheres made of polystyrene or silica tend to self assemble in an ordered face-centred cubic structure in proper environment. Complete PBG has been achieved by infiltrating a silica opal matrix with silicon and subsequently removing the silica spheres with a Fluoride-based etch [19]. Other materials which do not require chemical vapour deposition can be used, such as sol-gel, to create a partial band gap inverse opal. Scanning Electron Microscope (SEM) images of a polystyrene opal, and a sol-gel inverse opal can be seen in Figure 1.1. Figure 1.1 a) shows a photo taken of two polystyrene opals when illuminated with white light. Only light with a frequency within the partial PBG is reflected, while the light at other frequencies are transmitted. If the sphere size is chosen so that the PBG falls within the visible part of the spectra, the opal shows brilliant colour effects when viewed in the normal direction.

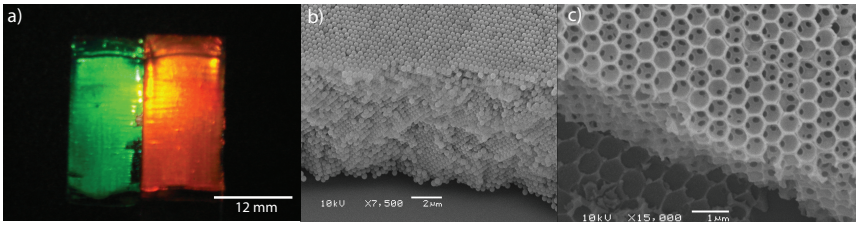

Figure 1.1: a)Photo taken under white light illumination of two polystyrene opals created on microscope slides. To the left: sphere size 270 nm. To the right: sphere size 240 nm. b) SEM image of a polystyrene opal. Showing the long range order also in the third dimension, a thickness of about 20μm achieved in a single growth. c) Sol-gel inverse opal. [20]

1.2.3 Functional Photonic Crystal Membranes

In this work the devices are 3D but with a PhCs band gap in only two dimensions, their partial PBG covers only a limited range of directions for a certain polarization. Though, with appropriate design this partial PBG can function in a very similar way to a complete PBG. From now on it will be referred to simply as PBG. An hexagonal array of holes are defined in a slab of semiconductor material. The reason for choosing an hexagonal lattice is because it has the largest 2D PBG in TE-polarization (the electric polarization parallel to the 2D plane) [21]. If intentional defects are introduced in the PhC lattice, then many different functional devices may be built from this platform, such as lasers, switches and amplifiers. Defects, such as missing holes, may allow localized modes to exist, with frequencies inside the PBG, see Figure 1.2. The denotations "dielectric band" and "air band" on the low and high frequency side of the band gap respectively will be further explained in Section 2.1.1.

If one hole is removed from the lattice a cavity with reflective walls is created. The localized mode cannot escape from the defect because it has a frequency within the gap, which is prohibited to propagate through the crystal. The defect mode decays exponentially away from the defect, and is localized in two dimensions while it extends

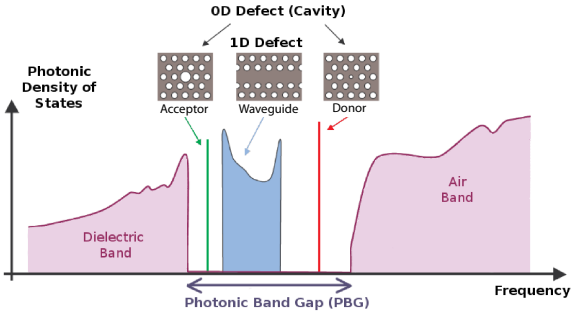

Figure 1.2: A schematic drawing of the photonic density of states (DOS) for a PhC. Defects such as waveguides or cavities creates modes within the PBG which are very well confined [22].

in the z-direction. Besides from resonators, waveguides may be created by removing a row of holes, see Figure 1.3. Also a line defect mode has its frequency inside the PBG. Light can therefore not leak out into the surrounding band gap material. However, in the third dimension (out-of-plane) the guiding mechanism is the same as for conventional waveguides (for example fibers or ridge waveguides), where the light is confined only if the law of total internal reflection (TIR) is obeyed. When light in a high index material strikes the interface of a low index material, light might be transmitted or reflected depending on the incident angle. If the angle is greater than the critical angle, all light is reflected back into the waveguide. The critical angle depends on indices of refraction of the two materials according to Snell's law of refraction. For optimal vertical confinement the 2D PhC is implemented in a membrane surrounded by air. All modes in a PBG are gap guided [23]. It enables low loss transmission through sharp bends; a feature desired for guiding light between a dense network of devices on an optical chip.

The 2D membrane PhC's have several advantages over current 3D PhC's, in which it is challenging to incorporate linear waveguides or other defects with good accuracy. In the membrane PhC's presented in this work, functionalities may be included without additional fabrication steps and the PhC pattern can be freely designed with high resolution. It is a limitation that light will suffer out-of plane radiation loss if TIR is not fulfilled, but the high refractive

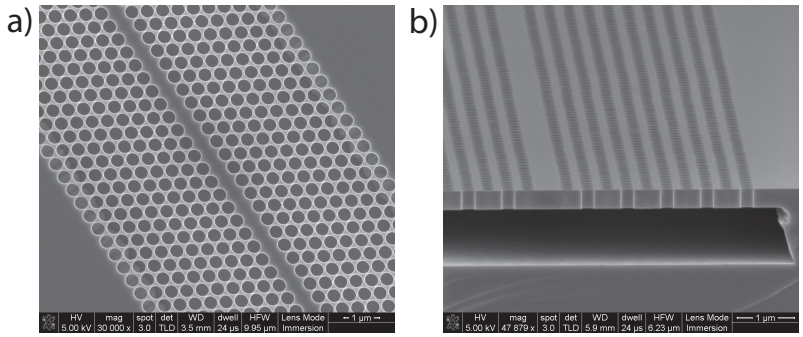

Figure 1.3: SEM image of 2D membrane PhC. a) Top view showing the linear waveguide defect. b) Sideview of a cleaved facet showing the free-standing membrane surrounded by air, for efficient confinement in the third dimension.

index ratio in air-membranes ensures that the guided mode covers a broad range of frequencies, which is required for processing of ultra short optical signals.

1.3 At the Speed of Light

The speed of light in vacuum, c, is approximately 3×10^8 m/s. When light propagates through a transparent material it is slowed down. The ratio by which it is slowed down is the refractive index of the material, n. The speed of light through all materials except for vacuum is wavelength dependent, which in turn means the refractive index is wavelength dependent.

When waves propagate through a material, they will interfere with one another. Consider two plane waves with the same amplitude but different frequencies, the sum of the two will be [24]:

$$E_1(t) + E_2(t) = Asin(\omega_1 t - k_1 x) + Asin(\omega_2 t - k_2 x) \quad (1.1)$$

$$= 2Acos(\frac{\omega_1 - \omega_2}{2} t - \frac{k_1 - k_2}{2} x) sin(\frac{\omega_1 + \omega_2}{2} t - \frac{k_1 + k_2}{2} x) \quad (1.2)$$

The mean values and differences in angular frequencies (ω) and

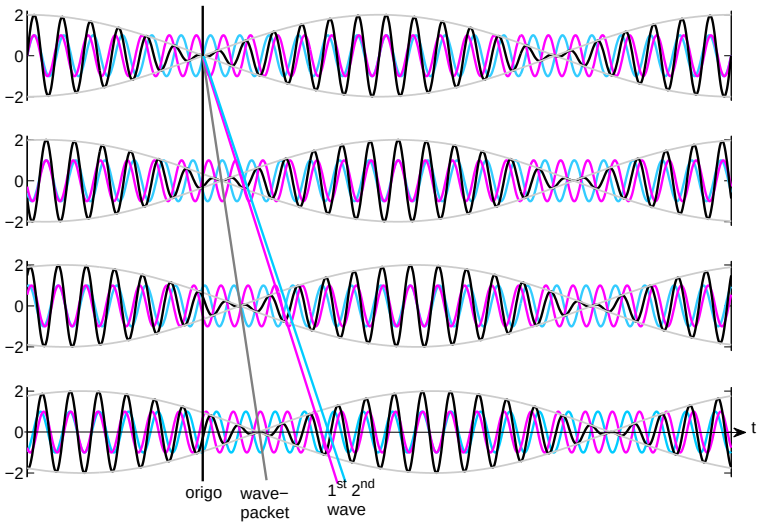

Figure 1.4: Two waves (blue and pink) with the same amplitude and almost the same frequency is propagating through a dispersive material. Due to interference, a beat frequency (black) is created. The velocity at which the beat frequency propagates is the phase velocity v_p. The velocity of the wave-packet (envelope of the beat frequency) is described by the group velocity v_g.

wavevectors (k) between the two waves are expressed as

$$\omega = \frac{\omega_1 + \omega_2}{2} \qquad k = \frac{k_1 + k_2}{2} \tag{1.3}$$

$$\Delta\omega = \frac{\omega_1 - \omega_2}{2} \qquad \Delta k = \frac{k_1 - k_2}{2} \tag{1.4}$$

If two waves are almost in phase with on another, their frequencies are only slightly shifted with respect to each other ($f_1 \approx f_2$). Then the interference can be written as

$$E_1(t) + E_2(t) = y(t)sin(\omega t + kx) \tag{1.5}$$

This can be interpreted as the beating having a frequency corresponding to the mean of the two waves, and its propagation speed is $v_p = \omega/k$. This is the phase velocity of light. The beat frequency is represented by the black curve in Figure 1.4. The amplitude modulation of the beating is described by

$$y(t) = 2Acos(\Delta\omega t - \Delta kx) \tag{1.6}$$

The amplitude modulation is also a wave with a frequency very different from f_1 and f_2, namely the beating frequency. The velocity at which the envelope of the beat frequency propagates is called the group velocity

$$v_g = \Delta\omega/\Delta k = \delta\omega/\delta k. \tag{1.7}$$

It may be rewritten as:

$$v_g = v_p - \lambda\frac{\delta v_p}{\delta\lambda} = \frac{1}{n + \omega(\delta n/\delta\omega)} \tag{1.8}$$

The first equality then clearly shows that v_g=v_p in a non-dispersive material.

If light is propagating in a dispersive material (where the propagation velocity depends on the wavelength), we need to keep track of several different velocities. If the group velocity v_g is measured experimentally, it is not the velocity of an individual wave but rather the energy distribution of a wave-packet which is measured, see Figure 1.4.

1.3.1 Slow Light in Photonic Crystals

As discussed earlier the fastest way to transfer information is at the speed of light, for a number of applications it is an advantage to be able to slow down light. Slow light is expected to enhance the functionality in devices such as switches, optical delay lines, all-optical storage [25] and amplifiers [26]. Group velocity reduction leads to pulse compression and an enhancement of linear and non-linear effects are expected [27, 28].

Optical resonances within a material or a periodic structure causes large first order dispersion [27]. It has been known since 2001 that a slow group velocity can be achieved in a PhC waveguide [29, 30]. An impressive 300-fold retardation of the group velocity has been demonstrated experimentally using an unbalanced Mach-Zehnder interferometer [31]. The slow down of light occurs at the band-edge of the guided mode, as further discussed in Section 2.1.

The research topic of slow light has attract a lot of attention the past decade. In 1999 Hau et al. were able to slow down light to the

speed of a bicycle, $17ms^{-1}$ [32]. The experiment was performed in ultracold gas of sodium atoms; an opaque medium which can be made transparent using electromagnetically induced transparency (EIT). EIT has also been observed in semiconductors [33], but its observation is very difficult due to both inhomogeneous and homogeneous broadening effects in semiconductors. The key advantage of PhC slow light has over other slowdown effects, such as (EIT) is that it is broadband, which is required for processing of ultra short optical signals and it is also possible to freely tune the wavelength because of its dependency on the structural geometry rather than a material resonance.

1.4 Semiconductors

III-V semiconductors have become the basis for many commercial optoelectronic devices, such as diode lasers, light-emitting diodes, and photodetectors only to mention a few. They have a direct band gap, making their optoelectronic properties more favourable than in-direct band gap semiconductors such as silicon. By definition, the valence band of a semiconductor is entirely filled, and there are no free electrons in the conduction band, at $T = 0K$ if no external field is applied. Electrons may be promoted to the conduction band if externally excited. Let us consider optical excitation; if an incident photon has an optical energy above the gap, it will be absorbed. An electron will be excited from the valence band to the conduction band, leaving a hole behind. Both the electron and the hole can now contribute to conduction. The kinetic energy of the excited electron, the energy above the conduction band edge, may be transferred into heat (phonon-phonon scattering) as the electron relaxes down towards the band edge of the conduction band. The recombination of an excited electron with a hole in the valence band can be a radiative, or a non-radiative process. In a radiative recombination, a photon will be emitted. The transition may occur in absence of a perturbing external electromagnetic field; which is denoted spontaneous emission. The transition may also be triggered by a photon propagating in the semiconductor which results in stimulated emission (SE). The photon created through stimu-

lated emission will have the same phase, energy, polarization and direction of propagation as the photon stimulating the transition [34]. Amplified spontaneous emission (ASE) is spontaneously emitted light, which is amplified by stimulated emission as it propagates through a gain medium. The three scenarios; excitation, spontaneous emission and stimulated emission are illustrated in Figure 1.5 a)-c). In a non-radiative recombination the conduction band

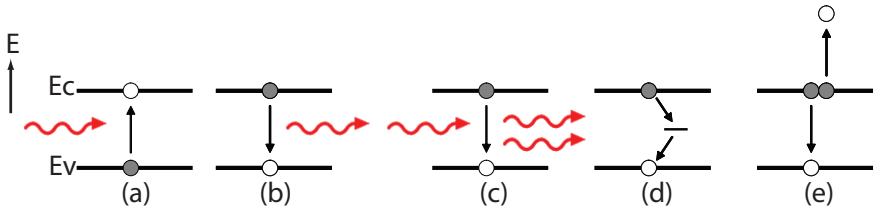

Figure 1.5: Electronic transitions between the conduction and valence bands. Open circles represent unfilled states (holes) and solid circles represent filled states (electrons). The red arrows symbolise photons. a) excitation, b) spontaneous emission, c) stimulated emission, d) surface recombination, e) Auger recombination. Inspired by a figure in [34].

electrons escapes from usefully contributing to the gain. Such process does not generate any photons, the energy is instead dissipated as heat in the semiconductor crystal lattice. There are two main non-radiative recombination schemes, as illustrated in Figure 1.5 d)-e). The first scheme depicts an energy level in the middle of the gap, which temporary traps the electron from the conduction band before releasing it to the valence band. Such an energy level can arise do to point defects or impurities in the crystal lattice. However, in modern crystal growth technologies the density of impurity atoms is very low which in turn means negligible impurity recombination rates [34]. The energy levels within the gap can also be associated with surface states in the crystal. Electron recombination via surface states results in a non-radiative transition denoted surface recombination. Surface recombination does not require an electron-hole pair, so the recombination rate is directly proportional to the carrier density. It is known that dry etching cause near-surface lattice damage which increase surface recombination rates [35], one should therefore avoid etching through the active layers of the device. Unfortunately, the total area of etched surfaces is

large in all the devices presented in this work, because the active layers are located in the center of the PhC membrane. Surface recombination is therefore and important loss-factor. The surface recombination velocity can be reduced by surface passivation [36], a permanent passivation of PhC membranes would improve device performance. The last non-radiative transition illustrated in Figure 1.5 e) is Auger recombination. The recombination energy does not generate a photon, but is given as kinetic energy to another electron or hole. Auger recombination increase with carrier density, because it depend on carriers colliding with one another.

Unless the excitation energy is very high, electrons are dominantly excited to energy levels close to the band edge. Therefore, the optical energy of the emitted photon is typically only slightly larger than the band gap energy. The technologies in crystal growth, such as metalorganic vapour phase epitax (MOVPE), makes it possible to engineer the band gap. The red line in Figure 1.6 shows the band gap energies achievable by creating InGaAsP quartinary alloys lattice matched to the binary compound InP. As the diagram shows, the band gap energy of InGaAsP alloys match well with the wavelength corresponding to low loss transmission in optical fibres ($1.55\mu m$), making it a good material choice for optical communication applications.

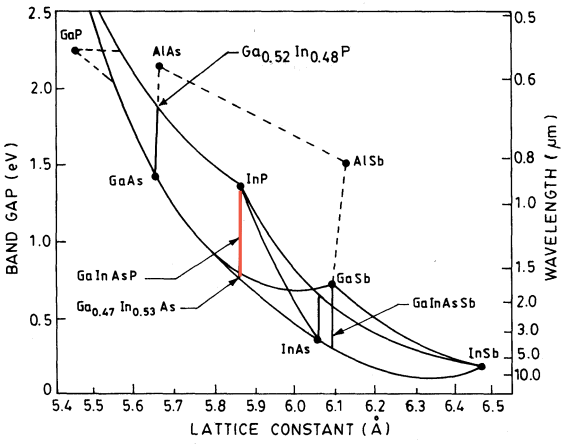

Figure 1.6: Bandgap vs. lattice constant for III-V compounds. The red line indicate the quaternary alloys, InGaAsP, lattice matched to InP [34].

1.4.1 Quantum Confinement

If the physical dimensions of the material are smaller than the coherent length of the conduction band electrons, quantum confinement effects occur [37]. A two-dimensional confinement can be accomplished by growing a quantum well (QW), which is a thin layer $(5 - 10nm)$ of a narrow band gap material sandwiched in between wider band gap material. Carriers are confined in a QW potential in discrete energy levels, similar to the classic particle in a box example. In a narrow well the electron wave function penetrates deeper into the barrier, leading to a higher energy of the quantized state. Hence, the transition energy of the lowest quantized states depend on the well thickness as illustrated in Figure 1.7. QWs have

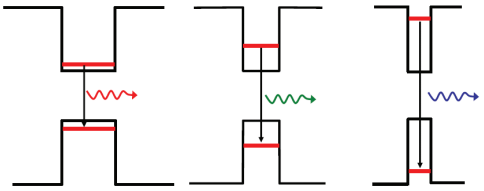

Figure 1.7: A simple illustration of QWs of different thickness. The energy separation of the quantized states is larger for a narrow well, leading to a shorter emission wavelength.

become an important gain material as they are more easily inverted than bulk material and the emission wavelength can be precisely tuned by altering their size [34]. The performance of the QW gain material can be improved further by introducing a strain in the well material. A small lattice mismatch in relation to the bulk material is tolerated up to a certain thickness, without introducing defects. Typically 1% mismatch is tolerable for a thickness less than $20nm$ [34]. Strained wells in lasers can reduce the lasing threshold to lower energies. An external force on a crystal lattice will cause distortion. The strain causes a splitting between the light-hole and the heavy hole band. The heavy-hole band rises relatively to the light-hole band and as a result, non-radiative recombinations are reduced.

Also 3D quantum confinement can be achieved by manipulating the crystal lattice. If a material, which is lattice mismatched to the substrate (for example InAs, lattice mismatched 3% relative

InP), is grown beyond the critical thickness, the induced strain will cause the lattice to break. Islands, quantum dots (QD), of material are formed on top of a ∼2 monolayer wetting layer [38]. The dots composition and size determines their band gap energy. As for the QWs; a smaller dot splits the energy levels more due to the quantum confinement effect, resulting in shorter wavelength emission. The formation of the dots is a statistical process, which leads to a distribution in dot sizes; $10 - 20nm$ wide and $3 - 5nm$ high. The different dot sizes result in an inhomogeneous broadened photo luminescence spectrum [39].

The electronic density of states (DOS) in QWs and QDs are different from that of bulk. For bulk material the energy states are so closely spaced they can be treated as a continuum of states. The bulk DOS forms an envelope for the steps of discrete energy levels which can be occupied with electrons in the QW case, see Figure 1.8. Each energy level in a QD can only occupied by 2 electrons (spin up and spin down electron). The density of states is therefore described by a Dirac delta function, indicated in green in Figure 1.8.

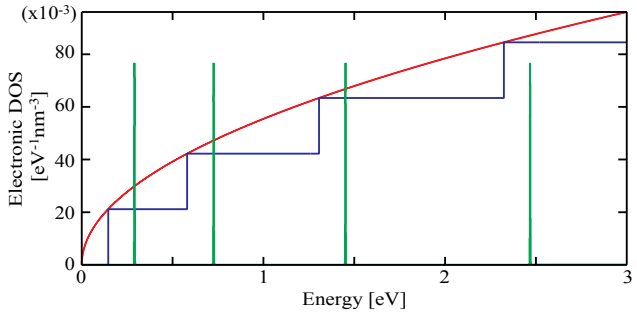

Figure 1.8: Electronic density of states for semiconductors of 3, 2, and 0 degrees of freedom, referred to as bulk (red), QW (blue) and QD (green) respectively. *Figure by courtesy of Troels Shur.*

1.5 Photonic Crystal Amplifiers

Slow light has been an active topic of research for the last decade, both due to fundamental interest in understanding light-matter interactions as well exploiting these effects for improving the performance of photonic devices or realizing new functionalities. Photonic crystal (PhC) line defect waveguides constitute an interesting platform for exploiting slow light effects and much work has been performed on passive waveguide structures [25, 31, 40, 41, 42].

When including layers of QWs or QDs in the PhC membrane slab one can control both the optical and electronic properties in an active PhC waveguide. By exploiting the slow light effect in active PhC waveguides, it has been suggested that an efficient, ultra compact semiconductor optical amplifier (SOA) can be achieved [26]. The device length can be drastically decreased compared to conventional ridge SOAs due to slow light enhanced light-matter interaction [27]. Such a device is desired for compact photonic chips and interconnects, e.g. for chip-to-chip or board-to-board links. Optical amplification is essential on a photonic integrated chip. By compensating for the attenuation more functionalities can be included. PhC amplifiers have proven challenging to realize experimentally and to the best of our knowledge there are no experimental demonstrations of gain in broad band PhC amplifiers. There are only few contributions in the literature on the study of the amplified SE from active PhC devices; in reference [43] investigations were carried out on highly multimoded waveguides with three rows of missing holes, not suitable for high-speed operation, and Raineri et al. presents optical amplification within a resonance whose quality factor is $Q \sim 1200$ [44]. In this work enhanced net gain in PhC amplifiers is demonstrated, the enhancement is shown to correlate well with the increase of the group refractive index due to light slow down. The devices have nearly zero input and output reflection coefficients and we emphasize that we focus on the output light intensity rather than the modification of the spontaneous emission decay time originating from the Purcell effect [16].

There are many demonstrations of lasing in photonic crystal structures [45, 46, 47], but most of them rely on the realization of a high-Q cavity in order to achieve lasing at a small net gain. There

are only a few contributions in the literature, where lasing is explained by gain enhancement at low group velocities [48, 49, 50].

1.6 Outline

In Chapter 2 the dispersion diagram for the PhC is presented and the important parameters for PhC design are highlighted. Calculations of the influence of slow light on transmission and ASE are presented followed by considerations for efficient optical pumping of the structures. In Chapter 3 the process for fabricating active InGaAsP PhC waveguides is presented. Chapter 4 contains the main experimental results on slow light enhanced gain and ASE in PhC amplifiers. Results on fabrication of topology optimized PhC waveguides and micro-lasers along with optical characterization of the lasers are presented in Chapter 5. In Chapter 6 pump-probe measurements of a ridge QD SOA are shown followed by a discussion of the ultrafast gain dynamics of the QDs, used in the amplifier and laser devices. Chapter 7 concludes the work and provides suggestions for future work. The parts which are done in collaboration with others are stated in the text.

Chapter 2

Photonic Crystal Amplifiers: Theory and Design

The intricate confinement of light in PhC waveguides result in a strong dispersion. With an understanding of how the structural parameters effects the propagating modes, the dispersion properties can be designed and optimized for each application. By reducing the lattice constant or increasing the hole diameter the mode can be shifted to shorter wavelengths. These scaling properties of PhCs allow fine-tuning of the slow light wavelength region which is valuable for active PhC waveguides. Light matter interaction can be enhanced by slow light propagation cite [27, 51], why an overlap between the wavelength for slow light and material gain is desired. There is also a freedom to tune the material gain, through material composition and QW thickness, to desired wavelength. For telecommunication applications, devices operating around 1550 nm are of interest because that wavelength region has shown lowest fibre loss transmission through optical fibres. Simple estimates of the drastic effect the slow light factor has on transmission and ASE in a semiconductor optical amplifiers are presented in Section 2.2, followed by challenges to overcome to achieve population inversion experimentally.

2.1 Design of Photonic Crystal Waveguides

Eigenstates of light in a transparent, uniform medium are described by the photon energy, wave vector and polarization state. Each eigenstate is specified by a mode, which is a plane wave for uniform media. The dispersion relation is a relation between the photon frequency (ω) and the wave vector ($\mathbf{k}$). In vacuum, the velocity of light is the same independent of photon energy and wave vector, leading to a linear dispersion relation; $\omega = c\mathbf{k}$. A photonic crystal has a periodic variation of the dielectric constant $\varepsilon(r) = \varepsilon(r + R)$, where $R = na_1 + ma_2 + la_3$ is a linear combination of the real lattice vectors (a_1, a_2, a_3) and (n, m, l) are integers. The periodicity leads to a modification of the eigenstates. Light which enters such a periodic material need to be described by a periodic eigenfunction and not by a pure plane wave. Using Bloch's theorem the electric and magnetic fields are written [52]:

$$E_k(r) = e^{i\mathbf{k}\cdot\mathbf{r}}u_k(r) \tag{2.1}$$

$$H_k(r) = e^{i\mathbf{k}\cdot\mathbf{r}}u_k(r) \tag{2.2}$$

where $u_k(r) = u_k(r+R)$ are the periodic Bloch eigenfunctions with the same periodicity as the dielectric function. At each k-point (Bloch wave vector), a discrete set of eigenstates exists. The eigenstates form bands, because $\mathbf{k}$ is a continuous variable. These photonic bands of the structure are calculated using Maxwell's equations. The periodicity of a photonic crystal greatly reduces the computational effort needed to calculate all eigenstates. If adding a multiple of $2\pi/a$ the wave will repeat itself, so k-values separated with $2\pi/a$ will give the same physical result. Hence, the solutions for all wave vectors can be found within the so called "Brillouin zone" $-\pi/a < k_x < \pi/a$ by adding a lattice vector.

Considering wave propagation in a mixed dielectric material consisting of isotropic, transparent materials ($\varepsilon(r)$ is real and positive), the displacement field, D($\mathbf{r}$,t) can be related to the electric field as $D(\mathbf{r}) = \varepsilon_0\varepsilon_\mathbf{r}E(\mathbf{r})$. Because the magnetic permeability is close to unity for most dielectric materials, the magnetic induction field, B($\mathbf{r}$) can be related to to the magnetic field via $B(\mathbf{r}) = \mu_0 H(\mathbf{r})$.

In these relations ε_0 and μ_0 are the vacuum dielectric constant and permeability respectively. Under these conditions, assuming there are no free charges or electric currents, Maxwell's equations can be represented in the following form [53, 52]:

$$\nabla \cdot \mathbf{H}(\mathbf{r},t) = 0, \tag{2.3}$$

$$\nabla \cdot \varepsilon(\mathbf{r})\mathbf{E}(\mathbf{r},t) = 0, \tag{2.4}$$

$$\nabla \times \mathbf{E}(\mathbf{r},t) = -\mu_0 \frac{\partial}{\partial t}\mathbf{H}(\mathbf{r},t), \tag{2.5}$$

$$\nabla \times \mathbf{H}(\mathbf{r},t) = \varepsilon_0 \varepsilon(\mathbf{r}) \frac{\partial}{\partial t}\mathbf{E}(\mathbf{r},t). \tag{2.6}$$

Maxwell's equations are linear, so the space and time dependence of the fields can be separated by expressing them as harmonic modes: $E(\mathbf{r},t) = E(\mathbf{r})e^{-i\omega t}, H(\mathbf{r},t) = H(\mathbf{r})e^{-i\omega t}$. The two equations Eq. 2.5 and Eq. 2.6 can be combined to eliminate $\mathbf{E}(\mathbf{r})$. Also, the speed of light in vacuum, c, can be expressed in terms of ε_0 and μ_0 according to $c = 1/\sqrt{\varepsilon_0\mu_0}$. This results in the "master equation" [52]:

$$\nabla \times (\frac{1}{\varepsilon(\mathbf{r})}\nabla \times \mathbf{H}(\mathbf{r})) = (\frac{\omega}{c})^2 \mathbf{H}(\mathbf{r}). \tag{2.7}$$

The solution to this problem will provide the eigenfrequencies $\omega(k)$. The operator in Eq. 2.7 is Hermitian, while the corresponding equation for the E-field is not. An Hermitian operator is desired because its eigenvalues are real numbers and the eigenvectors of two different eigenvalues are orthogonal. Once the solutions for H(r) are obtained, E(r) can be derived from Eq. 2.6: [52]

$$\mathbf{E}(\mathbf{r}) = -\frac{ic}{\omega\varepsilon(\mathbf{r})}\nabla \times \mathbf{H}(\mathbf{r}). \tag{2.8}$$

A freely available software package, MPB was used to solve the eigenvalue problem in Eq. 2.7 [54].

2.1.1 Linear Defect Waveguides

The dielectric structure is built by defining a unitcell, which is repeated using the periodic boundary conditions in MPB. The unitcell is the smallest part in the crystal, and in a defect-free membrane PhC it consists of a slab of dielectric material with a single

hole (cylinder of air). When introducing defects into the crystal lattice, such as a row of missing holes, the unitcell needs to be made larger. Lets introduce a coordinate system for the PhC structure, and place x along the waveguide, y vertically out from the waveguide in plane with the crystal, and z normal to the crystal. The unitcell we used for a PhC waveguide simulations consist of 7 rows of holes on each side of the waveguide (y-direction) and 2 lattice constants high in the z-direction. All devices in this work consist of a $340nm$ InGaAsP slab ($n = 3.45$), surrounded by air and with air-holes arranged in a triangular lattice. Figure 2.1 (left) shows a dispersion diagram plotted versus the wave vector component k along the waveguide, in the first Brillouin zone $k = (0, \pi/a)$. The figure displays the polarization parallel to the 2D plane (TE polarization). All structural parameters scale with the lattice constant because Maxwell's equations are scale invariant. Hence, also the frequency is normalized $\omega_{norm} = a/\lambda$. This means that from the dispersion diagram one can select a desired center transmission wavelength of the guided mode, and obtain the structural dimensions of the crystal. This requires that the thickness of the membrane can be adjusted freely too. In practice, membrane thickness as defined in the epitaxial growth of the wafer. It is chosen to be $340nm$ thick for all samples in this work. So one dispersion diagram for each lattice constant needs to be derived. The parameters of the crystal in Figure 2.1 (left) are: hole radius $r = 0.27a$, membrane thickness $h = 0.85a$, leading to a lattice constant $a = 400nm$.

Light is confined in plane with the membrane by the PhC effect and vertically by index guiding. The light-line indicates the border between vertically confined light by TIR and out of plane radiation modes (the grey shaded area in Figure 2.1. Light coupled to modes above the light-line will suffer large intrinsic loss. In the band diagram two regions with a continuum of modes can be seen, at low and high frequencies respectively. The electric field of these modes are not confined in the waveguide, but extend out in the membrane. Low frequency modes have most of their energy located in the high index regions of the crystal. High frequency modes on the other hand, have a larger fraction of their energy in the low index material. Hence, the two regions are called index and air band respectively. The fact that the energy field distributions

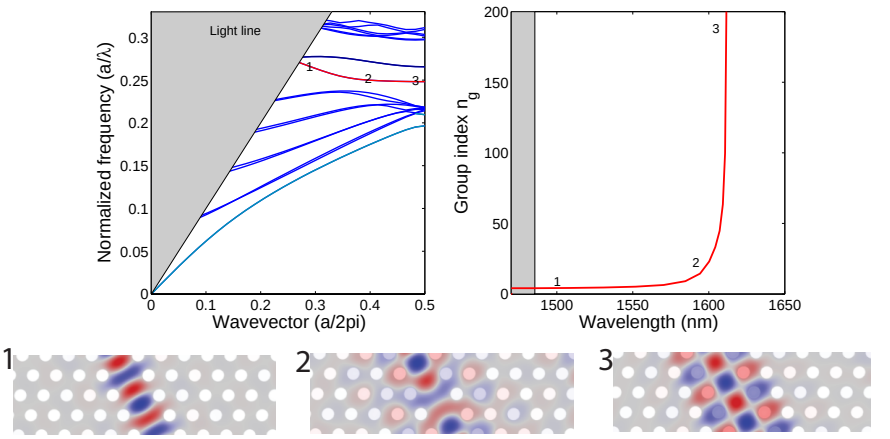

Figure 2.1: Left: a dispersion diagram for a membrane waveguide with refractive index 3.45 surrounded. The defect waveguide (one row of missing holes) introduces guided modes in the bandgap of the PhC. The red curve represents the fundamental, even mode. And the dark blue curve represents the odd mode. Right: The group index of the fundamental mode. Lower: H_z field distributions for the fundamental mode at the three marked frequencies.

depend on the mode frequency explains why a gap arises. If it was not for the linear defect waveguide in this example, there would be no modes in the gap region between the index and the air band. However, the waveguide has a series of guided modes within the gap (red, darkblue), and also below the index band (light blue). The modes below the index band are purely index guided, due to the high index of the waveguide compared to the lower average index in the PhC cladding and in the surrounding air. There are also two guided modes inside the gap. The fundamental mode is the one with lowest frequency, marked in red. We focus on the fundamental mode, because owing to its even field distribution this is the one which is most easily excited by an incoming plane wave. The second mode (marked in dark blue) has an odd spatial distribution of the field in the waveguide. This does not only cause coupling loss, but also leads to poor light matter interaction.

Figure 2.1 (lower) shows the fundamental mode's electric field distributions at the k-points indicated in the dispersion diagram. The field distribution for wave vectors approaching the edge of the Brillouin zone show two additional nodes in the y-direction, compared

with the distributions for wave vectors close to the light line. The drastic changes in the field distribution along the same mode is explained by an anti-crossing phenomena caused by the band gap [52], this have been observed in reference [29]. Two bands which are expected to intersect, instead couple to one another. An anti-crossing occurs, leading to the formation of an hybrid mode which resembles an index-guided mode for $0.28 < k < 0.35$ and band gap guided for $0.35 < k < 0.5$. Looking at fundamental mode (red) in Figure 2.1 it is clear that the band flattens out close to the Brillouin edge. Because the group velocity is described by the derivative of the dispersion $v_g = \delta\omega/\delta k$, it is clear that it approaches $v_g = 0ms^{-1}$ at the band edge. In Figure 2.1 (right) the group index ($n_g = c/v_g$) of the fundamental mode is plotted. Using the lattice constant ($a = 400nm$) the normalized frequency is converted to wavelength. Experimentally, the highest group index measured in a PhC waveguide to date is 300 [31]. Slow light is very sensitive to disorders, because of its wide field distribution [55, 56]. Scattering loss is believed to be the main limiting factor for slow light [57]. Despite the high resolution process technologies employed to realize theses structures, a fabricated device will always exhibit a certain degree of side-wall roughness and disorder [58]. The nature of the slow down can be understood by light being backscattered at each unitcell of the photonic crystal. As illustrated in Figure 2.2 light, qualitatively, moves forward four steps and back three steps, resulting in a net slow forward propagation [25]. Because slow modes experience almost as much backward as forward propagation there is a fine balance between the two which can easily be disrupted by scattering caused by process-disorder. This effect is strong when the propagating wavelength is in resonance with the structure. By careful design a broader range of wavelengths can be slowed down, and not only highly dispersive light at the band edge of the PhC mode.

In Figure 2.3 shows how the wavelength of the fundamental mode bandedge (at k=a/π) shifts as different design parameters change. Except for the parameter under investigation in each plot the remaining parameters are: radius $r = 0.25a$, thickness $t = 340nm$, lattice constant $a = 400nm$ and relative permittivity $\varepsilon = 11.2$. The lattice constant and the hole diameter are freely variable pa-

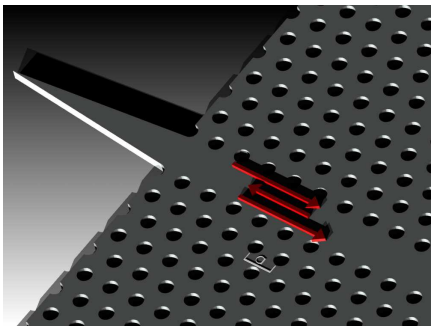

Figure 2.2: Illustration of the forward and backscattering which a slow light mode experiences. The lattice constant, a, is marked in the figure.

rameters, and can be varied to achieve a systematic shift in the band-edge spectrally, and thereby the slow light region of the PhC waveguide. Also the membrane thickness has a pronounced affect on the band edge wavelength. It is therefore important to have a reproducible process, where the same membrane thickness is achieved in every run. If the band edge is at too long wavelength, the membrane could be systematically thinned down in order to tune the wavelength. However, it requires a reproducible method and one issue is that also the hole radius will increase when etching the membrane. The fourth parameter which is varied is the relative permittivity of the material. Including more active material into the membrane, such as 10 QWs, will increase the relative permittivity, and thereby shift the band edge to longer wavelength. External sources such as an energetic optical pump focused onto the sample, can also cause a change in refractive index, and thereby shift the band edge wavelength.

A final note on PhC design is on the TM polarization (perpendicular to the 2D plane). Imperfection, roughness, or non-vertical holes can result in some depolarization of light. Light is not only scattered, but can also be coupled into other waveguide modes such as the TE odd or TM modes [59, 60]. Complete bandgap crystals have been investigated [61] and experimentally demonstrated [62] using triangular holes which might limit other design possibilities. Figure 2.4 (left) shows the dispersion diagram for the TM polarization (grey) and the fundamental TE mode (red). The TM polarization exhibit a small gap (named TM minigap in figure), about 5 nm

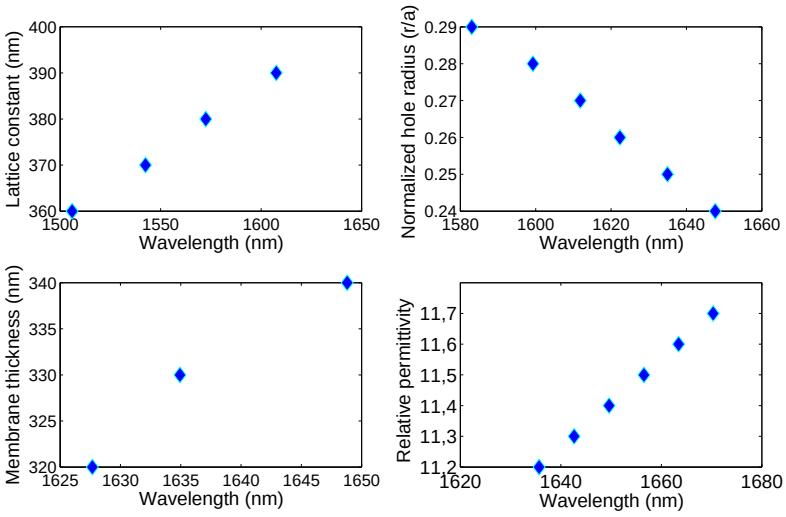

Figure 2.3: The spectral position of the fundamental guided band edge for different design parameters. Except for the variable under investigation in each plot, the other design parameters are kept constant. Lattice constant a = 400nm, radius r=0.25a=100nm, membrane thickness t=340nm and relative permittivity ε=11.2. Using these parameters the wavelength region is not centred around 1550nm in each plot, but provides an idea about the wavelength shift associated with a change in each design parameter. Left top: Lattice constant. Right top: radius. Left bottom: membrane thickness. Right bottom: relative permittivity.

wide. The slow light modes at the edges of the minigap, as well as the sharp drop in intensity at the gap wavelength for TM transmission, are observed in Section 4.4.1. However, it does not interfere with the TE performance because the TM minigap is well separated from the TE band edge. The TM dispersion is more affected by changes in membrane thickness than TE, as shown in Figure 2.4 (right). Thus, the TM dispersion could play a role in choosing the membrane thickness.

2.2 Photonic Crystal Amplifiers

The energy band diagram for the 340nm thick membrane including 6nm thick 1% compressively strained QWs is presented in Figure 2.5 (left). In the following calculations, 4 QWs are used, and no

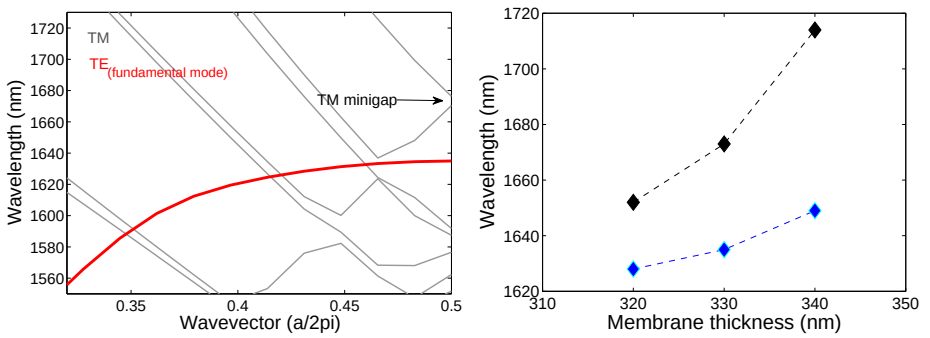

Figure 2.4: Left: dispersion diagram for TM polarization (gray) and the TE fundamental mode (red) (a=400 nm, t=330 nm, r=100 nm). The TM minigap is indicated in the figure. Right: Spectral position of the TE bandedge (blue) and TM minigap (black).

coupling between the wells are included.

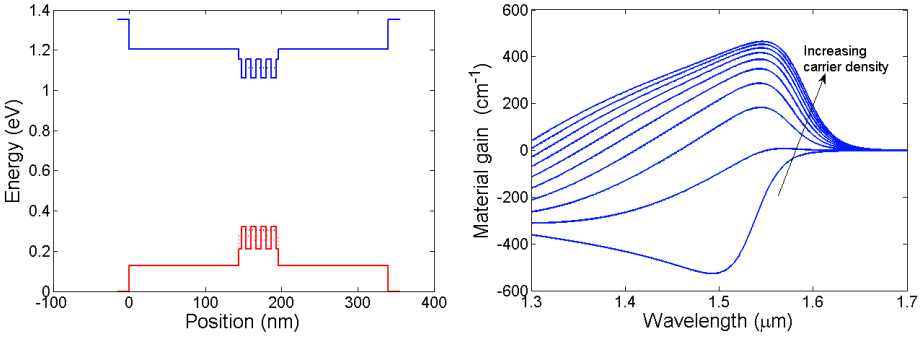

Figure 2.5: Left: Band diagram of the membrane with 4 QWs of $6nm$ thickness. The dashed lines in the QW region indicates the lowest quantum confined state (calculated for a single well). The depth of the wells are noted in the legend. Right: Calculated gain curves for carrier densities ranging from $1 \cdot 10^8 - -30 \cdot 10^{12}$.

For gain calculations of the active material used in the PhC amplifiers only the transition between the conduction band and the heavy hole band are considered. The membrane material is $In_{0.77}GaAs_{0.503}P$, lattice matched to InP. The gap energy is $E_g = 1.078eV$ or expressed in wavelength; $\lambda = 1.15\mu m$, and the band edge c-hh transition is at $\lambda = 1538nm$ for the $6nm$ thick QWs considered. Once the individual electron and hole energies are obtained, the Fermi occupation probability can be derived for both

the electrons (f_e) and holes (f_h) at the band edge. Material parameters are taken from [63]. The following relation between the modal TE gain (g) and the inversion of the material ($f_e + f_h - 1$) can be used [37]:

$$g = \Gamma g_{max} \cdot (f_e + f_h - 1) \tag{2.9}$$

where Γ is the confinement factor, proportional to the number of wells. The material gain from one well, g_{max}, takes density of states, wave function overlap (only allowed transitions) and matrix elements (polarization dependence) into account[1].

A crude prediction of how a PhC can change the transmission and ASE spectra is derived by including a slow down factor $S(\omega)$:

$$S(\omega) = \frac{n_{PhC}^{g}}{n_{g}^{back}} \tag{2.10}$$

It has been suggested by others that in the linear regime, the enhanced interaction with slowly propagating light is proportional to $S(\omega)$ [64, 65]. Both the gain and the loss is expected to scale with the S-factor. The transmission $T(\omega)$ then becomes:

$$T(\omega) = \frac{P_{out}(\omega)}{P_{in}(\omega)} = exp[S(\omega)(\Gamma(\omega)g(\omega) - \alpha_{int})L] \tag{2.11}$$

where L is the length of the device ($1mm$) and α_{int} are the internal losses which is the sum of disorder induced losses and free carrier absorption, the latter scale with the carrier density. The band edge of the PhC guided mode is at $\lambda = 1.57\mu m$ and group index is limited to reach a value of $n_g^{PhC} = 150$, because that is credible to achieve experimentally. The transmission spectra at three different carrier densities are shown in Figure 2.6. When slightly higher gain (the corresponding gain curves are curve 3, 4, and 5 in Figure 2.5 (right)), the transmission increases rapidly owing to the exponential dependence of the enhancement.

The ASE has been suggested to be doubly enhanced by the slow down factor [66]. The two key factors responsible for the enhancement are firstly that the slow light propagates an effectively longer

[1] Private communication with Kresten Yvind, DTU Fotonik.

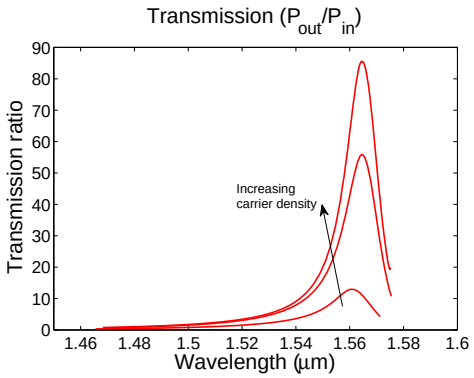

Figure 2.6: Transmission spectra for a PhC amplifier at three different current densities.

path length through the active material, the second factor is that the optical density of states is enhanced. ASE is stimulated emission due to vacuum modes, also the vacuum modes depend on the density of states, so the optical transition is accelerated. The expression for the ASE (power spectral density) becomes:

$$\mid E(\omega) \mid^2 = 2\pi\hbar S(\omega) n_{sp}(\omega) \frac{1}{1 - \alpha_{int}/(\Gamma(\omega)g(\omega))} (T(\omega) - 1) \quad (2.12)$$

where n_{sp} is the population inversion factor, defined as [34]:

$$n_{sp}(\omega) = \frac{f_c(E_c) f_v(E_v)}{f_c(E_c) + f_v(E_v) - 1} \quad (2.13)$$

where E_c and E_v denote the electron energy in the conduction and the valence band respectively. Figure 2.7 shows transmission and ASE for a PhC waveguide (red) and as a reference for a ridge waveguide (black) where gain is not enhanced due to light slow down. op

These calculations are based on simple gain calculations and assumptions. To our knowledge, no rigorous theoretical descriptions of PhC amplifiers can be found in the literature. The presented calculations gives an indication about the pronounced enhancement effect the slow down factor has on both the amplification of transmitted light and on the ASE. PhCs can be simulated using FDTD techniques, see e.g. [51]. But a description of PhC amplifiers require FDTD simulations including gain material. FDTD simulations are time consuming and difficult to scale up to actual device sizes. In

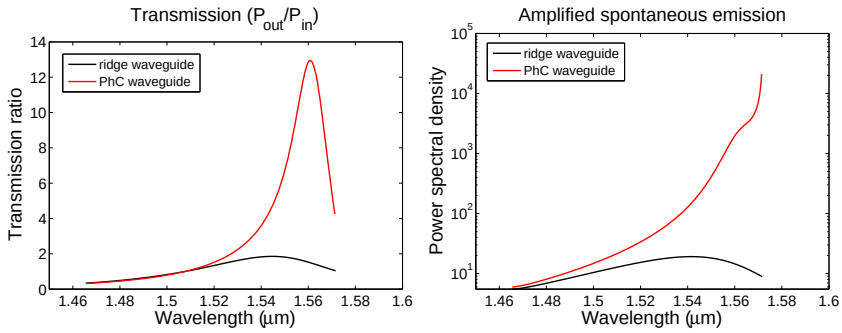

Figure 2.7: Transmission (left) and ASE (right) with and without slow down factor.

order to get an insight into the physics of the devices, and assist device design, coupled wave based simulations can be an used [67, 68]. The computation of Bloch modes are done separately which reduces computational cost, and makes the model compatible with dispersion engineering methods such as topology optimization.

2.3 Population Inversion by Optically Pumping

All the devices in this work are optically pumped. Light is focused onto the sample from the top, because a short wavelength is used ($800nm$ or $980nm$), carriers are excited into the barriers. Therefore, the full thickness of the membrane is absorbing the incoming photons.

The optical power required to pump a single QW in a 340 nm membrane slab is estimated through the rate equation. The change in carriers, N, is;

$$\frac{dN}{dt} = G_{gen} - R_{rec} \tag{2.14}$$

$$\frac{dN}{dt} = \frac{\Delta P}{\hbar \omega A_{wg}} - \frac{N}{\tau} = 0 \tag{2.15}$$

where G_{gen} is the rate of injected electrons (absorbed photons) into the active region. The absorbed power, $\Delta P = \alpha t P_{in}$, depends on

the absorption in the waveguide region $\alpha = \alpha_{mat} \times A_{wg}/A_{spot}$ and the membrane thickness, t. R_{rec} is the rate of spontaneous, non-radiative and leakage recombination of electrons per unit volume which is described by a carrier lifetime, τ, as N/τ [34]. From Eq. 2.15 the required input power, P_{in} to achieve population inversion becomes:

$$P_{in} = \frac{N\hbar\omega A_{spot}}{\tau\alpha_{mat}t} \tag{2.16}$$

Using material constants from reference [34] , a membrane thickness of $t = 340nm$ and a pump spot of $A_{spot} = 2\mu m \times 1mm$, the estimated input power is $P_{in} = 240mW$. The required power level is high, and it is clear that a tight focus, or a shorter waveguide than $1mm$, is called for. The Gaussian beam profile affects the spatial distribution of the population inversion along the waveguide. Hence, even higher powers might be required to reach a total inversion and avoid ending up with a section of gain in the center part of the waveguide, surrounded by absorbing regions, see Figure 2.8. The figure illustrates the smooth transition from pumped to unpumped regions of the device. Systematic measurements at different pump lengths requires a more well defined profile by cutting the beam in an imaging plane or just in front of the device.

2.3.1 Thermal Resistance

To obtain the best possible optical confinement in the InGaAsP membrane, it is surrounded by air. The large index contrast between the membrane and the surroundings allows light with a large range of wavevectors to propagate with limited out of plane losses. It offers a large degree of freedom when designing the PhC. Unfortunately it comes with a huge disadvantage; extremely poor heat conduction. Additional to the unfavourable geometrical configuration, quartenary material such as InGaAsP exhibit much lower thermal conductivity (5.93 W/mK) than its binary counterpart InP (68 W/mK) [69]. Not only amplifiers but also PhC laser structures suffer from heating, which might prevent CW lasing operation. Also when CW operation is achieved [70, 71], heating limits the output power. Electrically pumped structures, e.g.lasers in [72], are less

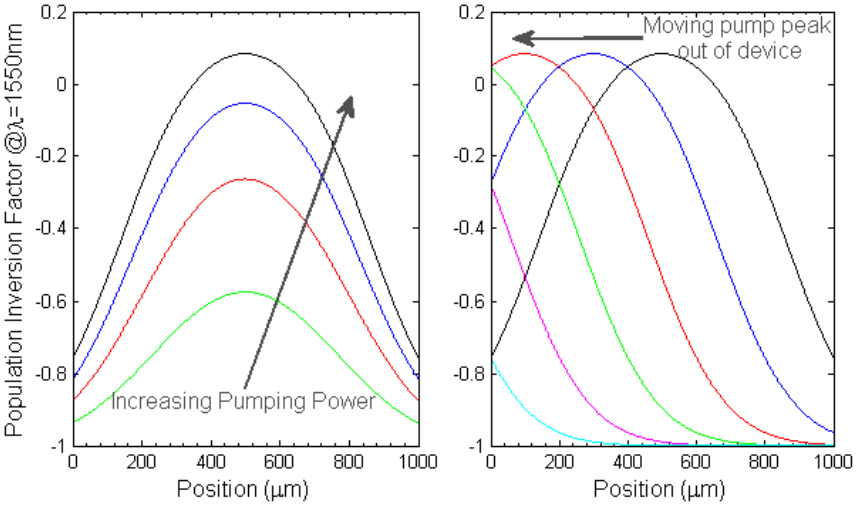

Figure 2.8: Left: Spatial population distribution along a 1 QW waveguide when using an optical pump with a Gaussian beam profile. Right: Illustrating the scenario when the pump is moved along the waveguide to excite different lengths of the device. *Figure by courtesy of Yaohui Chen, DTU Fotonik.*

heated than optically pumped structures, because the carriers do not have as much excess energy. Also heat-conductive claddings [73] have proven to improve the thermal properties. In reference [73] heat dissipation is improved by bonding the PhC membrane to sapphire. It results in more loss due to the higher index of sapphire and the non-symmetric device design hampers dispersion engineering. In general, it is difficult to introduce electrical contacts or interactive heat spreaders [74] without also causing more loss in the system. This trade-off needs to be balanced to reach optimal performance, but it is desirable to end up with a symmetric design. An important development is the demonstration of buried heterostructure PhCs by Matsuo et al. [75]. It is challenging to transfer the well known buried heterostructure to the PhC platform, due to the high demands on precision and sub-micrometer feature sizes. However, such device structure can strongly improve thermal relaxation and efficiency. By limiting the active region to the waveguide re-

gion only, a higher confinement of carriers will result in reaching a complete population inversion at lower pump powers. Burying the active InGaAsP region in a InP membrane, will limit the heating to the active region only, and from there it is efficiently conducted out into the surrounding InP.

The thermal resistance was calculated[2]for our device design using a two dimensional finite element method. The differential equation describing the heat flow in the material is:

$$\nabla \cdot (-k\nabla T) = \rho_s - \rho C \mathbf{u} \cdot \nabla T \tag{2.17}$$

where the heat source density ρ_s is defined as the thermal power (assumed to be 10% of the absorbed power, energy released due to electron relaxation from excited states to QW states) divided by the volume of material, T is the temerature in Kelvin, and $\mathbf{u}$ is a velocity vector. Thermal conductivity, $k = 5.93W/(m \cdot K)$, density, $\rho = 5120kg/m^3$, and specific heat, $C = 304J/(kg \cdot K)$, are all material parameters [69]. The numerical simulation of the surface temperature in our $340nm$ thick $In_{0.77}GaAs_{0.5}P$ membrane is shown in Figure 2.9. If a pump power of $200mW$ is absorbed in the material, the estimated thermal power is $20mW$. From the simulations a thermal resistance ($R = \Delta T/P_{thermal}$ of the structure was found to be 4.57 K/mW. A 7-fold improvement of the thermal resistance is expected for an InP membrane.

2.3.2 Pulsed Pumping

The performance of an active PhC membrane waveguide is severely deteriorated if the material is heated. Allowing time for thermal relaxation in between each pumping event will prevent a high temperature to build up in the material. Therefore, a pulsed excitation where each pulse is powerful enough to bring the material into the gain regime, while ensuring a low overall energy due to a low repetition rate is preferable. It is necessary to reduce the material heating as much as possible to achieve best device performance. A heated lattice will spread the carriers in energy and make the carriers more mobile, and more likely to leak out of the QW/QD

[2]The thermal simulations were done by Luca Carletti, DTU Fotonik.

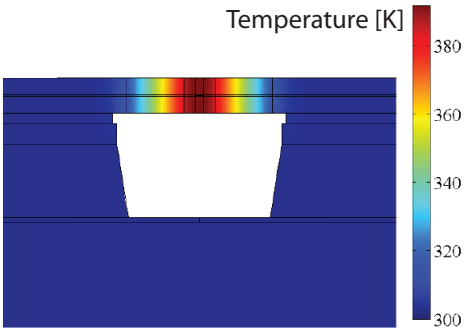

Figure 2.9: Numerical simulation results for a vertical cross section of the InGaAsP membrane structure. *Figure by courtesy of Luca Carletti, DTU Fotonik.*

region and hence not contributing to the optical gain. Another important issue is the physical damage itself. If the temperature is raised above the temperature for thermal damage the sample will literally burn, see SEM images in Section 4.2.1.

With a pulsed pump net gain can be achieved during the short time window when the pulse is present. If the duty cycle is 1% or less, it means that the material is absorbing most of the time. This calls for sensitive detection schemes and a synchronization between pump and signal. If ultrashort pulses are used, in this work a pulse duration of 1 ps was used in part of the measurements, the time window where there is a significant carrier excitation is proportional to the carrier lifetime. The population inversion[3]induced by a single pump pulse is shown in Figure 2.10.

As long as the pulses are significantly shorter than the carrier lifetime (which is about 500 ps), the actual pulse duration does not influence the population inversion and switch-on time window much. However, the period between each excitation event is important.

[3]Modelling of active PhC waveguides by Yaohui Chen, DTU Fotonik.

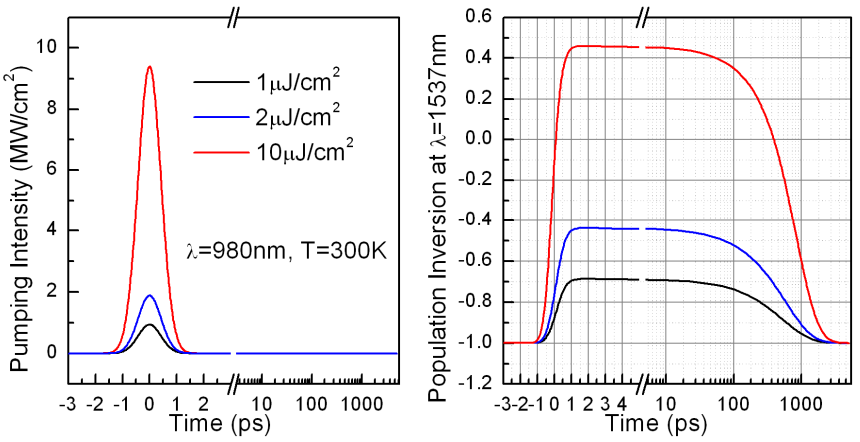

Figure 2.10: Left: An example of short pulse excitation at different energies. Right: the corresponding population inversion at each pump power as a function of time. The time-window for gain is proportional to the carrier lifetime (set to be 500 ps in the calculations). *Figure by courtesy of Yaohui Chen, DTU Fotonik.*

Chapter 3

Fabrication

The fabrication process developed within this project to achieve active photonic crystal waveguides is described in this chapter. All processing is done at DANCHIP cleanroom facility and the process is developed for the equipment available during the time of this work. First, an overview of the process is given, followed by more detailed descriptions.

3.1 Process Overview

The fabricated devices are based on the InP-material system, which is commonly used for communication applications operating in the $1.31/1.55\mu m$ regime. The top cladding of the wafer consists of quaternary $In_{1-x}Ga_xAs_yP_{1-y}$ ($\lambda_g = 1150nm$) material in which active layers of quantum dots or quantum wells are incorporated. Together these layers form a $340nm$ thick active slab in which the PhC pattern is created. Beneath the active slab there are 1 μm of sacrificial layers, to be etched away in order to obtain an air membrane structure. A more detailed description of the epistructure is presented in Section 3.2.1.

A schematic overview of the process is illustrated in Figure 3.1. Each step as shown in the figure is described briefly below.

Mask deposition A 200 nm layer of Si_3N_4 was deposited uni-

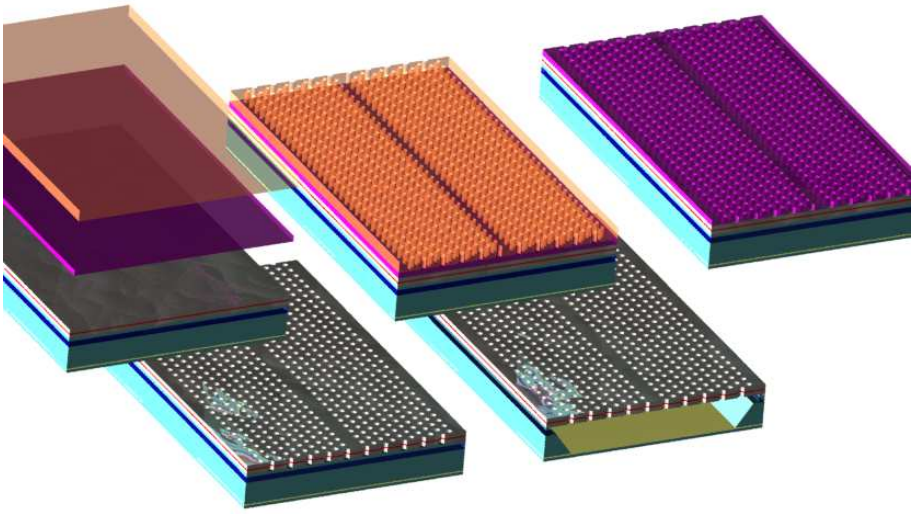

Figure 3.1: An illustration of the processing steps involved to achieve a free-standing membrane PhC.

formly on the wafer using a plasma enhanced vapor deposition (PECVD). This serves as a hard mask which shield everything but the features to be etched into the quaternary material. A positive e-beam resist (zep520A) is spin-coated onto the hard mask. The resist viscosity and spin settings were chosen to obtain a $500nm$ thick film.

E-beam lithography Patterning is done using a 100kV e-beam writer JEOL-JBX9300FS. After the exposure the wafer is developed in ZED N50 for 2 minutes, while constantly swirling the developer over the wafer to fully develop all features.

Pattern transfer The pattern is transferred onto the hard mask by CHF_3/O_2 reactive ion etching (RIE), more details in Section 3.4.1.

Semiconductor etch A cyclic CH_4/H_2-O_2 RIE was used, which is highly anisotropic and selective, see section 3.4.1.

Wet etch The final steps of the processing was completed using wet etch. A 2 minute hydrofluoric acid etch to remove the Si_3N_4 was followed by a cyclic $1HCl : 1H_2O$ - HF etch to remove the sacrificial layers and obtain a free standing air membrane.

3.2 Sample Layout

Scattering is an important loss mechanism and is reduced by improving the surface roughness, verticality of the holes, and uniformity; means to reduce these fabrication imperfections are discussed in this chapter. Any device will suffer from fabrication disorders, and the most efficient way to further reduce the scattering loss is to limit the device length. Arbitrary short PhC waveguides can be fabricated if access waveguides made for on chip guiding from the chip edge to the crystal are used [31]. Such access waveguides should preferably be passive, to avoid the need to pump them and to let the PhC waveguide alone be responsible for the amplification. To achieve that a buried heterostructure [75], with active material in selected region of the membrane only, is desired. Another solution would be to selectively etch away the active layers on the access waveguides only. The active layers would then need to be placed close to the top surface of the membrane, corresponding to the edge of the propagating optical field envelope, resulting in reduced light-matter interaction. Despite of that disadvantage the layout would still be interesting. In order to realize it, the membrane needs to rest on a low index material, which also can support the access waveguides. This approach, having a low index insulator under the devices, have proven useful in silicon photonics, as most silicon devices are on the silicon on insulator platform. A non-symmetric environment around the PhC, with a higher index material below the slab than above, is undesired because it complicates the designs and reduces the bandwidth of the PhC guided mode. On the other hand there could be a lot to gain in being able to reduce the device size, and through that reduce loss and allow for more tightly focused optical pump spots. A promising candidate for such a low index insulator material is oxidized InAlAs [76, 77], which was investi-

gated in this work. The waveguide layers can be epitaxially grown on top of the InAlAs because both are lattice matched to InP. A wafer with a $1\mu m$ thick layer of InAlAs underneath a $340nm$ thick InGaAsP waveguide layer was used. Ridge waveguides, defined in the waveguide layer using photo lithography are used in order to expose the InAlAs layer to the environment in certain areas, while being able to see the quality of the oxide undercut. Nitrogen is bubbled through water, heated to a stable temperature of 95 degrees. The stream (flow=990 sccm) of gas then enters the furnace set at 550 degrees, where the sample is oxidized for 30 minutes. These were found to be the best conditions for the present wafer and the result is shown in Figure 3.2. The SEM image shows a side-view of a cleaved facet. The surface roughness at the bottom of the waveguide layer is considered to be too severe for PhC applications. Alternatively, access waveguides of a different material can be used, for example BCB. It can be achieved by bonding the III-V top layer to BCB, recently achieved at DANCHIP with good yield [78].

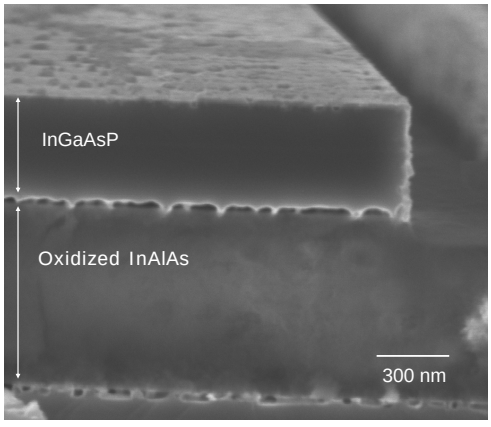

Figure 3.2: Oxidation test of a InAlAs below InGaAsP. Oxidized for 30 minutes at 550 degrees with 95° bubbler.

Due to the unsatisfactory result of the oxidization and in absence of other methods at the time, all the devices used in this project are without access waveguides. The device length was therefore limited by how small chips InP can be cleaved into. A cleaving accuracy of $\pm 5\mu$m is required, and that can be achieved for a chip sizes of about $1mm$. In order to obtain shorter PhC amplifiers,

the PhC waveguide is interrupted by a PhC mirror so that only one accurate cleave is required and the device length is defined by the mirror location. Figure 3.3 illustrates the two PhC amplifier designs.

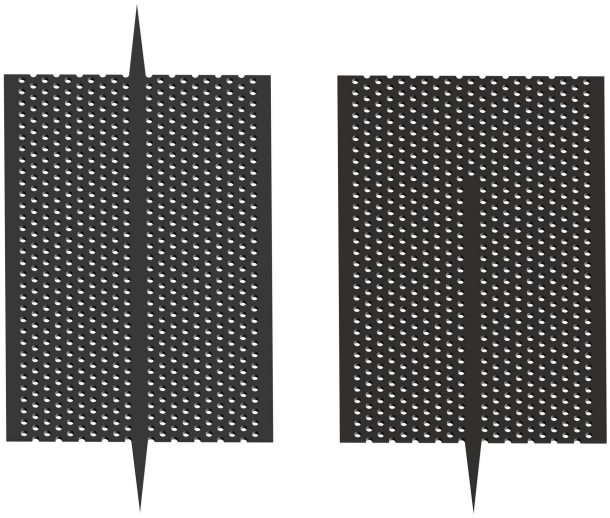

Figure 3.3: An illustration of the two amplifier designs equipped with tapers. Left: an amplifier with input and output tapers. This design can be made down to $900\mu m$ long, limited by cleaving capability. Right: an amplifier with one single taper. This design can be made as short as desired.

In- and out coupling losses due to mismatch of mode profiles inside and outside the PhC waveguide are important loss mechanisms. The coupling efficiency into the slab PhC waveguide can be improved using an inverted taper, as demonstrated for a passive device by Tran et al. [79]. The tapers are 6 lattice constants long and are shown in Figure 3.3, they are added to the device without an extra processing step. By using tapers the Fabry-Pérot oscillations which are caused by reflection at the end facets are suppressed, and lasing action in the amplifiers is avoided. Coupling to slow modes could be improved further by using a slow light coupler. The abrupt difference in the spatial distribution if an incoming gaussian mode and the slow light mode causes a coupling loss greater than that for fast light. A PhC design which allows for efficient coupling between the incoming fast light and the slow light could improve the perfor-

mance of slow light devices, examples of such couplers are found in references [80, 81].

3.2.1 Epitaxial layout

All wafers used in the processing were grown epitaxially[1]. The structure for the wafer with one QW is outlined in Table 3.1. The top capping layer is there to protect the wafer from dirt trough the processing and is removed during the final wet etch, along with etching the sacrificial layers. The InGaAsP (Q1.15) layers with the incorporated active quantum well in the center makes up the membrane. Underneath the 340 nm thick membrane there are layers of InP and InAlAs, which together add up to $1\mu m$ of sacrificial material. The choice of sacrificial layers is discussed in Section 3.4.2.

Table 3.1: Epitaxial structure of the wafer with a single quantum well

Composition	x	y	Thickness (nm)	comment
InP			20	capping layer
In_xGaAs_yP	0.77	0.503	163.4	membrane
In_xGaAs_yP	0.49	0.86	3.6	barrier
In_xGaAs_yP	0.75	0.86	6	well
In_xGaAs_yP	0.49	0.86	3.6	barrier
In_xGaAs_yP	0.77	0.503	163.4	membrane
InP			100	sacrificial layer
In_xAlAs	0.52		200	sacrificial layer
InP			700	sacrificial layer
$GaIn_xAs$	0.53		200	etch stop
InP			50	buffer
$InPwafer$				

[1]All wafer growth is done by Elizaveta Semenova and Kresten Yvind, DTU Fotonik.

Samples processed on 10QW and 3QD wafers are also presented in this work. They have similar epitaxial structures but with more layers of active material in the membrane and with a slightly thinner layer of InAlAs (100nm) in the sacrificial stack. The 10 QWs are located in the center of the membrane with a 8.6 nm barrier in between each well. Figure 3.4 shows the band diagram of the 10QW wafer (top) and SEM images of 3QD, 1QW and 10QW devices respectively.

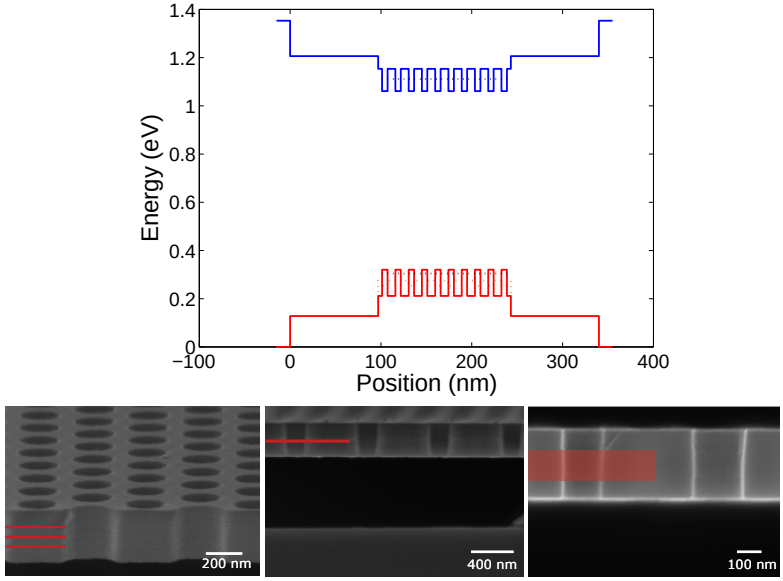

Figure 3.4: Top: band diagram of a 10 QW membrane. Bottom: SEM images of processed samples showing the active material incorporated in the membrane; 3QD, 1QW and 10QW from left to right.

Only a few groups have been able to achieve InAs QDs on (001) InP wafer with an emission wavelength at 1.55 μm [82, 83, 84, 85]. The main challenge compared to InAs dots on GaAs is that the lattice mismatch is lower which leads to larger dots, emitting at wavelengths beyond 1.65 μm. It has been shown that a thin underlayer of GaAs [83], or a double capping technique [85] can be used to control the emission wavelength of the dots. This was successful in our group using a 1.6 monolayer GaAs capping on top of the InAs QDs [38].

3.3 Patterning

3.3.1 Masking materials

Two masks are used; ZEP 520A which is a high resolution e-beam resist, and Si_3N_4 which can withstand the semiconductor RIE etch. The Si_3N_4 is deposited using PECVD and the film thickness is measured with an ellipsometer. The desired film thickness is 200 nm, which is a trade off between it being thick enough to remain during the entire RIE etch, while being as thin as possible to avoid shadowing effects, see Section 3.4.1.

The resist is spin-coated onto the Si_3N_4. It may be diluted with anisol (methoxybenzene) to desired viscosity. With 11% ZEP spin-coated for $60s$ at $2000rpm$ a thickness of $500nm$ was obtained. After the RIE hard mask etch the resist is removed in a heated ($60°C$) microdeposit Remover 1165 at a low ultrasonic agitation. The sample is placed with the pattern facing down in order to prevent the resist from reattaching onto the surface, and it is left in the remover for two hours. Any resist residuals left on the surface are removed by plasma ashing. In the hard mask etch (in CHF_3/O_2 plasma) the morphology of the resist surface changes, or becomes damaged. It was found that if the resist is not sufficiently thick, damaged resist will attach to the Si_3N_4 surface from where it is very difficult to remove, and will therefore cause pattern deformation. Figure 3.5 shows a bad example of the rough edges around each hole as a result of damaged resist attached to the hard mask.

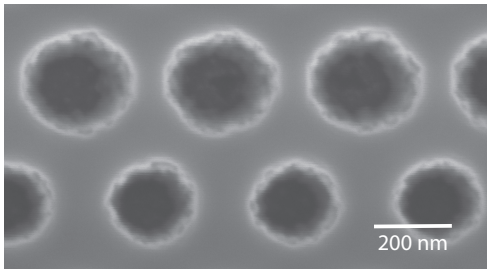

Figure 3.5: SEM image of a bad example of etched holes with very rough edges. The roughness is a result a damaged resist, causing non-perfect holes in the hard mask.

3.3.2 Electron Beam Lithography

The electron lithography system available at DANCHIP was used for the patterning in this work. It is an electron beam (e-beam) writer JEOL JBX-9300FS with an acceleration voltage of up to $100kV$. E-beam lithography is employed because of its nm-accuracy and ability to define sub-μm features. An continuous electron beam is focused using magnetic lenses onto the wafer. The pattern is written point by point and the writing field is $500\mu m \times 500\mu m$ with a stitching overlay of $30nm$ [86]. It is a well known phenomena that when exposing a dense pattern, such as a PhC, proximity effects can give rise to a non-uniform exposure [87]. Due to forward- and back-scattering of electrons from the resist and wafer, the exposed region becomes larger than the point of beam incidence. Features in the center of a dense pattern may end up larger than the features at the edges. This effect can be compensated for by using different exposure doses for different parts of the pattern [88].

The dose for all the samples in this work is $220\mu C$ per cm^2 and proximity correction is not used for any samples. However, this should be addressed for future devices, as proximity effects limit the processing accuracy of complicated designs with a dense pattern of features of different sizes.

3.4 Etching

3.4.1 Reactive Ion Etching

A highly anisotropic etch is desired to define holes with vertical sidewalls. Dry etching is therefore a good choice. Photonic crystal holes with impressive depth have been reported using Inductively Coupled Plasma (ICP) systems [89, 90]. In such a system a high density plasma is created by electromagnetic induction, while the ion acceleration towards the sample is controlled by parallel plate RF-power. The main advantage of this system compared to a RIE is that the concentration and ion energy can be controlled separately. During the time of this project there was no ICP in the

DANCHIP facilities so instead we used a RIE parallel plate system from PLASSYS. In that system the same RF power generates the plasma and provides the voltage drop towards the sample that determines the ion acceleration and bombardment energy. The ion concentration is mainly controlled by changing the gas flow and the pressure of the gases.

The two plates in the RIE chamber are the anode; where the gas-inlets are located, and the cathode, on which the sample is placed. The applied RF oscillating electromagnetic field creates a plasma by ionizing the gas molecules. Plasma is a complex mixture of ions, electrons and neutrals. The electrons have high mobility and respond to the RF potential, so in each cycle of the field they are accelerated in the chamber, eventually striking a chamber wall and are grounded. The ions on the other hand, are heavy and respond only to the time-averaged potential. Ions are accelerated in the RF field and strike the sample. Depending on the energy of the striking ions the etch may be dominantly physical (sputtering) or chemical [91].

Ion Assisted Chemical Etching

In the plasma free radicals, etchants, are created. These are neutral atoms or molecules with unpaired electrons. The etchants chemically etch the sample by reacting with the material, in order to form more stable products. If there were no crystallographic effects this would result in an isotropic etch; with an equal etch rate in all directions. It would resemble a wet etch of the material with poor pattern transfer due to a severe undercut of the masking material.

The chemical etching may be assisted by accelerated ions striking the surface to be etched. At the bombardment site the desorption of the etch-product is increased allowing access for more radicals. Ions are accelerated vertically in the chamber and are therefore only bombarding the sample surface which is not shielded by a mask. The etch rate on the bombarded surface is much higher than on the sidewalls, leading to anisotropic profiles [35]. The term "reactive ion etching" is slightly misleading; the chemical nature of the ion does not influence the yield much, it is the neutral which reacts with

the material and dominates the etch rate and selectivity [92]. If the energy of the bombarding ions is sufficiently high (about $400eV$ for argon ions), they may physically brake the bonds in the material to be etched (sputtering). The result will be a highly anisotropic etch, with severe damage on the etched surface and poor selectivity - requiring a mask which can withstand the sputtering. Ion assisted chemical etching show much faster etch rates than sputtering and with good anisotropy. Together with other advantages such as less damage and better selectivity makes it the preferable etching technique.

The RIE Chamber

The PLASSYS system used in this project is a parallel plate system with an RF frequency of 13.56 MHz. The cathode is located in the bottom of the chamber, covered by a quartz plate on which the sample is placed. The quartz plate is cooled to 20 degrees Celsius. The anode is centred at the top of the chamber, and that is also where the gas inlets are located. The pressure in the chamber is maintained with a turbo pump and controlled via a throttle valve. Because there is no load lock on the chamber in DANCHIP, chloride based etches cannot be used due their highly corrosive and toxic nature.

Hard mask etch

RIE of Si_3N_4 is done in a CHF_3/O_2 plasma and the etch rate is found to be 17 nm/min, comparable to that found in reference [93]. The following settings is used: $15sccm\ CHF_3$, $1sccm\ O_2$ at a pressure of 10 mTorr and RF power of $13W$. The samples are slightly over etched to achieve vertical side walls.

It is important that neither of the masks are too thick to cause shadowing effects, as illustrated in Figure 3.6. Small features require a thinner mask. All ions does not strike the surface perfectly vertically, with a thick mask only a small fraction of the ions will reach the etch surface which will reduce the etch rate [91].

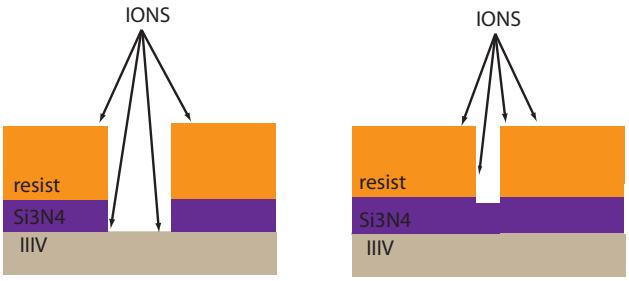

Figure 3.6: An illustration of the shadowing effect. The etch rate is reduced if the ions have limited access to the etch surface.

Semiconductor etch

Excellent anisotropy can be obtained for In-based compounds using reactive ion etching (RIE) with CH_4/H_2 mixtures. InP etching using CH_4/H_2 chemistry was first reported by Niggebrugge et al. in 1985 [94]. Most earlier studies on RIE of InP used chlorine-containing gas-mixtures [95]. However, chlorinated gases are toxic and corrosive and they etch photoresist and Si_3N_4 at significant rates [96]. The etch profile and surface smoothness do not meet the requirements either [97]. Also CH_4/H_2 plasmas have disadvantages. It is found that a low concentration of methane in the plasma gives a low etch rate, probably due to species depletion. As the concentration increases, the etch rate increases as well. When the methane concentration is increased above 20% the rate is decreased again. This is likely to be caused by the creation of a film of deposits on the surface. A. Carter et al. found that the film could be removed with O_2 plasma and assigned therefore the film to be organic [97]. The polymer film will even put the etch to a full stop if too thick. In order to avoid that the polymer is removed using an O_2 cleaning step in between each CH_4/H_2 etching cycle. A total of 45 minutes of CH_4/H_2 etching is used for the $340nm$ thick membrane. The etch rate is much lower for compounds containing aluminium [98]. In our epitaxial layout we have included a layer of InAlAs in the sacrificial layers to assist membranization. Due to the low RIE etch rate in this material the PhC holes are not etched trough that layer. Closest to the membrane layer there

is a $100nm$ thick InP layer to assist epitaxial growth. The holes are etched through the InP layer before the etch stops at the InAlAs layer. The ability to etch the holes slightly deeper than necessary improves the side walls of the holes. Figure 3.7 shows a SEM image of the etched PhC holes.

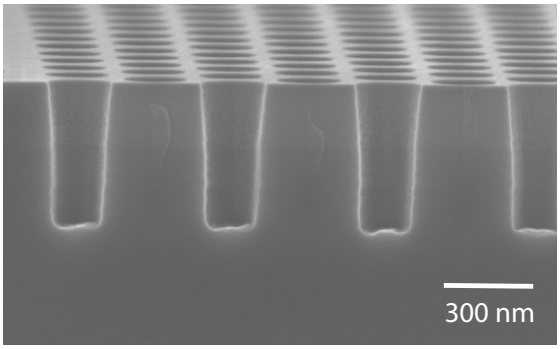

Figure 3.7: A SEM image of the a cleaved facet of the PhC pattern after the CH_4/H_2 - O_2 cyclic etch and hard mask removal.

3.4.2 Wet etch

The sacrificial layers below the membrane layers need to be removed in order to achieve a free standing membrane surrounded by air. In difference to the anisotropic RIE etch, it is desired that this etch is isotropic. All material 1μm below the membrane needs to be removed, and the only way to access the material is through the holes. A wet etch which etches not only downwards but also sideways is desired, to remove the material also in between the holes. Several issues may prevent a successful result, such as; poor isotropy, the creation of etch products which prevents further etching and membrane collapse. Therefore, this step required process development as discussed in this section.

It was found that InP alone could not be used as sacrificial layer. Efforts to etch InP sacrificial layers with $HCl : H_2O$ resulted in cylinders of removed material under each hole. Also for long etch times it was not possible to etch away the side-walls in between each cylinder. To open up a clear window under the membrane a layer of InAlAs was placed in the top part of the sacrificial slab.

The etch rate of $HCl : H_2O$ on InAlAs is much lower than for InP, but it is also much more isotropic. A thin layer of InAlAs, i.e. 100 nm, is enough to clear all material under the crystal. Once that is achieved, the wet etch has access to the full top area of the volume to be etched, so also a more anisotropic etch is capable of removing the remaining material.

When choosing thickness of the InAlAs layer, several factors needed to be taken into account. A thin layer is desirable to limit the creation of bi-products and to reduce the etch time. On the other hand, a sufficiently thick layer is required to open up a large enough window for further etch down into the InP. Figure 3.8 (left) shows a sample with too thick InAlAs layer ($800nm$), the sample have been etched for 5 minutes with $1HCl : 1H_2O$ and only $150nm$ of the sacrificial layer is etched. Figure 3.8 (right) shows a sample with a thin layer of InAlAs ($50nm$). The sacrificial InP material still remains under the PhC waveguide, even after a total etch time of 8 minutes $1HCl : 1H_2O$ with a HF clean after half the etch time. A likely explanation is that the wet chemistry could not access the surface sufficiently due to the narrow window, the problem is more critical under the waveguide where the distance between the holes is twice as long.

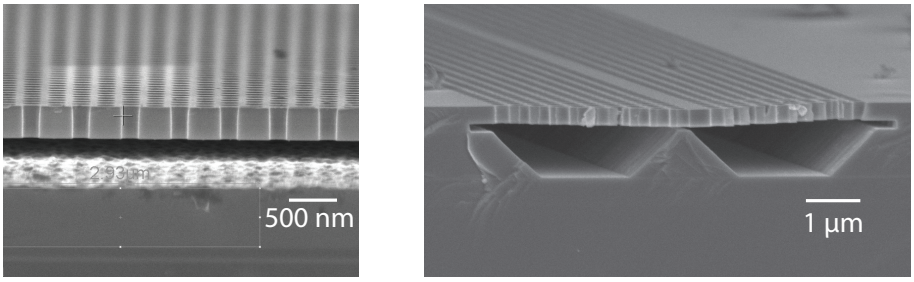

Figure 3.8: Two samples with different InAlAs thickness. Left: 800 nm. Right: 50 nm.

Unfortunately when wet etching the InAlAs layer, a bi-product is created which, if thick enough, hinders further etch. The composition of the bi-product is unknown, but it was found to be partly removed by HF. The samples were therefore iteratively cleaned in HF after each 5 minutes of etch in $HCl : H_2O$. This prevented the etch to stop, but the debris of the etch product was still visible

on the membrane, see Figure 3.9 (left). Khankhoje et al. have reported that they successfully removed an etch product believed to be hydroxide of aluminium in a solution of potassium hydroxide (KOH) [99]. Efforts to remove the debris with a $150s$ dip in KOH only left the surface in a worse condition, see Figure 3.9 (right). A $150s$ long KOH treatment of the sample did not remove the debris, and left the surface dirty in a non-uniform manner. This particular sample contained 5 layers of QDs (visible in the image) and the debris on the top surface is believed to be a result of etching the $200nm$ thick InAlAs sacrifical layer.

Samples with $100nm$ and $200nm$ thick InAlAs sacrificial layers were membranized successfully. But because it is not possible to remove all of the created bi-product a InAlAs thickness of 100 nm was used in the 10QW and 3QD samples to limit the debris thickness.

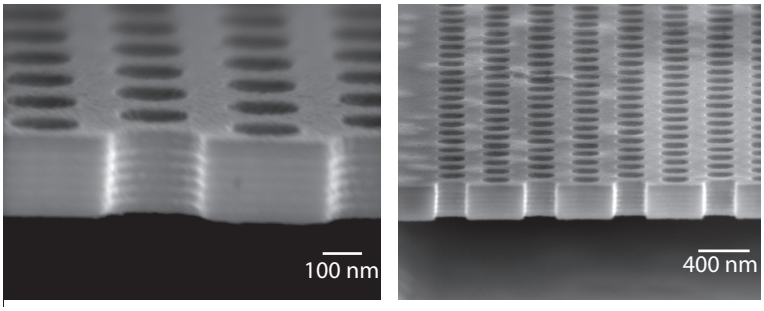

Figure 3.9: Left: SEM image at high magnification showing the debris on the top surface, created in the wet etch of the $200nm$ thick InAlAs sacrifical layer. The lines in the membrane are the active layers. Right: SEM image showing the surface condition of the same sample after a $150s$ dip in KOH.

Both HCl and H_3PO_4/HCl are very selective and etch the sacrificial layers at a fairly high etch rate while leaving the membrane practically untouched, due to the low etch rate in quartinary material. But the phosphor based etch causes the membrane to collapse while the hydrochloride based etch results in a free standing membrane even for crystals which are more than $30\mu m$ wide as shown in Figure 3.10. Neither of these two samples were dried in a controlled environment (in a critical dryer for example), only a gentle stream of nitrogen was used. As the aqueous solution under the membrane is evaporated out, attractive forces may cause the membrane to sink down towards the etch stop layer. It is believed to depend on

the surface condition. The problem could probably be avoided by drying the sample slowly in a humid environment.

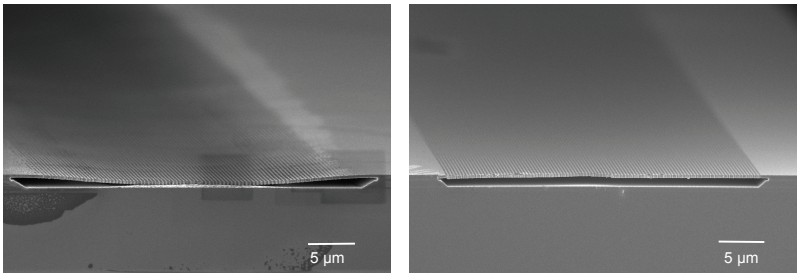

Figure 3.10: Identical samples on a wafer with a 200nm thick InAlAs sacrifical layer, the only difference is the wet etch chemistry. Left: H_3PO_4/HCl etch. Right: $HCl : H_2O$ etch.

Using a hydrochloric based etch the PhC membranes may be dried with nitrogen without it causing the membrane to collapse. This is an important property because the samples need to be dried several times during the wet etch procedure developed for these samples:

$\{$ 2 min HF + 1 min H_2O + N_2
5 min $1HCl : 1H_2O$ + 0.5 min $H_2O\} \times 3$

The first 2 minute HF etch removes the Si_3N_4 and the following three iterations of hydrochloric etch intervened with HF creates the free-standing membrane. If the sample is not dried before each HCl etch, then there could still be water left under the membrane, causing an uncertainty in $HCl : H_2O$ concentration in that region. Finally, the sample is inspected in an optical microscope where defects may be detected. However, a verification if all sacrificial material is removed under the PhC membrane requires a SEM imaging of a cleaved facet. Figure 3.11 shows the final device after cleaving, including the taper.

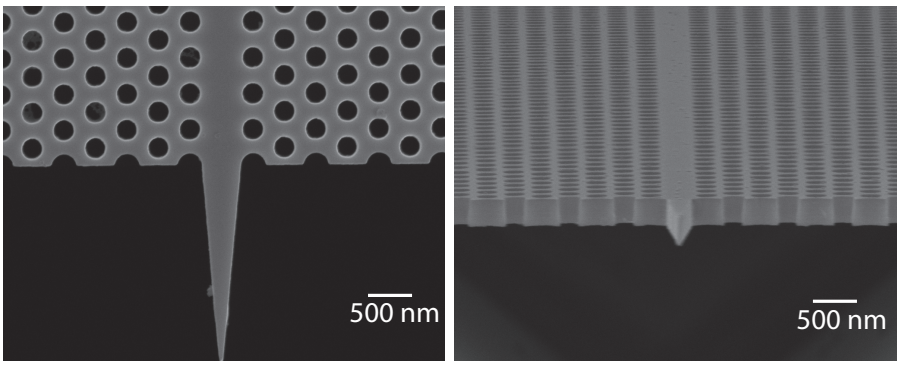

Figure 3.11: SEM image of 2D membrane PhC. a) Top view showing the linear waveguide defect. b) Sideview of a cleaved facet showing the free-standing membrane surrounded by air, for efficient confinement in the third dimension.

Chapter 4

Gain Measurements on Photonic Crystal Amplifiers

Many properties of the PhC waveguides presented in this thesis are directly related to the dispersion of the crystals. This chapter begins with a presentation of the measured group index of our samples using two different experimental methods. It is then followed by the main results of this work; an experimental demonstration of slow light enhanced amplified spontaneous emission (ASE) and gain in PhC amplifiers. The samples are optically pumped from the top, using a pulsed pump to limit heating. It is found, that including more QWs in the active layer of the membrane does not only increase the gain, but also the losses, thus a strong excitation is required. Gain measurements on 10 QW samples using highly energetic pulses of light are presented in Section 4.5. During strong excitation other effects such as the formation of localized modes occur at the band edge. The presence of localized modes, which are explained as random lasing, leads to a loss of carriers which will not contribute to amplification of the transmitted light. This can deteriorate amplifier applications if not properly controlled. It is therefore important to understand localized random lasers, which are also interesting in a fundamental point of view [100]. Random lasing results on the 10 QW PhC waveguides are given in Section 4.6.

4.1 Dispersion Measurements

Two methods were used to measure the dispersion. All dispersion measurements are done on 1 QW samples. First we present a method where the group index is extracted from Fabry-Pérot oscillations in the emitted ASE from active PhC waveguides. One limitation is that the method require devices of limited length without tapers. The second method utilizes a Mach Zender Interferometer (MZI) to measure the group index and samples of any length preferably with tapers can be measured [59]. However, the current measurement set-up at Thales Research and Technology does not allow for optical pumping of active PhC waveguides.

It is desirable to measure the group index on the same devices that are used for further characterization. The devices used in this project are up to $1mm$ long, making the Fabry-Pérot method unsuitable. Measurements on a shorter PhC waveguide which is an identical copy of a longer crystal, will give valuable information about the dispersion, and the spectral position at which the light is slowed down. However, each PhC waveguide suffer from fabrication imperfections so creating a perfectly identical copy is not possible. Furthermore, the imperfections cause propagation loss for slow light, so the maximum group index achieved in a short PhC waveguide might not correspond to the magnitude of the group index in a longer PhC waveguide [101].

4.1.1 Fabry-Pérot Measurement

As described earlier, all devices are equipped with tapers to improve out-and in-coupling and to suppress reflections at the end facets. Reflections will promote Fabry Pérot oscillations, undesired in amplifiers. However, the group index may be deducted from the Fabry-Pérot oscillations [29, 30], so in that sense they become useful. Short PhC waveguides terminated with a flat end-facets and air on both sides, were fabricated. The length of the crystals are $50\mu m$, which results in a fringe-spacing of about $0.6nm$ for a groupindex of 40, according to Eq. 4.1 below. That fringe-spacing is possible to resolve on the optical spectrum analyser at a resolution band-

width (RBW) of $0.1nm$. Using the wavelength spacing $\Delta\lambda$ between adjacent Fabry-Pérot peaks and the length L, the group index is calculated using:

$$n_g = \lambda^2/(2L\Delta\lambda) \tag{4.1}$$

The active sample to be characterized is pumped from above with $200mW$ of laser light with the wavelength $980nm$. The pump-light is focused onto the PhC waveguide using a cylindrical lens, more details on the pumping scheme is found in Section 4.2.1. When pumped, the active material in the membrane will spontaneously emit light, serving as an internal light source. The ASE will propagate through the PhC waveguide and a fraction of the light will reflect at the end facets. Interference effects will lead to the well known transmission spectra of Fabry-Pérot cavities, with a fress spectral range that depend on the length of the cavity and the group index. The ASE is collected at the output facet using a lensed fibre, a typical spectra and the corresponding group index is shown in Figure 4.1. Note that the oscillation period is not constant for all wavelengths, it becomes smaller for wavelengths approaching the band edge, reflecting the increase of group index as the band edge and the slow light region is approached.

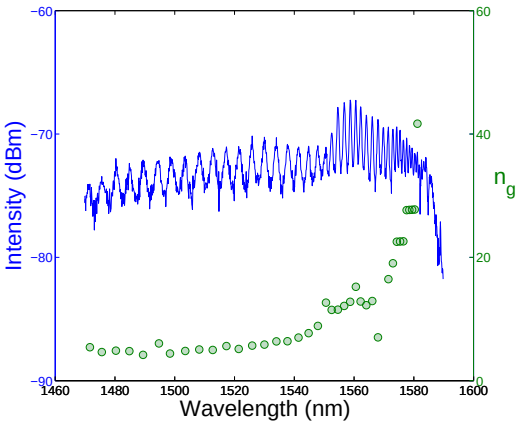

Figure 4.1: Spontaneous emission from a $50\mu m$ short PhC waveguide with a hole diameter of 210 nm and flat end facets (RBW= 0.1 nm). The deducted group index is shown in green.

The decrease in group velocity is significant close to the cut-off ($v_g = c/n_g = c/40$). The measured group index correspond nicely

with the theoretical predicted in Figure 2.1. A small spectral offset is seen due to slightly larger hole diameter in the fabricated device. One should be aware of defects such as random Fabry-Pérot cavities in the waveguide might cause narrow-spaced fringes, not necessary related to a high group index. Another drawback with this method is that special samples need to be fabricated only for this measurement. The short waveguides for group index measurements are fabricated only $100\mu m$ away from the $1mm$ long amplifier device, so that the processing of the two is as similar as possible.

4.1.2 Mach Zender Interferometer Measurement

Another method is to use a fibercoupled MZI [59]. A schematic of the set up is shown in Figure 4.2. Continuous wave light from a tunable laser is guided through the two arms of the MZI, the dispersive element (the photonic crystal waveguide) is placed in one arm. When sweeping the emission wavelength from the laser, the phase evolve differently in the two arms which produces a beating. The real part of the transfer function, $E(\omega)_{in} = E(\omega)_{out} * |T(\omega)|e^{i\phi(\omega)}$, is obtained by measuring the beating between the signal and the reference using two counter balanced detectors. The accumulated phase along a PhC waveguide of length L equals: $\phi(\omega) = k(\omega)L$, where $k(\omega)$ is the wavevector [102]. The group index can then be retrieved using the relation $v_g = \partial\omega/\partial k$. If the signal from the balanced detector drops, it might be difficult to tell if the drop is caused by changes in $\phi(\omega)$, or in transmission intensity $|T(\omega)|$. By performing a Fourier transform of the signal, also very high group indices, where transmission typically drops due to scattering, can be measured accurately.

Measured dispersion maps from 1 QW PhC waveguides are shown in Figure 4.3. The two dispersion maps are from $1mm$ long PhC waveguides with two different hole sizes. Transmission intensity is colour coded, where maximum signal is dark red, and dark blue is zero (logarithmic scale). Light is slowed down in the spectral region where the transmission through the PhC waveguide is delayed in time relatively the arm without a dispersive element. For the first waveguide (dispersion map to the left), this occurs at $1570 - 1590nm$. Due to the larger hole diameter in the second

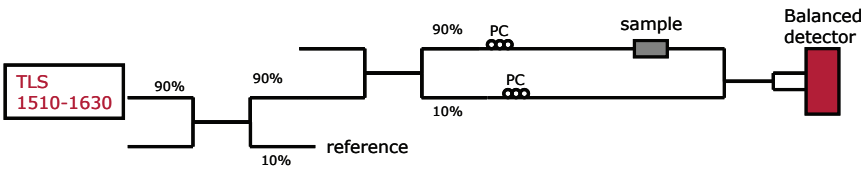

Figure 4.2: An illustration of the MZI set up for dispersion measurements.

waveguide (right), the slow light region is shifted to shorter wavelengths $1550 - 1570nm$. Because the length of the PhC waveguide is known, the group index can be derived from the measured time delay. Figure 4.3 (left): a delay of $15ps$ ($28ps$) at $\lambda = 1520nm$ ($\lambda = 1590nm$) results in a group index of $n_g = 4.5$ ($n_g = 8.4$). A similar group index was measured on the second waveguide. It is apparent from the dispersion maps that there is no transmission for wavelengths longer than a group index around $n_g = 8$, although higher group index is expected. As discussed earlier, slow light experience loss due to scattering because it is more sensitive to fabrication imperfections. However, it was not the only cause of the low group index for these samples. During the measurements the sample was imaged from the top with an IR camera. The propagating mode is seen as a bright line along the waveguide, arising from a certain degree of scattering which is present for all guided wavelengths. The out of plane scattering increased slightly for slow light, but not enough to be the main loss factor. It was evident that the slow light was absorbed in the un-pumped QW. The slow light mode could only be seen the first $200\mu m$ into the waveguide, after this point its scattered intensity faded out to zero. In an absorbing material, the absorption is expected to be enhanced by slow light. The measurement demonstrates that light with low group velocity is more stongly absorbed than fast light.

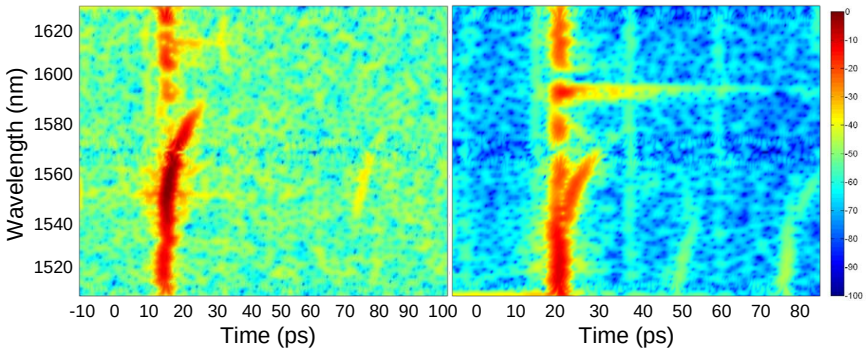

Figure 4.3: Time-wavelength map of two 1 QW waveguides. The colour code is normalized to the highest transmission. Dark red indicates 0 dB while dark blue indicates 100 dB. Left; lattice constant $400nm$ and hole diameter $210nm$, the same design as sample A (Section 4.3.1). Right; lattice constant $400nm$ and hole diameter $225nm$. The dispersive region moves $20nm$ in wavelength for the larger hole size, as expected.($15ps \rightarrow n_g = 4.5$ and $28ps \rightarrow n_g = 8.4$)

4.2 Experimental setup

It is challenging to couple light into waveguides with small cross-area. In Chapter 6, a free-space input beam is aligned after the amplified spontaneous emission, emitted from the SOA under electrical bias. When no bias is applied to an SOA, it turns into a photo detector. So once a rough alignment is achieved, the in-coupling may be optimized while measuring the photo current in the sample. However, optically pumped PhC amplifiers are unable to provide the same feed-back. For free-space coupling into the PhC waveguides, good imaging with a camera sensor sensitive to infrared light is desired. In this work we only had access to such a camera during a short period of time, which is the main reason why a fibre coupled setup was used. In many aspects, free-space optics is advantageous. The polarization is easier controlled and maintained in a free space set-up and light undergoes limited dispersion. Dispersion is not a problem in the measurements presented in this chapter, because continuous wave (CW) laser light is used. For short pulse experiments on the other hand, fibres might cause severe pulse broadening. Both setups are sensitive to the laboratory environment; free space optics are sensitive to dust and particles, while air fluctuations can cause movement in the lensed

fibres aligned to the device. To ease alignment a fibre-coupled setup was used, and we were painfully reminded too many times about the main drawback fibres have compared to free-space optics; the risk of the fibre crashing into the fragile PhC membrane.

Polarization control

It is important that the input light is linear polarized in the polarization state under characterization, most often TE. Because PhC waveguides are polarizing components, the polarization can be adjusted while studying the transmission through each waveguide using a manual fibre polarization controller. This holds for samples with good transmission and limited absorption. When the TE-polarized light is highly absorbed, for example in a multi QW sample, the polarization needs to be set before it is coupled into the device, and kept throughout the measurements. A polarization maintaining fibre preserves the polarization which is launched into it, making it a good choice for highly absorbing samples. In order to be able switch in between TE and TM polarized light in a controlled manner, a manual fibre bench polarization controller is used.

Transmission measurements

The light source used for transmission measurements is a CW tunable laser (Ando AQ4321D). The laser is synchronized with an optical spectrum analyser (Ando AQ6317B).

A schematic of the transmission setup is shown in Figure 4.4, light from the fibre coupled laser is polarization controlled, guided through the sample using lensed single mode fibres and finally detected. By sweeping the wavelength of the laser, while simultaneously measuring the transmitted light at the same wavelength, a transmission spectrum over a wavelength range of $100nm$ is obtained. Transmission measurements are preformed on the active samples while pumping at various powers, as outlined in Section 4.4.2. Gain measurements with a pulsed pump can with advantage be carried out with a more sensitive detection at the repetition rate of the pump.

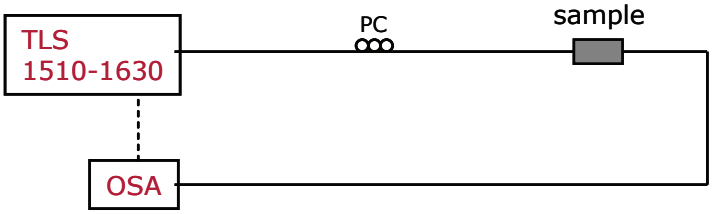

Figure 4.4: An illustration of the fibre-coupled transmission setup. Light from a tunable laser source (TLS) guided through the device under characterization and the output is detected on an optical spectrum analyser (OSA), synchronized with the TLS.

After filtering out the scattered pump light from the transmitted light, it is then detected with an InGaAs detector, connected to a lock-in amplifier. In this scheme the change of transmission induced by the optical pump is measured, hence the absolute gain can not be measured. Instead, a relative gain is derived. The relative gain is defined as the logarithm of the differential transmission normalized with the transmission at the lowest measurable pump power.

For PhC amplifiers designed with a mirror, i.e. only one taper, a fibre optic circulator is used to couple light in and out through the same fibre.

Measurement of the amplified spontaneous emission

The ASE is measured by collecting the emitted light from the pumped device using a tapered fiber. The amplified spontaneous emission (ASE) from an optically pumped sample provides a lot of information about its properties. A slow light enhancement can be seen in the ASE spectra, and the modal gain can be derived from ASE spectra accumulated while pumping different lengths of the PhC waveguide. In order to extract gain from the measurements, the pump lengths needs to be well defined and the power fluence as uniform as possible. The gaussian profile has a smooth transition between high and low intensity at the edge of the spot. In order to achieve a step-like transition between light on and off, a thin piece

of metal was placed as close to the sample as possible, partially shadowing the pump. Only the center part of the spot is used by positioning the pump spot so that the other tail of the gaussian profile falls outside the wafer edge. The optical pumping scheme is detailed in next section.

For measurements requiring better sensitivity, a liquid nitrogen cooled InGaAs spectrograph (Acton SP2500) was used. The spectral range of the cooled InGaAs sensor is $700 - 1600nm$.

4.2.1 Optical Pumping Scheme

Due to poor thermal conductivity of the quaternary material in combination with the free standing membrane quite severe pump-induced heating effects can be experienced. Actually, even to the point where the sample was burned. SEM images in Figure 4.5 show two burned samples. The one to the left was burned when pumped with $300mW$ continuous wave (CW) and the sample shown to the right was burned at the taper when trying to couple light with too high intensity into the waveguide. It was found that a maximum of $1mW$ can be focused onto the taper. It is therefore not possible to pump the device through the waveguide, unless short pulses are used.

The measurements were performed at room temperature and in order to reduce heating effects the pump was pulsed in most of the measurements. Two different lasers were used to optically pump the active PhC waveguides. To ensure efficient absorption, a pump wavelength which excites carriers into the InGaAsP barrier material is chosen. The first source is a laser diode emitting at $\lambda = 980nm$ with an output power up to $300mW$, it can be driven at continuous mode or using a pulse generator, resulting in down to $500ns$ long pulses at 1% duty cycle. The other source is a laser setup generating fourier limited pulses with a minimum duration of $150fs$ at a repetition rate of $250kHz$, emission wavelength $800nm$. The pulses are generated in a mode-locked laser (Coherent Mira 900 Ti:Sapphire). The output from the Mira is then amplified in a Regenerative Amplifier (RegA Coherent Ti:Sapphire), leading to high intensity output with a pulse energy of $4\mu J$. The laser system is

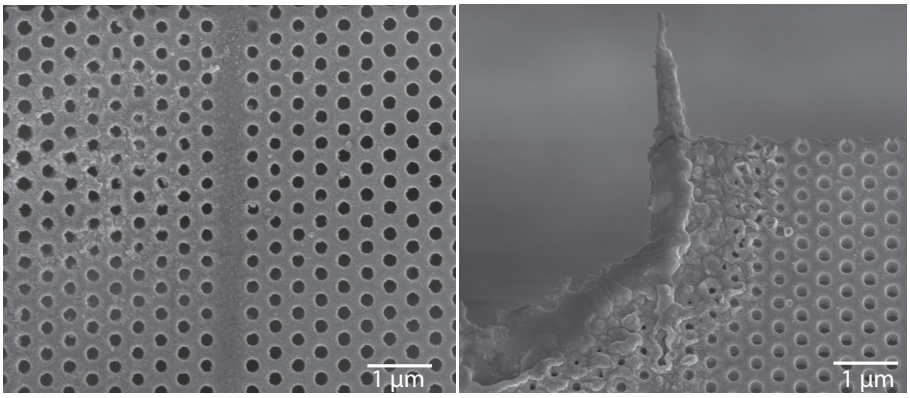

Figure 4.5: SEM images of 1 QW PhC waveguides, each during experiments. Left: burned when pumping CW with $300mW, 980nm$ from the top. Right: burned when coupling CW $2mW, 1550nm$ onto the in-coupling taper.

used also in Chapter 6, where experiments utilizing the full potential of the laser system are presented. For the PhC measurements in this chapter the output from the RegA is merely used to optically pump the device, because it offers more energetic pulses than the diode can offer. Only a small fraction of the full intensity is split off to be coupled into a fibre, a pulse energy of about $35nJ$ (corresponding to an average power of $10mW$) is used to pump the devices. Short pulse propagation through fibre causes pulse broadening, leading to an output pulse duration of about $1ps$, which still is short enough to avoid heating the sample.

A pump spot covering the full length of the device (up to $1mm$) is required, with tightest focus possible across the PhC waveguide (on the order of micrometers). There is limited space close to the sample because fibres needs to access the sample on both sides, and an imaging objective is limiting the space above the sample, see a photo of the set in Figure 4.6. Imaging using a visible, or an infrared camera is necessary to align and focus the pump spot onto the waveguide. It is essential to be able to pump and image the sample independently of one another, so a separate lens system was built for the pump. A long working distance microscope objective clears enough space for the following configuration: the pump light is collimated at the output of the fibre, using a commer-

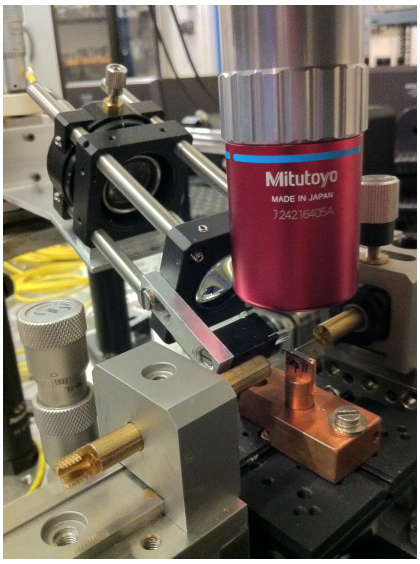

Figure 4.6: A photo of the optical pump scheme.

cial available collimation package (Thorlabs, F810FC-780). Within the focal length of a planar convex lens ($f = 38mm$), a cylindrical lens (f=20 mm) is placed. The cylindrical lens focuses light along one axis and its focal point is slightly misaligned with the convex lens' focal spot. The length of the spot is determined by the position of the cylindrical lens. The focal length of the cylindrical lens was chosen so that it can be mounted as close to the sample as possible without shielding the field of view through the microscope objective. The large diameter (7 mm) of the collimated beam ensures a tight focusing despite the relatively long focal length of the cylindrical lens.

All measurements in Section 4.3 and 4.4 are done with 980 nm diode as pump, while the measurements in Section 4.5 and 4.6 are done with RegA or MIRA respectively.

4.3 Enhanced Amplified Spontaneous Emission

A lot of interesting information can be deducted from the ASE emitted from active PhC waveguides. The spectral shape of the emitted light reveals the strong impact the band gap material has on the propagating light, see experimental study in Section 4.3.1. An enhancement of the ASE is observed close to the band edge of the fundamental mode. The enhancement is attributed to the decrease in group velocity for wavelengths approaching the band edge. Light within the slow light regime of the PhC will be enhanced because coherent backscattering and omnidirectional reflection increases the path length through the amplifying medium. The modal gain of the device determines how much the spontaneous emission is amplified as it propagates along the waveguide. For positive net gain, a longer propagation length results in higher output intensity; exponentially related to the modal gain. The modal gain of the device can therefore be extracted from ASE measurements acquired at many different, well defined, pump lengths; as presented in Section 4.3.2.

4.3.1 Experimental Study of the Slow Light Enhancement

In this section experiments aiming to demonstrate slow light enhancement of the amplified spontaneous emission are presented. Photonic crystals with a variation of lattice constants and hole diameters are used to show that the effect is consistent, and can be tuned to desired wavelength region by altering the photonic crystal design.

From weak to strong enhancement

The PhC has a pronounced effect on the emitted light from the QW, as shown in Figure 4.7 (left). The figure shows emission from three different waveguides with different hole sizes, located only

$200\mu m$ away from one another on a 1 QW wafer, when pumped with $200mW$ from the 980 diode (CW). All spectra are normalized and plotted with an offset for clarity. Only the smallest diameter is designed to exhibit strong photonic crystal effects, the others show very weak or close to no effects due to the large holes. The different spectra differ significantly; the QW peak at $1525nm$ can be seen in all spectra, but as the holesize decreases the spectral shape changes drastically. ASE from the crystal with a hole diameter of $210nm$ show a strong enhancement for wavelengths around $1590nm$, after which the intensity abruptly drops due to the PhC band edge. It is known from the dispersion measurements that the wavelength region where the enhancement occurs overlaps with the slow light region of the crystal, see the group index measurement of this PhC design in Figure 4.1. It is also noted that the band edge is shifted to longer wavelength when the hole diameter is decreased, as expected. The peak about $10nm$ away from the band edge is TM polarized light, verified in the measurements presented in Figure 4.9 below.

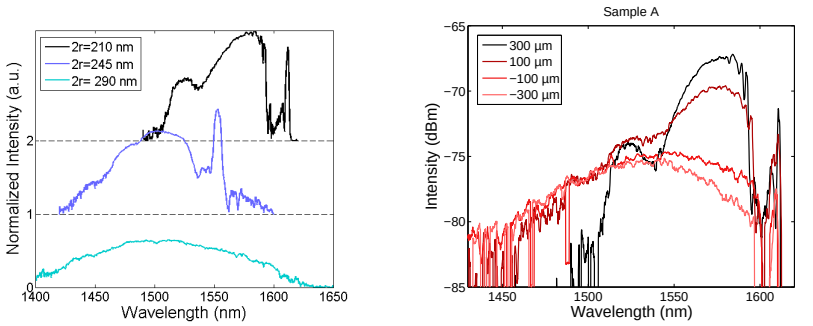

Figure 4.7: Left: Spontaneous emission from three different 1 QW waveguides with hole diameters of 210, 245 and 290 nm. Pump alignment and pump intensity are comparable between the samples (Pump: 980 nm diode, power $200mW$ CW). The curves have been offset for clarity. Right: Further study on the waveguide with a hole diameter of 210 nm. ASE at different pump length, the legend indicates the central position of the $1mm$ long pump spot where 0 is at the out-coupling taper.

Dependance on pump length

Figure 4.7 (right) shows the effect altering the length over which the sample is optically pumped ($200mW, 980nm$, CW), thereby

effectively varying the waveguide length over which spontaneous emission is generated. The PhC waveguide with a hole diameter of $210nm$ from Figure 4.7 (left) is used. The whole pump spot is moved along the waveguide in these measurements. First it is severely shifted out over the fibre collecting the ASE and then it is stepwise shifted inwards to pump a longer section of the PhC waveguide, to finally cover almost the full $1mm$ device length. When pumping only the very tip of the PhC waveguide the emitted light is barely affected by the band gap of the PhC and the spectrum is close to pure QW emission. As the pump length increases, the enhancement increases dramatically in the slow light region. Also the low, as well as high energy cut off, becomes more apparent. The results of these measurements confirm our interpretation that the photonic crystal dispersion enhances the ASE.

Variation of pump power

1 QW

A study of the ASE as a function of pump power is presented here, aiming to compare the emission from the PhC waveguide with that from the wafer itself. A better detection sensitivity is required to be able to measure at very low pump powers, the OSA was therefore replaced by the cooled InGaAs spectrograph in these measurements. Measurements on a PhC fabricated on the same 1 QW wafer, but with smaller hole diameter is used to show the tunability of the slow light enhancement. Figure 4.8 shows the ASE from a PhC waveguide, sample B, with its band edge at $1558nm$, and ASE from the wafer, measured close to the waveguide. Both are measured at pump powers ranging from $7 - 125mW, CW$. When measuring the emitted light from the wafer itself, the fibre is aligned to be in level with the active layer, and focus is adjusted (distance between fibre and wafer) to optimize in-coupling into the fibre. There is no defined waveguide in the bulk wafer. However, the pump spot is a narrow line, identical to the one used for pumping the PhC waveguide, and light is detected at the cleaved facet. This means that light is very weakly guided, which is why the emission from the wafer also is denoted ASE.

Looking closer at the measurements in Figure 4.8 b), heating is seen as a red-shift of the spectral features (about $2nm$) between the low and high pump powers. For the bulk wafer (a) heating is not as big of an issue, because heat can dissipate down into the wafer, and does not accumulate in the pumped region as it does in air-slab. Heating of the membrane cause carrier loss. Studying the ASE normalized with the ASE_{wafer} displayed in c), an amplification of $2-4$ times can be seen over the full spectra, with the maximum 4-fold enhancement in the slow light region close to the band edge. The spectral shape shows a clear signature of the photonic crystal dispersion.

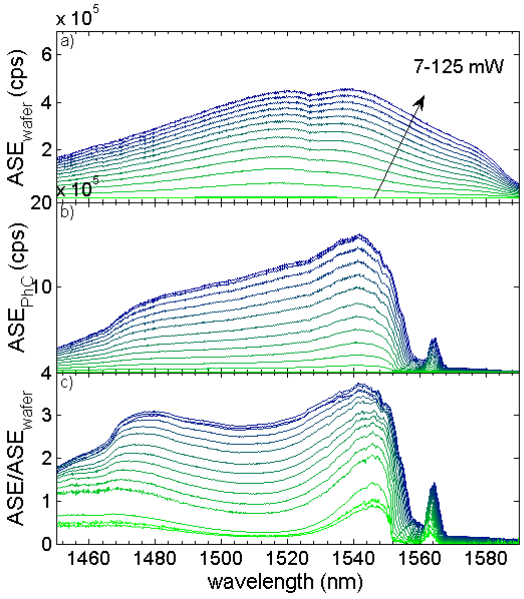

Figure 4.8: a) ASE spectra from the 1 QW wafer at CW pump powers ranging from 7-125 mW (980 nm) b) ASE spectra from sample B c) The normalized ASE, showing the PhC dispersion influence on the spectral shape and an enhancement in the slow light regime. (cps = counts per second)

In Figure 4.8 b) a peak about $10nm$ away from the band edge is apparent. Its relative intensity compared to the slow light emission is less here than in previous measurements. The reason is because a half wave plate is now placed in front of the free-space coupled spectrograph such that mainly TE-polarized light is detected. The emission from the QW at the wafer edge is highly polarization de-

pendent. A half wave plate is placed in front of the detector, and it is aligned to optimize the signal from the wafer, corresponding to TE polarization. A quarter wave plate is placed in front of the half-wave plate to ensure planar polarized light. The TE and TM polarization state of the emission can then be measured independently, Figure 4.9 shows both polarizations of the ASE emission from sample B. It is clear that the peak is TM polarized light, and not a part of the TE fundamental mode. As seen in the dispersion diagram for TM polarized light in Figure 2.4, TM modes close to the TE fundamental mode exist. The observed TM peak is assigned to be a spectrally narrow slow light region of a TM mode.

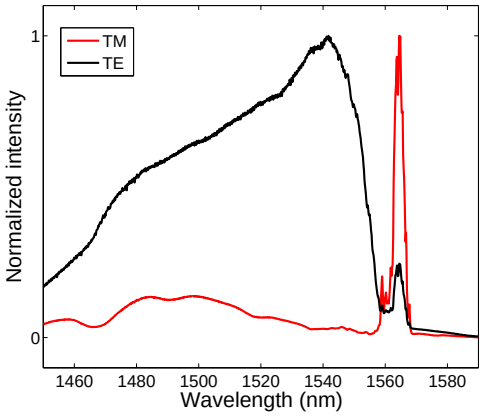

Figure 4.9: ASE from sample B (1 QW), collecting the TE (black) and TM (red) polarized part of the emitted light respectively. Pumped with $200mW$ CW using the 980 nm diode in continuous mode.

10 QW

A power dependance series with comparison of the wafer emission was carried out on 10 QW samples as well. Figure 4.10 shows measurements on a PhC waveguide with its band edge located at $1580nm$, which is a big offset to the center QW emission at $1540nm$. This sample is from here on referred to as sample C, as further measurements on the same waveguide will follow. Figure 4.10 (left) shows the ASE when pumping with 980 nm diode, CW $7-125mW$, identical to the pump scheme used for sample B (1 QW) in Figure

4.8, in order to make them directly comparable. When comparing the ASE from the wafer (ASE_{wafer}) with the ASE from the PhC (ASE_{PhC}) an obvious shift of the peak intensity can be observed. That the maximum of the ASE_{PhC} overlaps with the slow light regime, rather than the material gain maximum. The emission

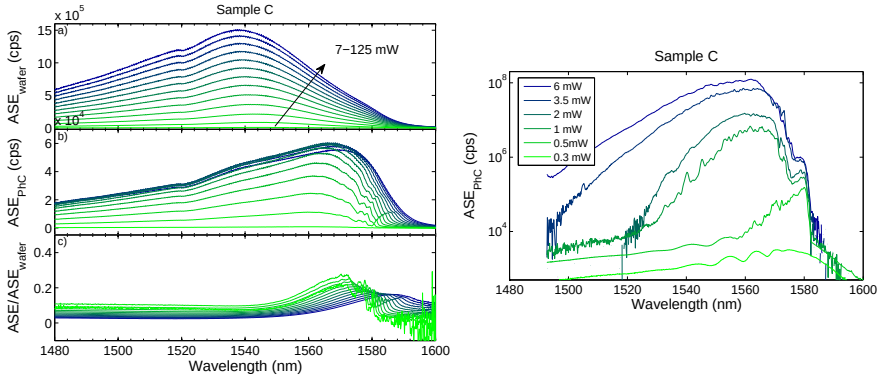

Figure 4.10: Left: a) ASE spectra from the 10 QW wafer at CW (980nm)pump powers ranging from 7-125 mW b) ASE spectra from sample C (10 QW) c) The normalized ASE. Right: ASE spectra from sample C (10 QW) when pumped with RegA (1 ps pulses, repitition rate 270 kHz), the legend shows the average power.

from the 10 QW wafer shows three times higher intensity than the emission from 1 QW. The fact that the pump powers are identical for the single and multi QW wafer, means that the same amount of carriers are absorbed in the two cases. With more wells in the membrane the possibility for carriers to be captured in one of the potential wells increase. This leads to more carriers contributing to the spontaneous emission in the multi QW wafer than in the wafer with a single well, hence a stronger 10QW ASE_{wafer} signal. The emission from the wafer is predominately SE, because there is no waveguide present.

The captured carriers are distributed in the 10 QWs, leading to a lower carrier density in each well. The emission from the 10 QW PhC sample C is much weaker than the emission from the wafer itself, seen in magnitudes of the ASE spectra and also in Figure 4.10 (left c). That indicates that an inversion is not achieved and the material is in the absorption regime. The ASE emission is then expected to be low, and the collected emission could be mainly

spontaneous emission from the region closest to the out-coupling taper. For the wafer, SE is emitted from a larger spot than from the PhC waveguide where only limited SE is expected from the PhC cladding regions, hence a higher SE intensity is expected from the wafer. More loss is expected in the PhC than in the wafer for two resons; firstly, the PhC suffers from more heating than the bulk wafer, where heat can dissipate down into the wafer. Heating causes a spectral red-shift, and by looking at the spectra Figure 4.10 (left b) a $6nm$ shift can be seen. Secondly, the large matrix of holes etched through the active medium in the PhC cause surface recombination. Surface recombination is known to be a big loss factor in these samples, since they are not passivated.

The 1 QW ASE_{PhC} signal from sample B is larger than the ASE_{PhC} from 10 QW sample C (about 30 times more) because a population inversion is achieved, so the SE is amplified as it propagates through the 1 QW waveguide. Surface recombination is just as an important loss factor for a 1 QW sample as for a 10 QW sample. It is proportional to the carrier density, however at high carrier densities (as achieved in the single QW) the surface states begins to saturate [103].

Figure 4.10 (right) shows the ASE_{PhC} from sample C, when pumped with short, highly energetic pulses from the RegA. The average power of the $1ps, 270kHz$ pulse train is indicated in the legend. At similar average pump powers, the output intensity increases with three orders of magnitude when pumped with RegA compared with the CW 980 diode. The higher ASE intensity when using a short pulse excitation indicates that during a time window, corresponding to the carrier lifetime after the pump pulse have excited the material, net gain is achieved due to the large carrier density. From these measurements it is concluded that the 10 QW samples require the high pulse energy from the RegA in order to enter the gain regime.

4.3.2 Gain Measurements

Modal gain can be extracted from ASE measurements from waveguides of different length. One would like to avoid deriving gain from a range of PhC waveguides with different length, because the

propagation loss might vary between samples due to local irregularities in the crystal. Instead, different lengths of the waveguide are pumped, a technique which have been used to measure gain in bulk material [104] and also for electrically pumped SOAs with the help of segmented contacts [105].

The different lengths at which the device is pumped is denoted l, while the total length of the device (or the longest pump length) is denoted L. If pump efficiency, coupling-, and detection loss are all included in the constant A; the detected intensity $I(x)$ can be written as:

$$I(x) = I_s A \int_0^L e^{gx} dx \tag{4.2}$$

where g is the net gain, including all loss mechanisms, and I_s is the density of spontaneous emission generated at each segment dx. By integrating over the pump length l the total detected ASE is obtained. A normalized intensity I_{norm} defined by dividing the intensity at a given length $I(l)$ with the full length intensity $I(L)$, will cancel out the prefactors $I_s A/g$. We end up with only one unknown; the net gain (Eq. 4.4). The gain which best match the measurements is extracted when fitting Eq. 4.4 to the experimental measured data.

$$I(l) = \frac{I_s A}{g}(-1 + e^{gl}) \tag{4.3}$$

$$I_{norm} = \frac{I(l)}{I(L)} = \frac{-1 + e^{gl}}{-1 + e^{gL}} \tag{4.4}$$

A series of measurements with different pump lengths are done using the cooled InGaAs spectrograph. The pump is pulsed to reduce heating; pulse duration $500ns$, period $50\mu s$. The length is defined by blocking part of the pump spot using a thin piece of metal, and the absolute value of the length is later deducted from calibrated microscope images from an IR camera. A $1400nm$ longpass filter is inserted on the microscope, so that only PL from the wafer is visible on the camera image. A good IR camera is a very helpful tool when aligning the pump, and also to accurately measure the pumped length.

The measured data from sample B and the extracted gain is shown in Figure 4.11 (left). A gain up to $38cm^{-1}$ is measured, with a clear

enhancement in the slow light region. The gain of 1 QW semiconductor optical amplifiers is typically $10cm^{-1}$ [34]. In these samples the thin membrane confines the mode more than in a conventional ridge waveguide, so a slightly higher gain is expected because of the higher confinement factor. However, the increase of gain to a value of $40cm^{-1}$ is believed to be a result of the light slow down.

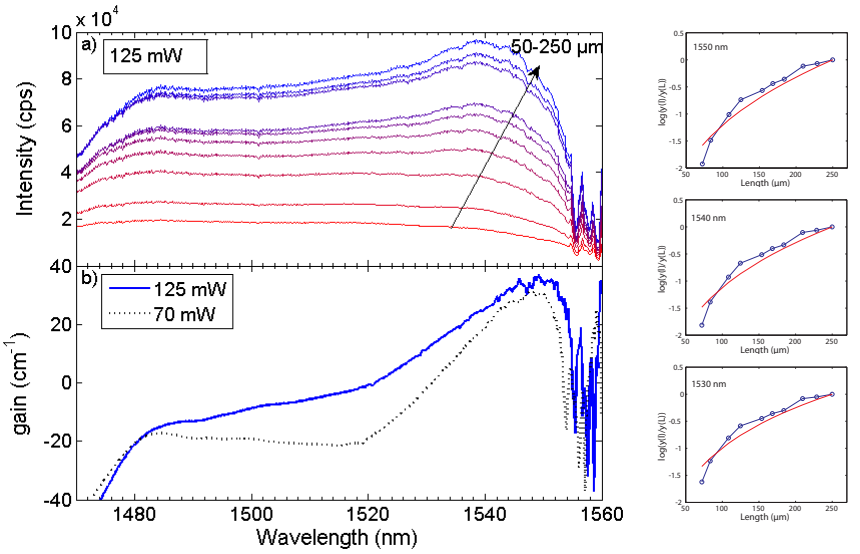

Figure 4.11: Left: a) ASE spectra measured while pumping different lengths of the PhC waveguide (sample B, 1 QW). Pump power 125 mW peak power, pulse duration $500ns$, period $50\mu s$, wavelength $980nm$. b) the extracted gain for $125mW$ and $70mW$ pulse peak power. Right: Measured data (blue) and fit (red) for three representative wavelengths (1530, 1540, 1550 nm

.

4.4 Enhanced Transmission

Transmission measurements of active PhC waveguides as a function of pump power are presented in Section 4.4.2. Due to heating of the lattice when pumping continuously, a pulsed pump is required for those measurements. It is not possible to observe a change in transmission on a the OSA, which detects the incoming signal continuously, when the device is pumped only a fraction of the time. A lock-in amplifier, locked at the pump frequency, is therefore

used instead. In Section 4.4.1, transmission spectra from samples with various configurations of absorbing material are presented and discussed.

4.4.1 Transmission Measurements

1 QW sample

By using tapers the Fabry-Pérot oscillations which are caused by reflection at the end facets are suppressed, shown in Figure 4.12. The measurements are done on a $1mm$ long 1 QW PhC waveguide and the total transmission through the device with tapers is 5.6%.

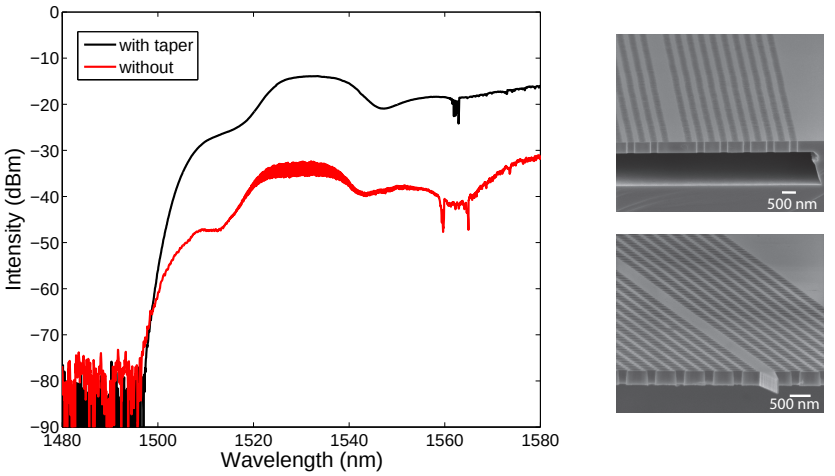

Figure 4.12: Measured transmission spectra from an un-pumped 1 QW PhC waveguide with (black) and without (red) taper. Right: SEM picture of the sample without and with the mode adapting taper respectively.

10 QW samples

Transmission measurements were done on multi QW samples as well. Because of severe absorption of TE polarized light propagating down the un-pumped material, no transmitted TE polarized light can be detected on the OSA. Instead, TM polarized light

shows high transmission at wavelengths beyond the material absorption. Figure 4.13 shows the transmission spectra of 10 QW PhC waveguides with different lattice constants. The green spectra (lattice constant $a = 380nm$) is measured on sample C, which has been introduced earlier. The clear dip in the spectra is assigned to the TM minigap shown in the TM dispersion diagram in Figure 2.4. The width of the dip is about $5nm$, which match well with the calculated value. The fact that the transmission shows a sharp drop, and display low loss transmission on either side of the minigap makes it interesting for filter applications [106]. The TM minigap is beyond the band edge for the fundamental mode, but still within the TE band gap. Hence, light with a wavelength within the TM minigap is inhibited to propagate, independent of polarization.

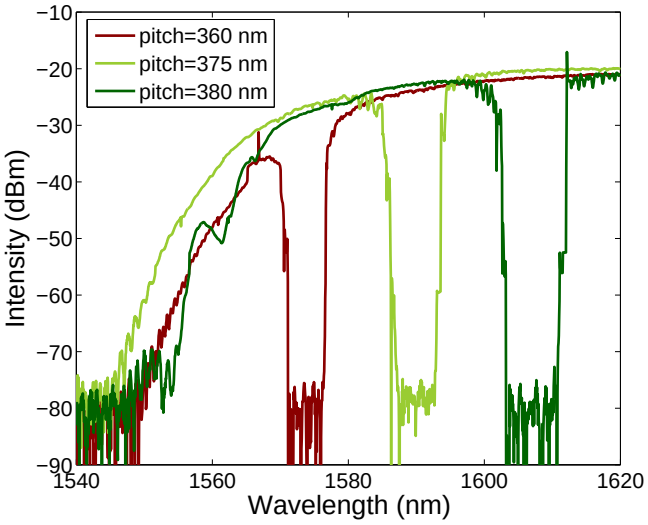

Figure 4.13: Transmission spectra from un-pumped 10 QW waveguides with different lattice constants. The green spectra with $a = 380nm$ is measured on Sample C.

3 QD samples

To study the filter-effect further a PhC sample with three layers of QDs, is investigated. The same dip occur in the transmission spectra and the spectral position can be precisely tuned by altering

the design parameters of the PhC. The dispersion maps, acquired from the MZI setup outlined in Section 4.1.2, from the 3QD sample are displayed in Figure 4.14.

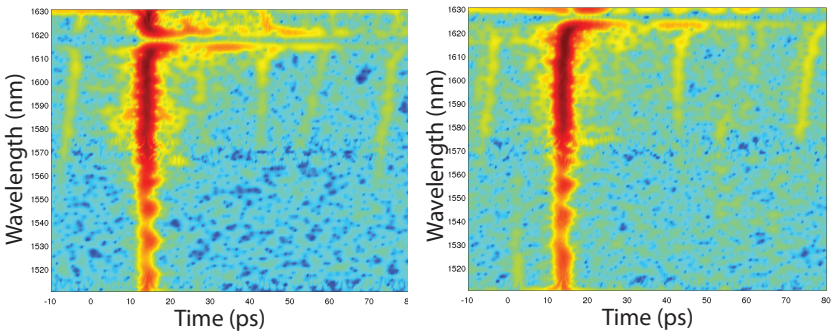

Figure 4.14: Time-wavelength map of two un-pumped 3 QD waveguides with a lattice constant of 385 and 390nm respectively. Bright red indicates high signal (log scale). The TM minigap shifts in wavelength as predicted in the PhC design.

The dip is clearly visible in the dispersion map, and the expected wavelength shift with increasing lattice constant is seen when comparing Figure 4.14 a) and b). The spectral width of the minigap corresponds to the measured spectra in Figure 4.13. On each side of the dip there is a narrow region of slow light. This is expected for the TM minigap, where the slope of both modes defining the gap decrease close to the band edge in the dispersion diagram shown in Figure 2.4. Also the spectral width of the minigap is predicted in the dispersion diagram. Both waveguides show strong transmission also for large delays, i.e. light with low group velocity. A group index of $n_g = 20$ is achieved in the measured sample.

4.4.2 Relative Gain

The transmission spectra in the previous section are all measurements without pumping the active material in the sample. Pumping the sample continuous wave lead to net modal gain, as shown in the ASE measurements. There are several competing effects; high pump powers leads to an increase of carriers, but also more heating.

Slow light propagates an efficiently longer path length through the active material, and enhances the positive or negative net gain. It turns out, due to severe heating of the material when pumped CW, it is not possible to detect an increase in transmission on the OSA.

Heating of the sample is reduced by using a pulsed pump. Using a pulse generator, the laser diode can operate in pulsed mode with a pulse duration of $500ns$ and a period of $50\mu s$. Because the sample is now illuminated only 1% of the time, it is still difficult to resolve a change in transmission using continuous detection. Instead, light modulated at the repetition rate of the pump laser is detected using an InGaAs detector connected to a lock-in amplifier. From the measurements a relative gain can be derived. The differential transmission signal at different pump powers was normalized with the signal at the lowest measurable pump power:

$$RelativeGain = 10log_{10}(\frac{trans_{pump} - ASE}{trans_{lowestpump}}) \tag{4.5}$$

A sample which has its slow light region within the range of the tunable laser, yet still beyond the wavelength for maximum material gain, is chosen. The ASE and transmission spectra in Figure 4.15 a) is from a 1 QW sample with a lattice constant of $400nm$ and hole diameter of $220nm$. As expected from the dispersion diagram for this design, the measurements show that the band edge is at $1600nm$. Despite the fact that the wafer emission is centred around $1520nm$ for this 1QW wafer, the PhC waveguide show higher relative gain close to the band edge of the guided mode, which corresponds to the slow light region.

Relative gain measurements were carried out on 10 QW and 3 QD PhC waveguides as well. The fact that the TE mode was fully absorbed in a 1 mm long un-pumped 10QW or 3QD waveguide implies good absorption, which also implies that a large gain should be achieved with appropriate pumping. The increase in transmission when pumping the waveguide at different pulse peak powers is shown in Figure 4.16 (left) for 10 QW and Figure 4.17 (left) for 3 QD.

These measurements show a maximum relative gain of 17 dB (1 QW), 13dB (10 QW) and 15dB (3 QD) in $1mm$ long devices pumped with $500ns$ pulses with a peak power of $300mW$, and wavelength

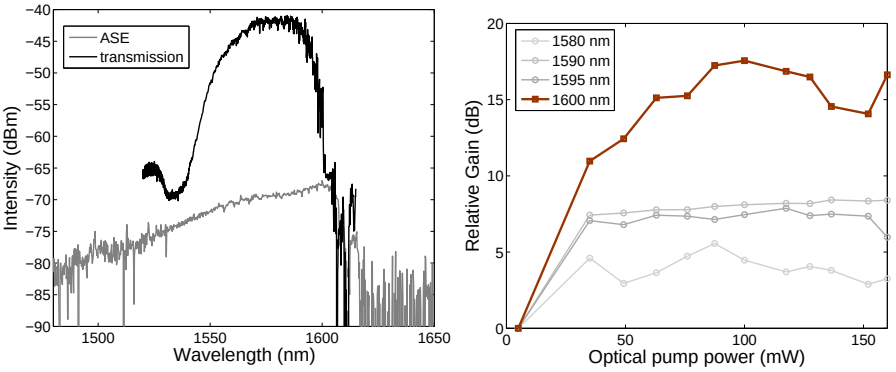

Figure 4.15: Left: ASE (pump: $200mW$, $980nm$, CW) and transmission (un-pumped) showing the band edge at $1600nm$ of the 1 QW sample. Right: Relative gain gain measurement showing highest relative gain in the slow light region. The pump-power levels at the x-axis indicate the peak power of the $500ns$ long pulses from the $980nm$ diode.

$980nm$. The 10 QW sample is most likely still below transparency in these pumping conditions, according to ASE power series with 980 diode in Figure 4.10 above. The relative gain for the different samples (Figure 4.15, 4.16 and 4.17) cannot be directly compared with one another because the extracted gain depends on the lowest power measurement relative to which the measurements are performed. However, it is clear there is no tendency of saturation, so by increasing the pump power the relative gain is increased.

4.5 Gain Measurements with Short Pulse Excitation

Two actions were made to improve the gain measurements; shorter 10 QW devices were fabricated, and the diode laser pump was exchanged to the output from the RegA which is fed by a mode-locked Ti:Sapphire laser (MIRA). Light propagating through a shorter device is expected experience less scattering induced loss, but also less amplification. As a consequence of shortening the device, the pump can be more tightly focused into a smaller spot, thus increasing the pump fluence on the pumped area. Because the device length is

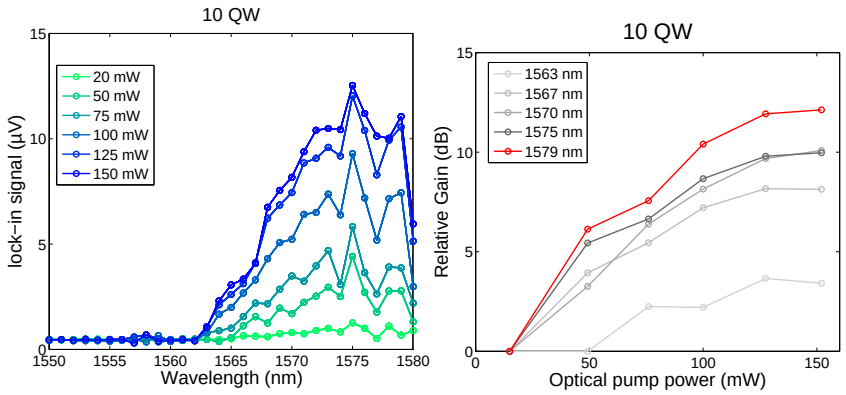

Figure 4.16: Left: Change of transmission for the 10 QW PhC waveguide at several different pump powers. Right: the derived relative gain. The indicated pump-power levels are peak power of the 500ns long pulses from the 980nm diode.

limited by how narrow the InP material can be cleaved accurately, the device design is modified to obtain shorter devices. The PhC waveguides are now equipped with a taper in one end to improve coupling and reduce residual reflection, and terminated with a PhC mirror in the other end. Calculations of the reflection coefficients based on finite difference time domain in 2D indicate close to 100% reflectivity for all wavelengths in the guided mode. The device is illustrated in Figure 3.3 (right). From now on this device design will be called a semi-closed waveguide. Transmission measurements can be done by accessing the taper with a fibre circulator. There is a trade-off between reducing propagation loss and optimizing light amplification when choosing length of the amplifier. Here, the amplifiers are made 200 or 300μm long, hence a propagation length of 400 or 600μm. The following measurements on short amplifiers pumped with RegA (800nm and about 1ps pulse duration at a repetition rate of 270kHz) are presented.

4.5.1 Semi-Closed Waveguide

In this Section a series of measurements performed on the same sample are presented. The sample, which is named sample D, is a 200μm long 10 QW PhC semi-closed waveguide.

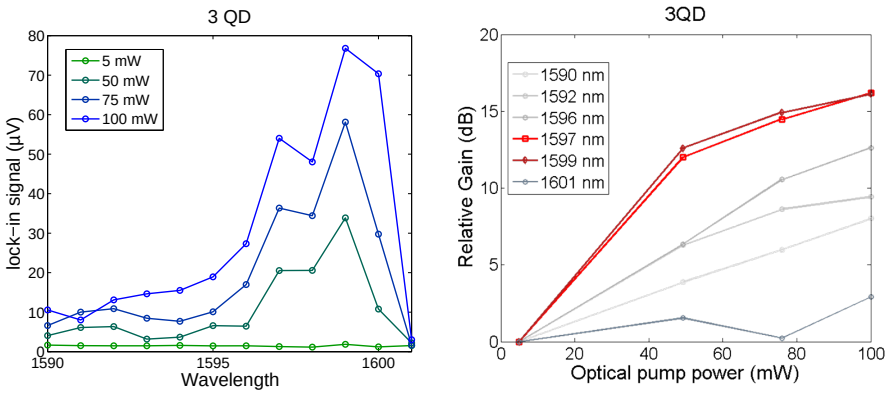

Figure 4.17: Left: Change of transmission for the 3QD PhC waveguide at several different pump powers. Right: the derived relative gain. The indicated pump-power levels are peak power of the 500ns long pulses from the 980nm diode.

ASE

ASE measurements are done using the 980 CW pump, to be able to compare with sample C above. The ASE spectra from the wafer and sample are presented in Figure 4.18. As seen in earlier samples, the ASE emission is strongly influenced by the PhC dispersion. The emission is greatly enhanced in the region close to the band edge at 1588nm (the slow light region). The difference between sample D and sample C, is that ASE_{PhC} saturates at long wavelengths first (corresponding to the slow light region). This is expected due to gain saturation caused by band filling, however not clearly observed in sample C. An alternative explanation could be that a higher group index is achieved in sample D, increasing the gain sufficiently to make the effect visible in the ASE spectrum. This would require the ASE to be so strong that it saturates the gain itself, and that is not likely to be the case.

Transmission

Transmission measurements were also carried out on sample D in reflection, using a fibre circulator. TE polarized light was coupled into the sample and collected through the same fibre. More interfer-

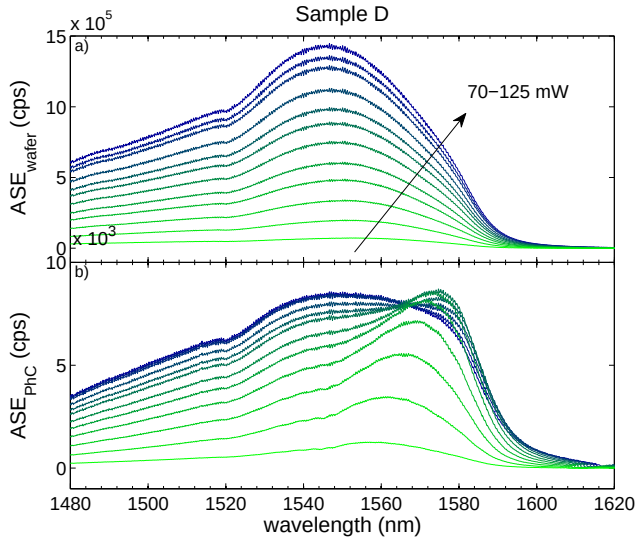

Figure 4.18: ASE spectra from the wafer and 200μm long semi-closed sample D respectively (10 QW). Pump: 980 nm diode, CW at powers ranging from 7-125 mW.

ence can be seen on the transmission spectrum from a semi-closed than from an open waveguide. The higher reflectivity of the closed end of the waveguide sets higher demands on having a low reflection at the taper to maintain a low product of the two. Transmission spectra as a function of pump power is shown in Figure 4.19. Due to the shorter propagation length in sample D, compared to sample C, the TE polarized fundamental mode is not fully absorbed, and transmission can be measured also without pump. The lower graph in the figure shows the change in transmission normalized with the transmission without pump. At wavelengths in the fast light regime of the guided mode the pump cause additional loss, and gain is not sufficient to overcome the losses, resulting in a lower transmission when pumping. The fringes occur at the same wavelength for the different pump powers so there is only limited heating of the crystal lattice. However, there is a wavelength shift at the cut-off. The pump cause a small increase of the InGaAsP refractive index and the PhC band edge shifts in wavelength as a function of the refractive index, as seen in Figure 2.3. The observed shift of 3nm corresponds to a refractive index shift of order 10^{-2}, which is a realistic pump induced change. For 10 QW gain material, pumped with an

average power of $8mW$, high enough amplification is achieved so that it can be detected on an OSA (continuous operation) despite the low repetition rate of the pump laser.

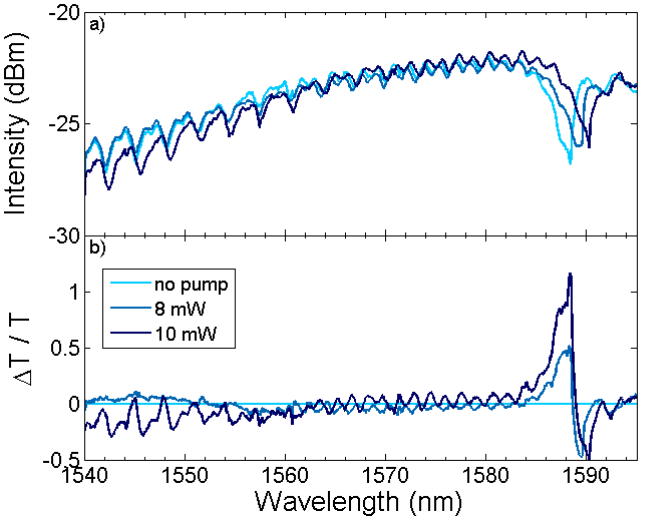

Figure 4.19: a) Transmission spectra from Sample D (semi-closed 10 QW) for different pump powers. The legend indicates the averaged power of the pulsed pump from the RegA. b)The normalized change in transmission plotted as a function of wavelength.

Lock-in measurements

If the OSA is exchanged for an InGaAs detector connected to a lock-in amplifier, more sensitive measurements can be carried out by detecting transmitted light at the same frequency as the repetition rate of the laser. The pump-induced changes in transmission are thereby more directly probed, and the amplification is not washed out by detecting also when there is no pump present. Lock-in measurements of sample D are presented in Figure 4.20 (left). The ASE signal, which is measured when the tunable laser is off for each pump power, is subtracted. Transmission is measured at a large range of wavelengths, and the lock-in signal is measured at each wavelength. The lock-in signal is very wavelength dependent with a maximum signal in the slow light regime, close to the band edge.

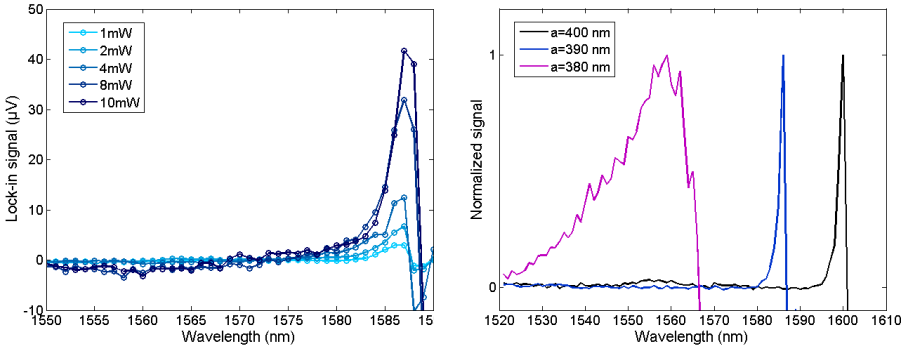

Figure 4.20: Left: Change of transmission at several different pump powers, average power of the RegA pump noted in the legend. Sample: 10 QW semi-closed (sample D) Right: lock-in measurements on 10 QW samples with different lattice constants, each normalized with its peak value. A high transmission correlate with the slow light region of each crystal.

To show the correlation with slow light region, lock-in measurements on waveguides with band edges located at 1600, 1588, and $1566nm$ are presented in Figure 4.20 (right). All samples are located on the same chip, so the gain material is identical. The study shows that the wavelength region of high transmission scales systematically with the variation of the structural parameters of the PhCs.

Gain

Gain measurements, similar to the gain measurements outlined in Section 4.3.2, were performed on semi-closed waveguides too. The semi-closed configuration calls for a modification of the equations. Consider a semi-closed waveguide, pumped a certain length l from the taper and in over the waveguide, as illustrated in Figure 4.21. In the following relations gain and absorption in the pumped and unpumped regions respectively are denoted with g and α. Light generated within a small fraction, dx, can propagate towards the taper and then be amplified along the way, indicated with a blue arrow and corresponds to $I(x) = I_s A e^{gx}$. It might also propagate the opposite direction and experience both amplification and absorption on its return trip towards the output taper. The propaga-

tion can be divided into three steps as indicated in Figure 4.21; green: $I(x) = I_s A e^{g(l-x)}$, red: $I(x) = I_s A e^{-2\alpha(L-l)}$ and black: $I(x) = I_s A e^{gl}$. The total ASE intensity at a pump length l can be written as:

$$I(x) = I_s A \int_0^l e^{gx} + e^{g(l-x)-2\alpha(L-l)+gl} dx \tag{4.6}$$

$$\tag{4.7}$$

The normalized intensity used to fit gain and absorption coefficients for each wavelength becomes:

$$I_{norm} = \frac{I(l)}{I(L)} = \frac{e^{-2L\alpha}(-1+e^{gl})(e^{2L\alpha}+e^{l(g+2\alpha)})}{-1+e^{2gL}} \tag{4.8}$$

The method and has the advantage that both gain and absorption can be measured simultaneously. However, it requires a more accurate fitting. Here, the mirror is expected to be 100 % reflecting, which corresponds to the 2D calculations. However, scattering out of plane at the mirror can even be seen on the IR camera so there is a certain degree of loss. This leads to an overestimation of the absorption.

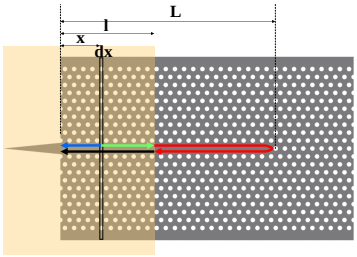

Figure 4.21: An illustration of the semi-closed waveguide, and the pumping scheme used to extract gain and absorption.

The measured spectra along with the fitted gain and absorption for a $300\mu m$ long 10 QW semi-closed waveguide are presented in Figure 4.22. The sample is the same as the one presented in Figure 4.20 (right) with a lattice constant of $380nm$, and band edge at $1566nm$.

The gain measurements shows a larger gain for higher pump powers, as expected. A gain above $100cm^{-1}$ is measured, which is realistic for a 10 QW device.

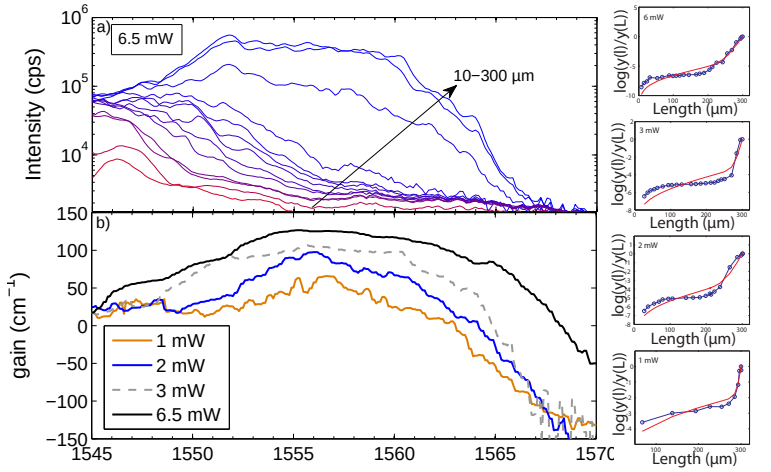

Figure 4.22: Gain extracted from ASE measurements acquired while pumping the different lengths of the 300μm long semi-closed 10 QW PhC waveguide. Data points beyond 1567nm are not trustworthy as they are beyond the band edge of the guided mode. The legend indicate the average pump powers of the RegA pump. To the right the experimental data along with the fits are presented for each pump power at the wavelength 1557nm.

4.5.2 Open Waveguide

To finalize the experimental study of slow light enhanced gain in PhC amplifiers we present gain measurement of three different 10QW PhC waveguides, each with a shift of the slow light region of 20nm in relation to each other. Using the RegA pump, which has proven to pump the 10 QW samples more efficiently than the 980 nm diode, gain measurements can be done also on the open waveguides (1 mm long with a taper on either end). Lets return to sample C, and waveguides next to sample C on the same chip. Eq. 4.4 is used for the fitting. Measured ASE accumulated at different pump lengths are presented to the left in Figure 4.23, all pumped at an average power of 6mW from the RegA. The corresponding gain curves for each waveguide are shown to the right. The fits fail to represent the measured data accurately at wavelengths much shorter than the gain maximum. The transparency levels are therefore not trustworthy. A clear slow light enhancement of the net gain is seen for all the different PhC designs and

the gain maximum shifts with PhC design. There is an variation of the spectral shape of the different gain curves. That could be assigned to different slow down factors. In difference to b) and d), the gain curve in f) does not show its maximum gain close to the band edge. This is likely caused by larger scattering loss which is more deteriorating for slow light, thus resulting in a smaller slow down factor. If the observed effects were to be explained by a pure filter effect (without slow light enhancement) the gain curves would be the same for all three devices, but with a sharp drop at the wavelength corresponding to the band edge of each device. However, a spectral shift of the gain maximum is observed as a result of a slow light enhancement.

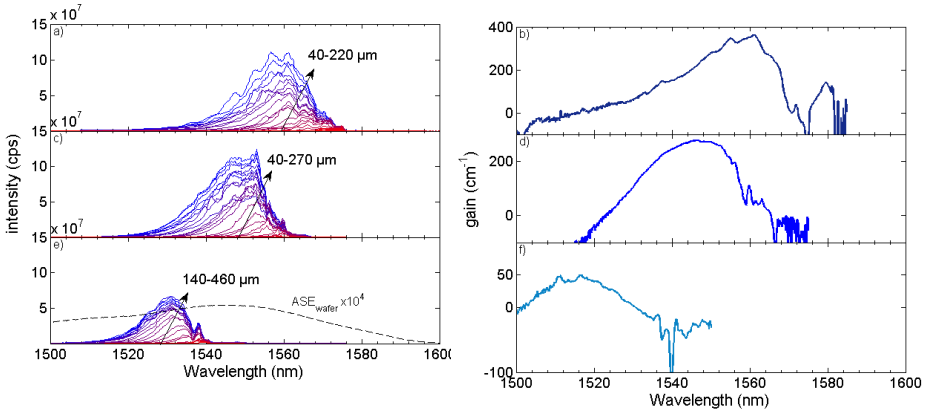

Figure 4.23: Gain measurements on three 10 QW PhC waveguides with different lattice constants. All are pumped with RegA at an average power of 6 mW. a-b) PhC waveguide with lattice constant $380nm$ (Sample C). c-d) PhC waveguide with lattice constant $375nm$. e-f)PhC waveguide with lattice constant $370nm$.

4.6 Random Lasing

All samples were not good candidates for systematic ASE measurements, such as comparing the ASE at different pump lengths to extract the gain. When 10 QW samples are pumped with the output from the RegA, a large gain is achieved by each pump pulse, as shown in the measurements. During the measurements lasing

modes were observed at discrete points along the waveguide in 10 QW samples. Such lasing modes are deteriorating for the gain measurements because they complicates the I_{norm} curves, making fitting more challenging. A drastic drop in intensity occurs when the pump is moved away from the lasing location, like an internal light-source which is suddenly switched off, see Figure 4.24. The images are taken with an IR camera attached to the imaging microscope in the set-up. A $1400nm$ longpass filter is placed in front of the camera, so it is only photoluminescence which is imaged, no stray pump light.

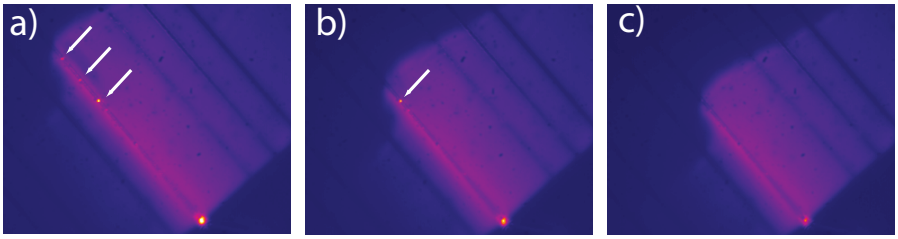

Figure 4.24: A photo series taken with an IR camera while pumping different lengths of a 10 QW sample with three distinct lasing modes in the PhC waveguide. The guided ASE intensity (seen as scattering out of plane at the taper tip at the bottom of each image) is drastically reduced as the lasing modes are shadowed.

Interference and random scattering can give rise to strong localization, also named Anderson localization [107]. There is no intentional introduced disorder in the samples, merely inherent disorder originating from the fabrication process. Surprisingly, light localization is stronger in a PhC waveguide with fabrication induced disorder than in a waveguide with an intentional degree of disorder [108]. A high gain might cause random localized modes to lase. Such localized lasing modes are also known to cause severe loss in transmission [109]. It is therefore of interest to characterize the localized modes further. The measurements on random lasing presented here were performed by Jin Liu, DTU Fotonik.

All the 10 QW samples which were tested show some degree of localization; not necessarily as strong and deteriorating for amplifier applications as the sample in Figure 4.24, but still present. Sample C has shown strong ASE and a gain of $380cm^{-1}$ (Figure 4.23), still it is believed that the localized modes are preventing the slow light gain to reach even higher levels. A SEM image of sample C is shown in Figure 4.25 a) and the measurement in c) show that within only $20\mu m$ several hotspots are found. This is consistent with the numerical simulation in b), where the mode profiles from a 2D finite-difference time-domain calculation are shown on the InGaAsP-air PhC structure with randomly varied hole positions (Gaussian distribution with standard deviations of $\delta = 1\%$). A strong localization due to slow light enhanced multiple scattering is shown for a fixed wavelength within the slow light regime. Figure 4.25 d) presents a study of random lasing at 5 different 10 QW waveguides, with the same pitch, but increasingly larger holes. Waveguide 2 corresponds to sample C, and the lasing occurs close to the band edge, which is located at $1580nm$ as known from previous measurements.

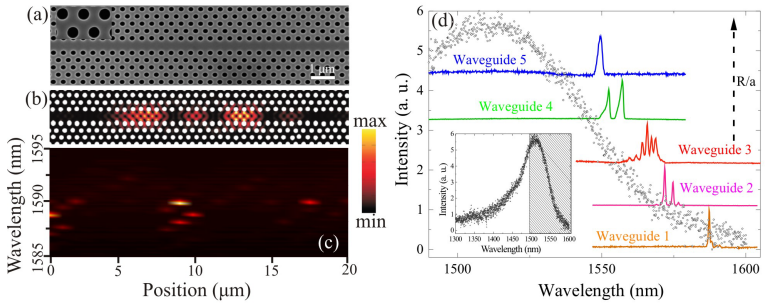

Figure 4.25: a) SEM image of Waveguide 2 (Sample C). No intentional disorder is introduced, only inherent fabrication disorder is present. b) Numerical finite-difference time-domain calculation of the localized modes in a random PhC waveguide ($\delta = 1\%$), for a fixed slow light wavelength. c) Experimentally measured localized modes using a micro-photoluminescence technique. The excitation/collecting objective is translated $20\mu m$ along the waveguide (sample C). d) Localized random lasing spectra for 5 waveguides with increasing hole diameter. The inset graph shows the full QW photluminescence spectra from the wafer, indicating the spectral range d). *Figure by courtesy of Jin Liu.*

The measurements[1] were done using a micro-photoluminescence setup where the sample is excited, and emission collected through the same objective, normal to the membrane. The excitation laser is the MIRA (Ti:Sapphire) emitting pulses with a wavelength centred at $800nm$, at a repetition rate of $78MHz$. Light is coupled through a fibre, broadening the pulses to a duration of about $1ps$. Sample emission is detected using the cooled InGaAs spectrograph.

Spatially localized modes with a distribution of emission wavelengths within the slow light region of each crystal design are observed. For waveguide 1, the lasing occurs at a wavelength with a large offset to the maximum wafer emission, which distinct it from diffusive random lasing which takes place at the maximum of the gain curve. Waveguide 1 and 5 show single mode lasing, while waveguide 2-4 show multi-mode lasing. This reflects the complexity of the lasing modes, characteristic for localized random lasing. In Figure 4.26 the properties of a multi-mode random laser are studied closer.

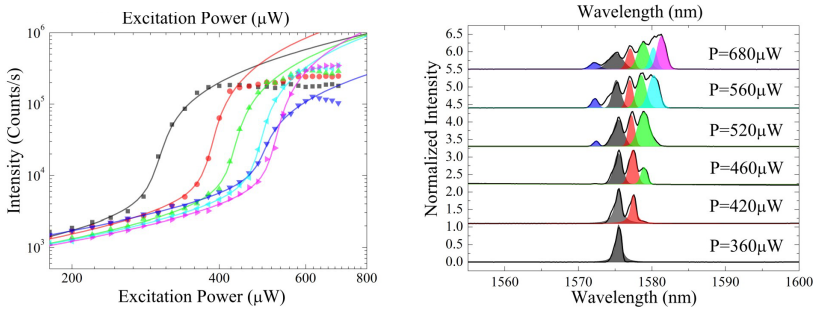

Figure 4.26: Left: Input-output curves for all the individual modes in a multiple mode random laser. The onset of a higher threshold mode at the same power as the previous saturates indicates mode competition. The experimental data is fitted with modified semiconductor laser rate equation. Right: Emission spectra at different powers. Each spectra is normalized and plotted with an offset for clarity. The modes starts to lase one by one. *Figure by courtesy of Jin Liu.*

Input-output curves for each individual mode is plotted in Figure 4.26(left), different lasing threshold for the various modes is observed. The data is extracted from the peak intensity of each

[1]Random lasing measurements are done by Ph.D. student Jin Liu, DTU Fotonk.

mode. As one mode saturates, another mode begins to lase, which is a strong indication of mode competition. The laser emission spectra in Figure 4.26 (right), show that a higher pump power brings an additional mode over threshold, one by one. Solid lines show fittings for each laser mode, the fits are based on semiconductor lase rate equations where Purcell enhancement is included for both the spontaneous and stimulated emission[1][110]. There are good agreements between experiment and theory apart from the region far above threshold. Saturation and mode competition effects are not included in the current model.

4.7 Summary

In this chapter slow light enhanced amplified spontaneous emission and slow light enhanced net gain have been experimentally observed. Heating is a limiting factor when optically pumping PhC membrane structures. However with pulsed excitation the issue can be circumvented and net gain of $38cm^{-1}$ and $380cm^{-1}$, for 1 QW and 10 QW structures respectively, have been measured. Measurements on PhC devices with different structural design show that the observed effects scale consistently with the attribution of the effect of slow light enhancement.

Lasing was observed in the 10 QW PhC waveguide, even in absence of intentional cavities. It is attributed to random lasing in localized modes.

[2]Theoretical fit by DTU student Troels Suhr, DTU Fotonik.

Chapter 5

Topology Optimized Waveguides and Lasers

5.1 Dispersion Engineering

A critical point in signal processing and optical communication is the requirement of a large bandwidth. Short pulses and high speed modulated signals have a very broad frequency spectrum. A constant high group index (i.e. low group velocity) over a sizeable bandwidth is desirable in order not to distort the signal. The complex confinement of light in PhC waveguides results in strong dispersion. As shown in this report, a single row of missing holes in a PhC membrane promotes a guided mode with large group index close to the band edge, where the dispersion relation has a parabolic form. Many reports are devoted to reduce the group velocity dispersion (GVD). One route is to compensate for the dispersion using coupled waveguides, as propsed by Baba et. *al* [111, 112]. Another route is to tailor the dispersion by changing the structural parameters of the PhC lattice, i.e. dispersion engineering.

For the best performance the following points should be fulfilled;

- **Transmission under the light line**
  Light is vertically confined in the membrane under the light line. If this condition is not fulfilled light will suffer severe out of plane losses.

- **Single mode**
  Inter coupling between modes should be avoided. If two modes are present at the same frequency, light could be lost to the other mode.

- **Even symmetry**
  Even modal field distribution improves in and out coupling to a gaussian mode.

- **Flat group index**
  A low GVD will cause less distortion of the signal. It also provides a uniform enhancement of optical amplification, or non-linear effects. It is desired to reach as high a group index as possible, while also maximizing the bandwidth.

Unfortunatley, the goals are conflicting. The slow down factor is intrinsically linked to the operation bandwidth; the higher the group index, the narrower the bandwidth [2]. It has been shown that the transmission spectrum of a PhC waveguide can be modified by changing the width of the waveguide [29]. By reducing the waveguide width to W0.7 (30% more narrow than a single row of missing holes, W1), a flat dispersion can be achieved [23]. The modification of waveguide width pushes both the index- and the gap-guided part of the mode up in frequency. Because the gap-guided mode moves faster, the anti-crossing point will shift to a lower k-vector in the band diagram, resulting in a flat band with low dispersion. Also double defect multi mode PhC waveguides, W2, has shown an improvement in second and third order dispersion compared to the W1 waveguide [60]. However, a single mode design with higher design freedom is desirable. A shift of the holes closest to the waveguide preserves the properties for the index guided wavelengths, while modifying the dispersion to a "U"-type group index curves [113]. One approach presented by Frandsen et al. is based on the knowledge that the modal field distributions differ between the index-guided part of the mode and the gap-guided mode with a low group velocity, see Figure 2.1. The field of the slow-light mode is concentrated in the two rows of holes closest to the waveguide, and is therefore more affected by changes of the structural parameters in that region. A flat plateau of the dispersion can be achieved by varying the hole diameter of the first and second rows of holes

[41]. Instead of changing the hole diameter the location of the holes can be shifted [101].

While the methods described above have resulted in high transmission waveguides with a desired flat dispersion region, many have been developed using trial and error approaches. In order to realize a PhC with any specified dispersion relation, especially designed for the application at hand, a more efficient design tool is needed. Topology optimization has proven to be a valuable tool when maximizing transmission through sharp bends and splitters in PhC structures [114]. Recently, it has been extended to find the best match between the fundamental mode dispersion and a preassigned dispersion relation [115]. The topology optimization tool is based on repeated finite element calculations and design updates, aiming to minimize the error between the actual and the target group velocity. The mode confinement is maximized, odd and multiple modes are avoided in the core region, and fabrication errors such as over- and under-etching are included to create a robust design [116].

5.1.1 Implementation of Topology Optimized Designs

Topology optimized designs[1]are implemented in passive InGaAsP PhC waveguides. An optimization limited to vary the radius and the location of circular holes only, provides a tool for systematic design of "classical" PhC waveguides. The prescribed group index, aiming for a group index of 40 over a bandwidth of $20nm$, and the dispersion relation for the optimized design in 2D is shown in Figure 5.1. Current state of the art topology optimization is done in two dimensions.

Before processing the device it is desirable to have a 3D simulation of the dispersion in order to choose a suitable lattice constant. A 3D calculation is done in MPB, using the unitcell parameters from the optimized design. Unfortunately there is a big difference between

[1]All topology optimization is done by Ph.D student Fengwen Wang at DTU Mekanik.

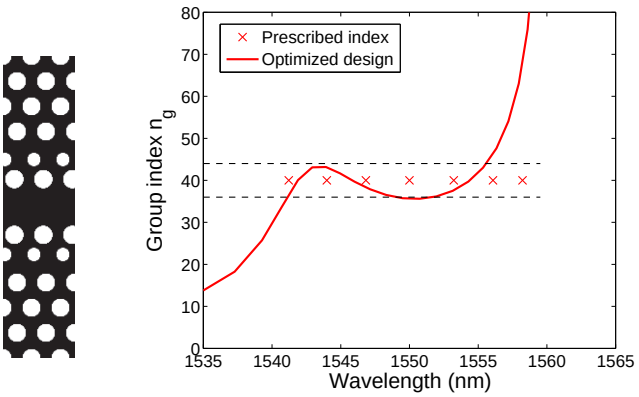

Figure 5.1: Topology optimization in two dimensions. The marked points illustrate the pre-described group index, dotted lines indicate the allowed deviation, and the red curve shows the dispersion of the optimized design. To the left an extended unitcell is shown *Figure by courtesy of Ph.D student Fengwen Wang at DTU.*

group index simulated in 2D and 3D. Due to higher confinement of light in an air-membrane, the group index is increased. The flat group index plateau is raised to $n_g = 70$, a higher group index also comes with a narrower bandwidth, see Figure 5.2. A lattice constant of $400nm$ tunes the slow light region into $1560 - 1580nm$ which is within the range of the tunable laser used for the characterization, and was therefore chosen for the fabricated device.

A SEM image of the fabricated sample is shown in Figure 5.3. The radius of the holes in the row closest to the waveguide are denoted r_1, the second row r_2 and the rest of the holes r. The structural parameters of the fabricated structure (topology optimized design) are: $r_1 = 0.302a$ ($r_1 = 0.317a$), $r_2 = 0.225a$ ($r_2 = 0.227a$) and $r = 0.315a$ ($r = 0.31a$). A good agreement between the design and fabricated structures are achieved, it is subject to uncertainty of the last digit in the SEM measurements. Also location shift of the holes corresponds to the design. The spatial position of the holes are in general easier to control than the exact hole radius, because the latter is affected by proximity effects during e-beam patterning.

Measurements[2]of the dispersion were done using the MZI setup explained in Section 4.1.2. Both the dispersion map and the group

[2]Measurements performed by Sylvain Combrie, Thales Research and Tech-

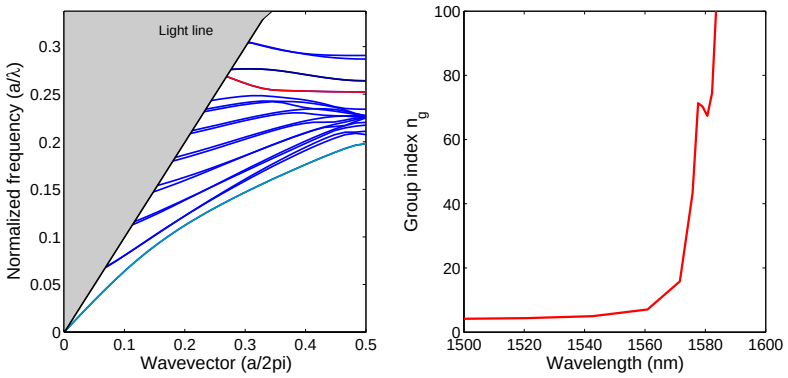

Figure 5.2: Dispersion diagram (left) and group index (right) from a 3D MPB calculation of the optimized design. A lattice constant of $400nm$ (membrane thickness $340nm$) brings the band edge to about $1580nm$.

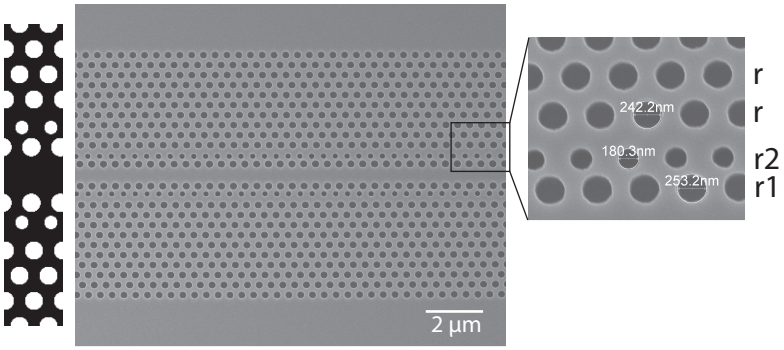

Figure 5.3: Left: a unitcell of the optimized design. Middle: SEM image of the fabricated structure. Right: a magnification showing the size of the holes r_1 at the bottom of the image, followed by r_2 and r. The location shift of the two rows closest to the waveguide can be seen.

index from the $1mm$ long waveguide are shown in Figure 5.4. The slow light region is spectrally located at the predicted wavelength, but the group index only reaches a value of 25. Thus, the predicted narrow plateau at $n_g = 70$ was not observed. According to the band diagram in Figure 5.2 (left), the fundamental mode does not overlap with any other mode at the frequencies in the slow light region. However, the measurement show propagation (zero dispersion) only $10nm$ away from the high group index region. It is not clear from the band diagram in Figure 5.2 which mode that might be, but is likely to be index guiding at the band gap edge. If irregular ge-

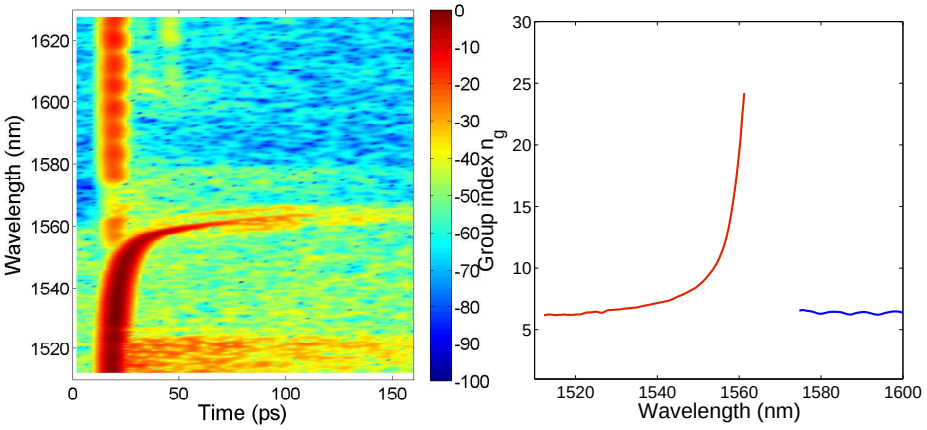

Figure 5.4: Left: time wavelength map of the topology optimized sample. Plotted on a log scale normalized to maximum transmission. Dark red is maximum transmission (0dB). Right: Extracted group index, using the sample length, 1 mm. The mode with zero dispersion at $1580 - 1600nm$ is plotted in a different colour because it is believed to be a different mode.

ometries are allowed in the optimization a much better performance than the "classical" design, including only holes, can be obtained. A group index of 80 over the wave vector region $0.35 < ka/2\pi < 0.45$ is theoretically obtained in the 2D topology optimization. Figure 5.5 shows the design and a SEM image of the fabricated sample. Reasonable agreement between the design and device is achieved. Some small features are missing, which can be explained by the dose (energy density with which the e-beam exposes the pattern)

nology, France.

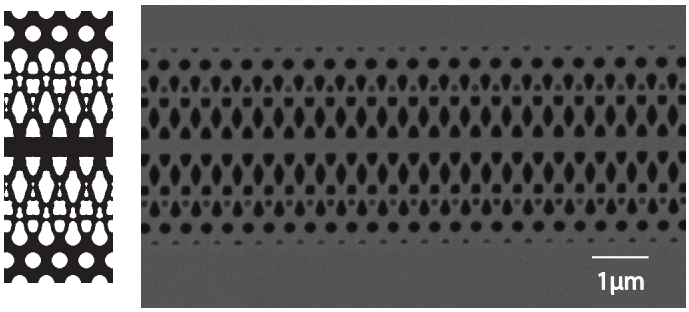

Figure 5.5: SEM image of the sample fabricated using the topology optimized design to the left.

being too low $220\mu C/cm^2$. There are issues with proximity effects during the patterning (e-beam) in the InGaAsP material which is not yet fully controlled. With a proper proximity correction the proper dose for each feature size can be used which would improve the result. Improved results could be achieved by proper proximity correction, the correction failed due to a faulty estimation of the backscattering of electrons on the complex epitaxial layout. The topology optimized design was therefore fabricated in silicon. Optical characterization showed that the guided mode was out of range of the tunable laser. Further investigation include experimental trials using a different lattice constant, and 3D calculations of the structure.

5.2 Photonic Crystal Micro Laser

Recently, much attention have been given to micro- and nano-lasers in PhCs, due to the wide possibilities of designing the quality factor (Q) and mode volume (V) in this type of material. High Q-factors are desirable as they imply long photon lifetimes and low thresholds. While large Q/V ratios can give high Purcell enhancement of the radiative decay, which can lead to faster and more effective devices. High-Q cavities have been realized [47, 45, 117, 118]. A superior confinement of light in a cavity included in a bandgap results in small mode volume (order of a cubic wavelength) and a high Q (around 10^6). This makes photonic crystal cavities an exciting route towards nano-scale lasers and single photonic sources. Lasers

with very small mode volume are not optimal for all applications. For an integrated laser on a photonic circuit, it is rather desired with stable single mode operation and higher output powers [119]. A promising candidate could be the PhC micro laser. One obvious disadvantage they hold compared to a ridge Fabry-Pérot laser is the pumping scheme. It is desirable to be able to electrically pump the PhC laser. It is challenging because of the current membrane configuration, but realistic within the near future. Electrical contacts on PhC membranes have been realized for light emitting diodes [120, 121], and nanocavity lasers [46, 72], although with relatively low quantum efficiency which leaves room for improvement. However, PhC lasers hold two important advantages; the ability to achieve high reflectivity at the cavity mirrors and operation in the slow light regime which means a longer propagation time in between the mirrors which results in increased photon lifetime, hence enhanced light-matter interaction [53, 27]. Also vertical cavity emitting lasers exhibit high reflectivity at the cavity mirrors owing to the Bragg reflection. The reflectivity of each mirror is determined by the number of mirror pairs included in the epitaxial structure. The design parameters in an in-plane configuration (PhC cavities) are more easily accessible. Integrated circuits based on PhC have been suggested [52], if realized, PhC micro cavities would be easily incorporated because they do not require cleaved facet mirrors, instead partly reflective mirrors can be introduced by inserting various number of holes into the PhC waveguide. Alternatively, laser light from a cavity with complete PhC mirrors can evanescently couple out to a nearby PhC waveguides. If a multi-mode laser is achieved with an equi-distance between the oscillating modes, the PhC microcavity holds great promise for a mode-locked laser. By the use of QDs in the gain region and QWs in the absorbing region of the cavity, an efficient compact passive mode-locked laser could be achieved [122]. The use of a slow light waveguide would increase the roundtrip time without compromising device size. In such a device dispersion engineering would play an important role, so that high repetition rates can be achieved while sustaining the short pulses.

There are only a few contributions in the literature where lasing explained by gain enhancement at low group velocities is shown

[49, 48]. One of these references [49], shows lasing operation at a low group velocity point above the light line, which leads to out of plane emission. Here, we present lasing in the guided fundamental mode below the light line. The low group velocity enhances the gain, as shown in measurements in Chapter 4, which is expected to reduce the lasing threshold.

Results on lasing in PhC micro cavities are presented in this Section. Lasing oscillation at the slow light wavelength of the mode is demonstrated. All laser structures are 3 QD PhC structures on 340 nm thick membranes. Two laser designs are presented which differ in PhC design and output mirror configuration.

5.2.1 Multimode Lasing

Measurements on a $50\mu m$ long cavity, which is a line defect terminated by PhC in one end and a cleaved facet in the other, are presented here. The lattice constant of the PhC is $390nm$ and the hole diameter in the fabricated laser is $132nm$. The dispersion properties of the device are modified by altering the size of the holes closest to the waveguide; $r_1 = 95nm$ and $r_2 = 156nm$ (r_1 and r_2 as indicated in Figure 5.3). This does not result in a flat dispersion plateau, but rather a fairly complicated dispersion as will be discussed.

The lasers are optically pumped with the output from the RegA, so $1ps$ long pulses at a wavelength of $800nm$ and repetition rate of $270kHz$. The power levels noted in the emission spectra, Figure 5.6 (left), denotes the average pump power over the full pump spot which has an area of about $10 \cdot 400\mu m$. The emission is detected on the cooled InGaAs spectrograph, with a resolution of $0.15nm$. Emission spectra at representative pump powers are shown in the figure. There are two spectral regions where laser oscillation occurs, around $1435nm$ and at $1595nm$. The integrated intensity as a function of average pump power is shown in Figure 5.6 (right). The emission show a threshold behaviour at an average pump power of $0.3mW$. A zoom in at low pump powers is seen in the inset. The increase in output power at increasing pump-powers below threshold show that it is not data points corresponding to the noise floor

of the detector. The spectral shape of the emission below threshold is seen in the top plot $0.12mW$to the left.

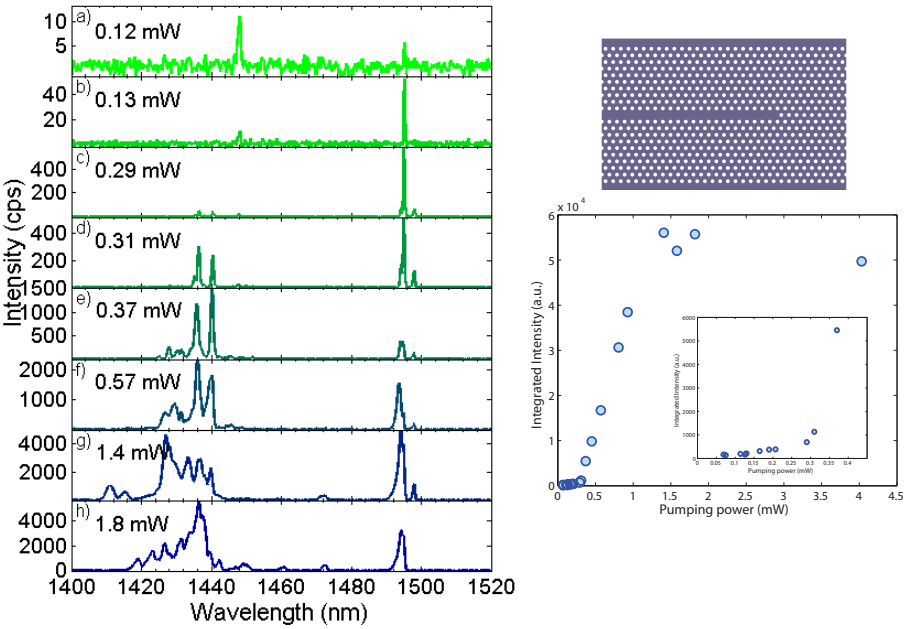

Figure 5.6: Left: Laser emission spectra from a $50\mu m$ long 3 QD cavity, pumped with RegA. The indicated power levels are average powers of the pulsed pump laser. The holes closest to the waveguide are of different size than the rest of the lattice, leading to emission at two wavelength regions. Right: the top figure illustrates the cavity configuration. The cleaved facet serves as a partly reflective mirror. The bottom figure show the measured Pin/Pout curve. The inset is a zoom-in at low pump powers.

A linewidth narrowing is observed at pump-powers up to 0.3mW , just above threshold. As the pump power increases the peak is broadened (compare emission at $0.31mW$ and $1.4mW$). Since the peak is not red shifted for higher pump powers, the broadening is not believed to be caused by heating. Rather, the large carrier density injected by the short, energetic pump pulses might introduce a deterministic chirp. A linewidth broadening of up to $2.5nm$ is observed in nanocavity PhC lasers, pumped with the same mode locked laser [86, 123]. Confirmation that nanocavity lasers are chirped under pulsed pumping is found in a recent recent report from Braive et al. [124] and a similar effect has shown to cause

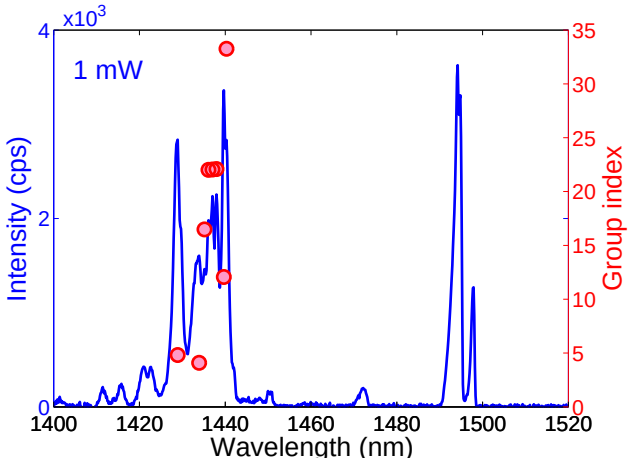

Figure 5.7: Laser emission at $1mW$ average pump power (blue) and the measured group index (red).

broadening in microdisk lasers [125].

The group index can be derived from the spacing between the peaks of the multimode emission. As shown in Section 4.1.1 the following relates the group index with the mode-spacing:

$$n_g = \lambda^2/(2L\Delta\lambda) \tag{5.1}$$

The laser emission at a pump power of $1mW$, and the measured group index is shown in Figure 5.7. Since there is mainly one lasing mode at $1495nm$ the group index could not be measured in that region. However the measured group index in the region around $1435nm$ show an increase from 4 to 34. The lasing occurs at a slow light region of the lasing mode.

In order to investigate the origin of the lasing a 3D MPB calculation of the dispersion diagram is calculated for the fabricated structure. The dispersion diagram (left) and the group indices for the fundamental (red in the middle) and the odd mode (blue to the right) are shown in Figure 5.8. The fundamental mode overlaps in frequency with the index band, which lead to severe loss into modes propagating in the slab. It is therefore not likely that the lasing oscillation occurs in that mode. The odd mode, indicated in blue, exhibit two slow light regions. At the band edge ($1500nm$) and at light-line cut-off. The two regions with slow light are separated by

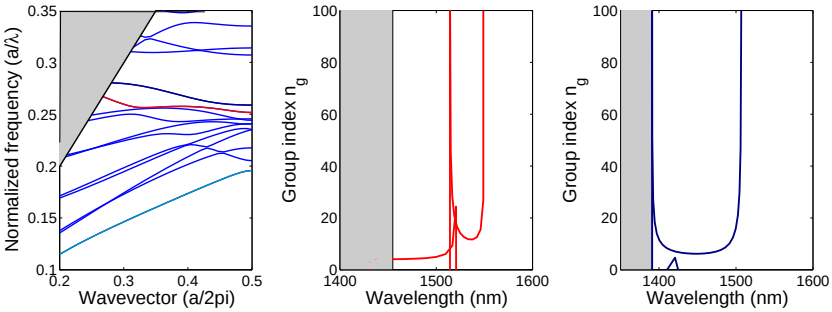

Figure 5.8: Left: Calculated dispersion diagram using the structural parameters from the fabricated device. The red line indicates the even mode and the dark blue mode in the gap indicates the odd guided mode. Middle: group index of the even mode. Right: group index of the odd mode. The group indices are plotted as a function of wavelength, derived from the normalized frequency of each mode, using the lattice constant $a = 390nm$. The gray regions in all the plots indicate the region above the light line. In that region light suffers severe out of plane loss.

$100nm$, which does not correspond to the measurements where a spacing of $60nm$ is observed. The odd mode has not been probed in previous experiments in this thesis due to its odd parity across the center of the waveguide, which lead to less efficient coupling. Despite a reduced light-matter interaction compared to an even mode, lasing oscillation can occur in that mode. An alternative explanation is that the lasing occurs at the band edge of the odd and the fundamental mode. The wavelength spacing between the two band edges are $40nm$, which does not match the measured spacing either. These initial results are promising and encourages further investigation of lasing in dispersion engineered laser cavities.

5.2.2 Single Mode Lasing

Laser cavities with a triangular lattice of equally sized holes were also fabricated and characterized. The design is identical to the amplifier design, the dispersion diagram can be seen in Figure 2.1, incorporating a $70\mu m$ long W1 micro cavity. A lattice constant of $400nm$ is used with a variation of hole size to shift the lasing wavelength of the band edge laser. The line defect which forms the cavity extends $70\mu m$ into the PhC from the out coupling mirror,

where it is blocked by holes. Thus, it is the same configuration as the semi-closed amplifier mirror. The output mirror is made to be only partly reflective by inserting four holes $5\mu m$ away from the out-coupling taper. Calculations of the reflection and transmission spectra of the structures based on 2D finite difference time domain simulations, indicates that 4 holes results in 97% reflectivity for wavelengths within the photonic bandgap. A schematic over the laser configuration is shown to the right in Figure 5.9. Laser emission at different pump powers (same pump scheme as in the previous Section) is shown in Figure 5.9 (left). The linewidth broadening, explained by a chirp caused by the energetic short excitation pulses, is observed here as well. A blueshift of the emission mode is seen for increasing pump powers, this may also be caused by pump induced refractive index changes. Since the peak is not red shifted for higher pump powers, the broadening is not believed to be caused by heating.

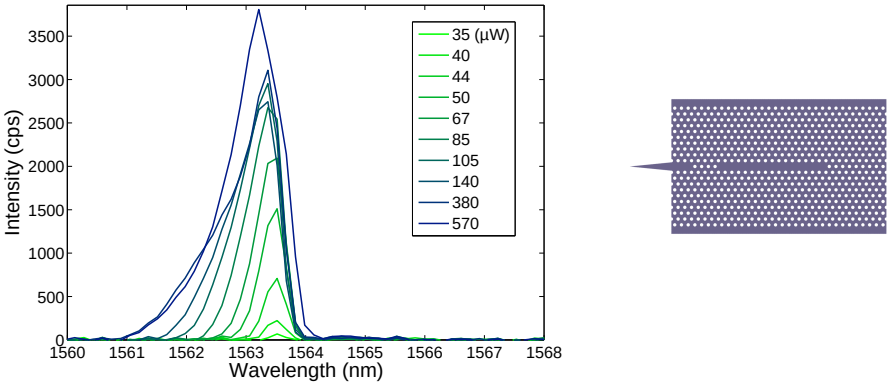

Figure 5.9: Left: emission spectra from a 70 μm long 3QD laser, pumped by the output from the RegA, the average power is noted in figure. Right: an illustration of the cavity configuration. Four-holes placed in the line defect close to the out-coupling taper forms a partly reflective mirror.

All the tested devices show lasing operation at a wavelength corresponding to the band edge of each design, as seen in Figure 5.10. Laser emission spectra from three PhC cavities are shown, all with a hole diameter shift of $5nm$ relative the previous. As theoretically predicted in Figure 2.3, such a shift in hole diameter corresponds to a wavelength shift of about $8nm$ in band edge position.

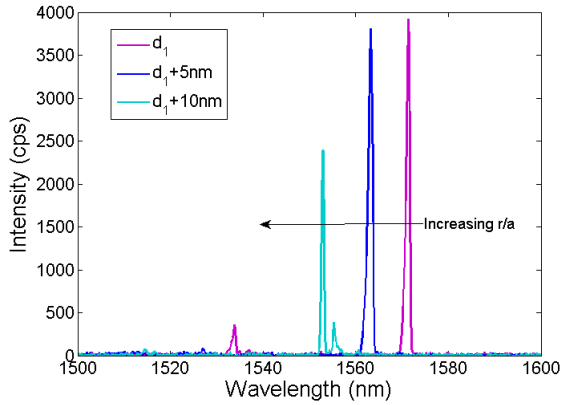

Figure 5.10: Samples: 70 μm long 3QD lasers of different designs. Pump: RegA, average power 6 mW. Left: Laser emission spectra from three 70μm long 3QD lasers with increasing hole size. All with four-hole output mirror and a out-coupling taper. The cavities are optically pumped with the output from the RegA, at an average power of 1mW.

5.3 Summary

Topology optimized PhC waveguides, aiming to achieve a constant group index over a broad range of frequencies have been fabricated. The fabricated structure with a "classic" design, consisting of holes only, is structurally well matched to the design. A light slow down is observed at the predicted wavelength, however it does not reach the predicted magnitude.

QD micro laser cavities of different configurations and photonic crystal design have been fabricated, and lasing operation is demonstrated. The lasing wavelength shifts depending on the PhC design, and the lasing is assigned to occur at the cavity mode band edge. A partly reflective mirror consisting of a number of holes in front of an out-coupling taper allows for optimization of the reflectivity, here 4 holes was used. Lasing in a PhC cavity with a complex dispersion relation was demonstrated. For future devices it is desired to use dispersion engineered designs for the micro-cavities, such that lasing occurs away from the band edge at a pre-assigned slow down factor. Operation at the band edge involves large scattering losses [57], and recently it was shown in reference [126], that a large material gain degrades the slow down properties compared with a corresponding

passive device, and thereby limits the slow light enhancement of the effective gain. The impact of gain is less detrimental where the enhancement factor is kept at a value of about $60-100$, rather than at the band edge where the slow down factor approaches infinity theoretically.

Chapter 6

Ultrafast Dynamics in Quantum Dots

When engineering components which aim to operate in the terabit per second regime it is important to fully understand the ultra fast gain dynamics of the device. Such studies have not yet been performed on PhC amplifiers, but are of central importance for future experiments. In order to distinguish the influence of light slow down from the dynamics of the gain material itself, it is desirable to have measurements of the gain material without PhC for comparison. In this Chapter pump-probe measurements on the GaAs capped InAs QDs used in both PhC amplifiers and PhC lasers (Chapter 4 and 5) are presented.

As opposed to the former experiments in this thesis, these measurement were based on a single mode ridge waveguide. The active region was sandwiched in a PIN configuration allowing for electrical carrier injection. The ASE from the electrically biased $(10 - 180mA)$ sample, measured with an OSA, is shown in Figure 6.1 (left). The spectra show indications of more than one transition being involved. The peak near 1400 increase with almost no saturation, while a lower energy state, around $1580nm$ saturates. If there were only one exciton transition involved, the whole spectrum would increase equally for all wavelengths. Another feature which is observed in the measured ASE spectrum is a modulation with clear dips an peaks at different wavelengths. One possible cause of

the dips in the spectra could be the phonon bottleneck, described theoretically in [127] and observed experimentally in [128, 129]. In QDs with discrete energy levels, carrier relaxation can be reduced at energy transitions with inefficient phonon scattering [130]. Efficient relaxation can take place only when the electron level spacing match the LO-phonon energy, or within a few meV to be assisted by LA-phonons. The LO-phonon energy in InGaAsP is about 37 meV [131] ($\lambda = 60nm$) which roughly correspond to the spacing between the peaks in the ASE emission spectrum. If the modulation is explained by the phonon bottleneck, the characteristic gain recovery times at a peak relative a dip should differ. However, as shown in Section 6.2, such wavelength dependency of the gain recovery times was not observed which challenges the hypothesis.

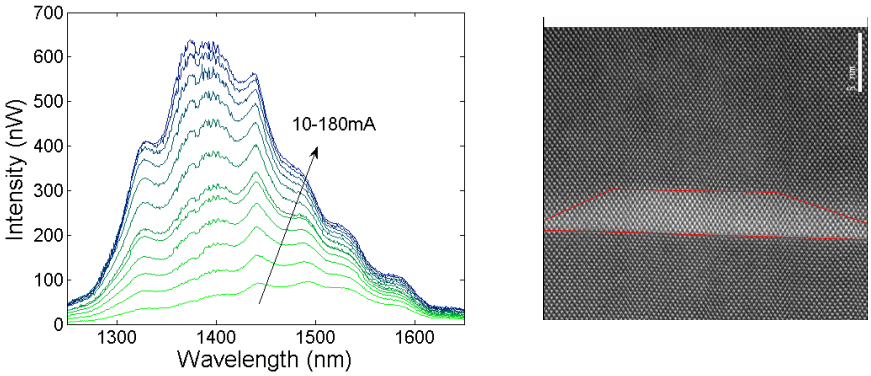

Figure 6.1: Left: ASE spectrum from an electrically biased 5QD SOA at currents ranging from 10 to 180 mA. (RBW=2nm) Right: HAADF STEM image of a GaAs capped InAs QD followed by InGaAsP. The InAs rich dot appear bright in the image, red lines are guides to the eyes. *Figure by courtesy of Shima Kadkhodazadeh, DTU Fotonik.*

A high-angle annular dark-field (HAADF) scanning transmission electron microscopy (STEM) image of a GaAs capped InAs QD is shown in Figure 6.1 (right). The InAs rich dot appear bright in the image. The average measured height and diameter of the QDs were 2.6 nm and 31.9 nm, respectively. The use of a GaAs capping layer results in a flat top dot with reduced height compared to a dot capped with InGaAsP only [38]. The ASE modulation is most likely attributed to sub-ensembles of QDs which differ in height by one InAs monolayer. Dots with a discrete number of monolayers in height lead to well defined transitions. The fact that the effect

is clearly seen in the ASE spectra demonstrates that there is a low statistical deviation around the mean transition energy in each sub-assembly [132]. This multimodal nature of the QDs have been observed by others [132], and the wavelength spacing between the peaks in Figure 6.1 (left) are on the same order as that measured on InAs/GaAs dots [133].

6.1 Experimental Details

6.1.1 Sample

A $2\mu m$ wide, $500\mu m$ long ridge SOA with electrical contacts is used in the pump-probe measurements [1]. The end facets are cleaved at the Brewster angle and to further reduce back reflections the end facets are anti-reflection coated. The waveguide material is InP, and the five layers of GaAs capped InAs dots are surrounded by InGaAsP barriers[2]. There is a large variation in dot size, resulting in an inhomogeneously broadened photoluminescence spectra from the unprocessed wafer with a full width half maximum of $140nm$ centred at $1620nm$. The sample is mounted on a Peltier cooled copper block to keep a stable temperature of $20°C$ during the pump-probe measurements.

6.1.2 Pump-probe setup

The Mira mode-locked laser (Coherent Mira 900, Ti:Sapphire) and the RegA (Coherent regenerative amplifier with Ti:Sapphire as gain medium) have been introduced in Chapter 4, where the amplified pulses from the RegA are used to optically pump the PhC waveguides. Here, the output from the RegA is injected into an optical parametric amplifier (Coherent OPA) for wavelength tuning.

The ultra fast relaxation which occur only picoseconds after a pump pulse has propagated through a SOA can be measured by a probe

[1] Sample processed by Ph.D. student Irina Kulkova at DTU Fotonik.

[2] Epitaxial growth by Elizaveta Semenova and Kresten Yvind at DTU Fotonik.

pulse. The pulse duration is $180fs$, and this sets the temporal resolution of the measurement. Each pulse in the idler beam from the OPA is split up into three paths using acousto optic modulators (AOMs); a pump modulated at 40 MHz, a probe modulated at 80 MHz and a reference beam. This requires two AOMs as indicated in the set-up schematic in Figure 6.2. The figure is slightly misleading, it is important that light propagates the same optical path length in each arm. This so that the pump and the probe arrive simultaneously (or at a short delay) at the sample. In order to detect the probe selectively a heterodyne detection technique is used [134], the pump and the probe can then be of same wavelength and polarization and still be distinguishable. The probe can be measured by achieving a temporal and spatial overlap with the reference, and detect the lowest beat frequency between the two on a balanced detector. The beat signal is sent to a lock-in amplifier. The measurement technique allows measurements of both amplitude (gain) and phase (refractive index), here we focus on the gain measurements.

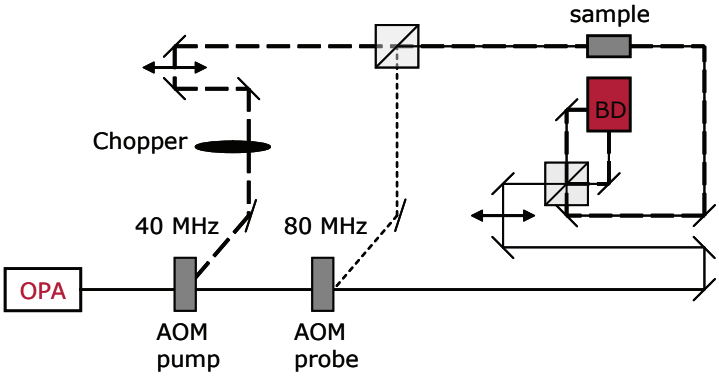

Figure 6.2: A schematic of the pump-probe set-up. The figure is slightly misleading, the optical path lengths for the pump, probe and reference are all of equal length.

An illustration of the pump-probe principle is shown in Figure 6.3. The bottom curve show a typical response function where the dip in probe transmission is seen at zero delay. Zero delay means that the pump and the probe enters the waveguide simultaneously, as illustrated in the top figure. The pump depletes the carrier distribution leading to a gain saturation and a decrease in probe transmission.

The probe transmission is reduced at all time-delays until enough time has passed so the material is fully recovered due to refilling of carriers. In the absorption regime an increase in probe transmission is expected due to optical excitation of carriers by the pump. The delay between the pump and the probe is increased by decreasing the optical path length of the pump. This is controlled accurately in small steps using a motorized delay stage.

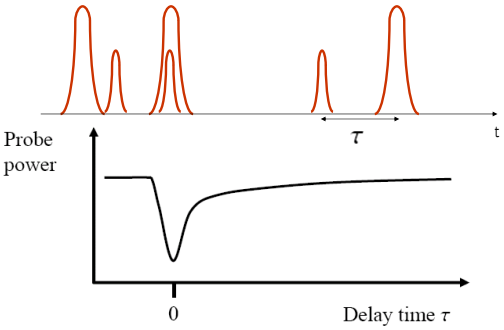

Figure 6.3: A schematic of the delay between the pump (higher amplitude) and the probe (lower amplitude) and the corresponding pump-probe measurement in the gain regime.

At each delay, the probe transmission with and without the pump present, is measured. The pump signal is chopped at $15Hz$ and the lock-in amplifier integrates over 1 ms. This results in tolerable signal to noise while allowing to detect a fast shift between the "on" and "off" state of the pump. When the pump is chopped, and all beams are aligned in time and space, the modulation at the chopper frequency is clearly visible on the lock-in signal. If the probe arrives up to $100ps$ (time for full gain recovery) after the pump, the modulation is seen. The pump delay stage can be adjusted to find the maximum modulation of the signal, to find the complete overlap between the pump and the probe (zero delay).

The differential probe transmission $\Delta T/T$ is extracted from the measured lock-in signal according to:

$$\frac{\Delta T}{T} = \frac{T_w - T_{wo}}{T_{wo}} = \frac{V_w^2 - V_{wo}^2}{V_{wo}^2} \tag{6.1}$$

where V is the measured lock-in signal, the indices w and wo indicate with and without the pump pulse present. The heterodyne cross correlation technique detects changes in the electric field amplitude, resulting in the squared dependence of the measured voltage signal.

6.1.3 Response Function

A response function approach can be used to describe every system where there is a linear relation between input and output. Here the response function is denoted with h and the change in probe transmission through a SOA can be written as [135, 136]:

$$\frac{\Delta T(\tau)}{T} = \int_{-\infty}^{\infty} h(\tau - t)dt \int_{-\infty}^{\infty} S(t)S(t - t')dt' \tag{6.2}$$

The impulse function $S(t)$ describes the photon flux, the probe pulse is assumed to be a weak replica of the pump. The response function,h, includes several amplitudes and time constants, representing different physical processes:

$$h(t) = A_{TPA}\delta(t) + A_1 e^{-t/\tau_1} + A_2 e^{-t/\tau_2} + A_3 e^{-t/\tau_N} \tag{6.3}$$

The pump pulse cause carrier depletion from the considered energy state, which results in reduced gain. This is then followed by subsequent refilling by carrier relaxation. Instantaneously as the pump and the probe overlap at probe time delay equals zero, two photon absorption (TPA) occur, the time constant for TPA is therefore very short and is described by a Dirac's δ-function. There are two characteristic gain recovery times which can be measured in the current set-up. The fastest out of the two, (τ_2), describes the relaxation of carriers from discrete energy states within the dot. The slower time constant, (τ_1), describes the relaxation from the wetting layer into the dot. There is a third time constant (τ_N) which is related to the total carrier density. This could not be accurately measured because it requires longer delay scans than what is possible in the current set-up. It is on the order of $100ps$ [137], and after that time the gain material is totally recovered. We set $e^{t/\tau_N} = 1$, and the associated amplitude A_3 is the offset to the zero-axis at the

longest measured delay. Expressions for the amplitudes,A_{TPA}, A_1 and A_2, can be found in reference [138].

6.2 Experimental Results

Pump-probe measurements were carried out at six different wavelengths, chosen to overlap with dips and peaks in the ASE spectrum while covering the full range from absorption to gain regime. At each wavelength, a variation of bias currents were used. The bias dependency at the wavelength $1440nm$ are presented in the end of this section. The OPA laser spectra for each wavelength along with the ASE (gray) spectrum are shown in Figure 6.4.

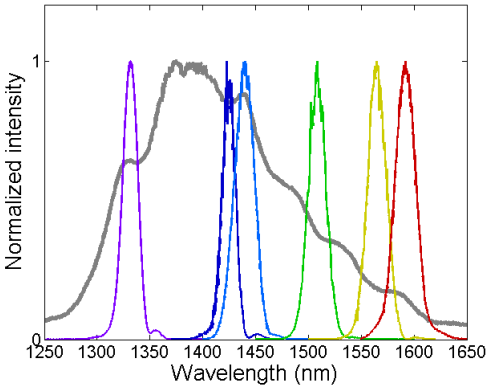

Figure 6.4: ASE spectra (gray) and normalized laser emission spectra at each wavelength at which pump probe measurements were carried out. The wavelengths $1423, 1440nm$ and $1565, 1590nm$ correspond to a dip and a peak respectively. The chosen wavelengths covers a range of $260nm$.

Figure 6.5 shows pump-probe measurements at the chosen wavelengths. The pulse energy for the pump and probe were set at $0.9pJ$ and $0.2pJ$ respectively, and the sample is biased at a current of $100mA$. All measurements were carried out for a probe delay ranging from $-1.5ps$ to $10ps$. Largest gain is seen for the wavelength $1440nm$, where a large decrease in probe transmission is seen. Going to shorter wavelengths the pump photon energy is so high so that it corresponds to the absorption regime and carriers are excited, that leads to an increase in probe transmission.

For long wavelengths (low photon energies) mainly instantaneous processes at zero time delay takes place. Because the photon energy corresponds to an energy close to the band edge it is barely influenced by total carrier density variations. The material then recovers owing mainly to the fast component. This is also confirmed by the extracted amplitudes in Figure 6.6 (right). Both amplitudes which represent the slow contributions (A_1 and A_3) are close to zero for long wavelengths. A_3 provides information about how close the material is to full recovery at $10ps$ delay. It is positive in absorption, negative in the gain regime and zero at transparency. For all wavelengths in the gain regime it is measured to be close to zero, indicating that the total gain recovery is dominated by fast intra-dot and wetting layer-dot relaxation. All amplitudes are normalized with $\sqrt{A_{TPA}^2 + A_1^2 + A_2^2 + A_3^2}$.

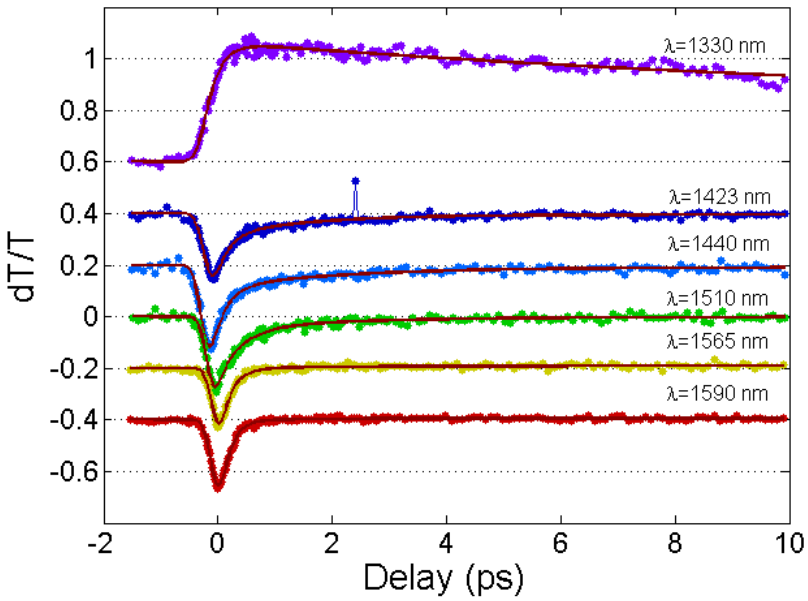

Figure 6.5: Differential transmission as a function of probe delay. The different colours indicate different pump-probe wavelength and each curve is offset 0.2 for clarity. Applied current: $100mA$. Solid red lines represents the fitted response function to each measurement.

A longer recovery time for the slow component, τ_1 is seen for absorption compared to the other wavelengths in gain regime in Figure 6.6 (left). An increase of τ_1 is also observed in reference [139] in

the absorption regime. The effect can be explained by the following reasoning: for wavelengths in the gain regime carriers are depleted from the energy state considered. The vacancies are filled by carriers from the higher energy levels in the dot or from the wetting layer. For wavelengths in the absorption regime, the pump excites carriers to a high energy level within the dot. In the absence of available states at lower energy levels, the injected carriers need to escape to higher laying energy states in the wetting layer. Such process can be phonon-mediated or carrier-carrier mediated (scattering), which is slower than carrier capture. Following the reasoning, a short, highly absorbing wavelength such as $1330nm$, results in large A_1 and A_3, as shown in Figure 6.6 (right). Besides from the deviation in τ_1 between absorption and gain regime, the slow and fast time constants τ_1 and τ_2 does not vary much as a function of wavelength. That reflects the large inhomogeneous broadening in the sample. The relaxation time constants are on the order of $\tau_1 \sim 2ps$ and $\tau_2 \sim 0.2ps$, in good agreement with earlier reports on relaxation times in QDs emitting at $1550nm$ [139, 140, 141, 142]. The fast time constant is close to the resolution, defined by the pulse duration ($0.18ps$). Hence, there is an uncertainty in the amplitudes A_{TPA} and A_2. It is also noted that the carrier dynamics does not differ for dots with different number of monolayers, represented by wavelengths at the different peaks in the ASE spectrum.

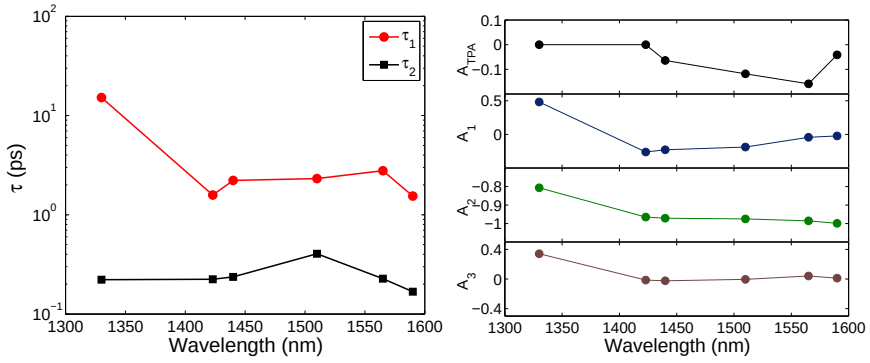

Figure 6.6: Left: Characteristic gain recovery times for QD SOA as a function of wavelength. Slow component (τ_1) shown in red and fast component (τ_2) shown in black. Right: normalized amplitudes coefficients of the response function in Eq. 6.3. The applied current is fixed at $100mA$.

Figure 6.7 presents the temporal gain dynamics as a function of

injected current at a fixed pump-probe wavelength of $\lambda = 1440nm$. The indicated current levels are normalized with the transparency current, I_{tr}. The transparency current is measured at a constant delay of $5ps$ between the probe and the pump. At that delay the ultrafast carrier dynamics can be discarded and the differential transmission is negative in the gain regime, positive in the absorbing regime while vanishing at transparency point. At the transparency the TPA will take place a zero time delay, but since there is no net stimulated emission there is no change in carrier density. The measured transparency current is $I_{tr} = 60mA$ is valid for the material gain, corresponding to the bias current where the stimulated emission rate equals the absorption rate.

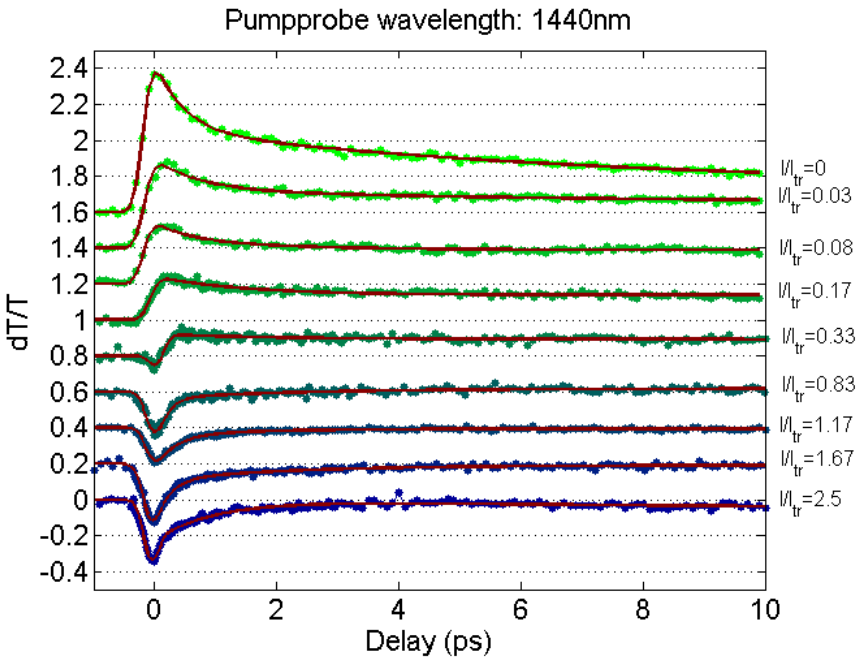

Figure 6.7: Differential transmission at $\lambda = 1440nm$ as a function of injected current. The different colours green to blue indicate increasing current, as indicated relative the transparency current ($I_{tr} = 60mA$) in the border . Each curve is offset 0.2 for clarity. Solid red lines represents the fitted response function to each measurement.

It is clear that with increasing current injection, the material changes from being in to absorbing regime to the gain regime. The measured data is well represented by the bi-exponential fits, represented

by red solid lines. The fit parameters are presented in Figure 6.8. Both the fast and the slow timeconstants (Figure 6.8 (left)) seem almost unaffected by injected current. Only at zero bias a large increase in τ_1 can be seen, due to the longer relaxation time for carrier escape than for carrier capture. For comparison, the timconstants derived from measurements at $1423nm$, corresponding to a dip in the ASE emission spectrum, are shown in the figure as well. If the modulation in the ASE spectra was explained by the phonon bottleneck, the time-constants for a wavelength corresponding to a dip ($1423nm$) and a peak ($1440nm$) would differ. That is not observed in the measurements.

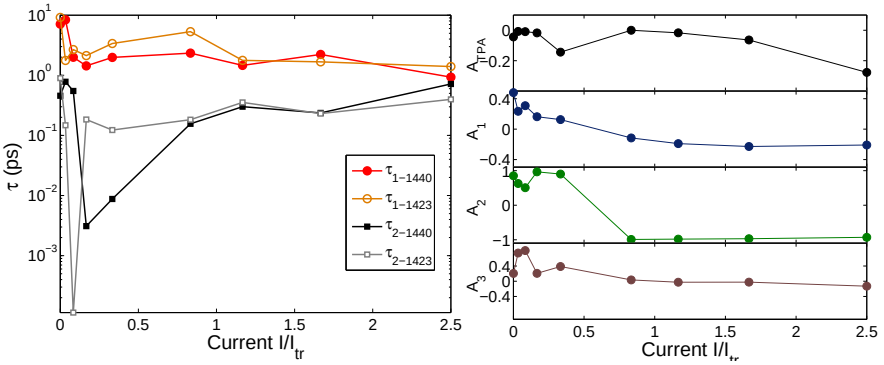

Figure 6.8: Left: Characteristic gain recovery times for QD SOA as a function of injection current. Slow component (τ_1) shown in red and fast component (τ_2) shown in black. Derived time constants for both $1423nm$ and $1440nm$ are shown for comparison. Right: normalized amplitudes coefficients (at $\lambda = 1440nm$) of the response function in Eq. 6.3.

6.3 Summary

A modulation is observed in the measured ASE from a SOA with five layers of quantum dots. The modulation is explained by emission from sub-ensembles of dots with different number of monolayers. Pump-probe measurements of the sample show that the carrier dynamics from dots of different height does not differ. Two characteristic gain recovery times are measured to be $\tau_1 \sim 2ps$ and $\tau_2 \sim 0.2ps$, consistent with previous reported values for dots with an emission wavelength of $1550nm$. The recovery times are almost

constant over a large range of wavelengths, and applied currents. Only when in the absorption regime a increase in τ_1 ($\sim 10ps$) is observed, which is expected due to the optical excitation of carriers.

Chapter 7

Conclusion and outlook

Photonic Crystal Amplifiers

Photonic crystal slab waveguides, incorporating active layers have been fabricated, and the possibility of enhancing gain by using slow light effects have been investigated. Structures with a single quantum well, 10 quantum wells and three layers of quantum dots were fabricated, all emitting at $1550nm$. All waveguides have taper structures at input and output to minimize insertion loss and suppress residual reflection. Measured amplified spontaneous emission spectra were observed to be enhanced close to the band edge, where light is slowed down due to photonic crystal dispersion. The amplified spontaneous emission from photonic crystal waveguides of different designs were characterized, showing that the enhanced region consistently shifts to overlap with the slow light region of each design. The modal gain was derived from systematic measurements of the amplified spontaneous emission at different excitation lengths. A single quantum well sample show a modal gain of $38cm^{-1}$ in the enhanced region, while a gain of $370cm^{-1}$ was measured for 10 quantum well samples. The spectral profile of the modal gain envelope along with the high absolute values are explained by enhancement of net gain by slow light.

The slow light enhancement of gain was measured also investigated by transmission measurements. Due to severe heating when op-

tically pumping the structure in continuous wave mode, the measurements were done using short excitation pulses. Lock-in measurements at the repetition rate of the pump laser show that the amplification is clearly wavelength dependent with more than 10 times greater differential transmission in the slow light regime relative fast light regime.

Lasing was observed even in absence on intentional cavities. It is attributed to random lasing in Anderson localized modes.

outlook

Heating of the samples turned out to be a more critical point than first anticipated. For future devices the thermal management needs to be improved. Ongoing experiments on patterned epitaxial growth are well under way at DTU Fotonik and will be implemented in photonic crystal amplifiers soon. Such buried heterostructure is expected to reduce heating significantly. Alternative designs where the membrane is encapsulated in BCB are also being considered. That would improve the thermal conductivity compared to the current air-membrane configurationm and more importantly, it would allow for passive access waveguides.

In this work, a taper was used to improve coupling and reduce reflections at the facets. However, the taper was not specifically optimized for coupling of a slow light mode. The field distribution of a slow light mode is very different from an incoming gaussian mode, leading to a weak coupling. A slow light coupler will be implemented for future designs. Further efforts will be made to realize topology optimized designs.

Photonic Crystal Micro Lasers

Photonic crystal micro lasers were fabricated and its optical properties were investigated. The device design was identical to the photonic crystal amplifiers, with an addition of cavity mirrors. The demonstration of laser oscillation confirms that net gain is achieved in the 3QD photonic crystal devices.

Lasing was observed in cavities which were 50 - and 70μm long, with two different output mirror configurations; a flat cleave and a partly reflective photonic crystal mirror consisting of four holes. In a crystal with uniform hole sizes, lasing occurs at the band edge of the defect mode. Measurements on 70μm long lasers with different hole size show that the shift in emission wavelength correspond to the shift in band edge position. In a dispersion engineered photonic crystal cavity, lasing was observed at two spectral regions separated by $> 60nm$.

Outlook

The effect of slow light enhanced gain in photonic crystal micro cavities will be further investigated. The lasing threshold is expected to be greatly reduced for low group velocities [53], why an experimental study of the dependency will be initiated. Attention will be given to achieve lasing away from the band edge in a dispersion engineered device. Operation at the band edge has several disadvantages; light suffers high losses due to scattering [57], a large material gain is expected to degrade the slow down properties at the band edge [126], and the slow down factor can not be precisely controlled.

Photonic crystal amplifiers can also become and interesting platform for mode-locked lasers. Although several challenges needs to be overcome before the realization of such a device, efforts will be made in that direction. Advances in selective growth will enable incorporation of gain and absorber regions and further work will focus on multi-mode photonic crystal micro lasers.

Pump-probe Measurements on Quantum Dot SOA

The gain dynamics of the quantum dot material used in the amplifiers and lasers were measured. The measurements were done on a ridge single mode SOA with five layers of quantum dots. Several dips and peaks were observed in the amplified spontaneous emission spectrum from the device. The modulation is related to sub assemblies of InAs quantum dots which differ in height by one

InAs monolayer. Pump-probe measurements were carried out at six different wavelengths with a fixed applied current of $100mA$. Two characteristic times of $\tau_1 \sim 2ps$ and $\tau_2 \sim 0.2ps$ were extracted using a response function fitted to the measurements. It was shown that the carrier dynamics does not depend on the number of monolayers in the quantum dots.

Pump-probe measurements at a fixed wavelength ($1440nm$) with various applied currents were also presented. The gain recovery was measured in both the gain regime and absorbing regime.

Outlook

To date there are no measurements on pulse propagation or gain dynamics in active photonic crystal waveguides. Future measurements will focus on characterizing photonic crystal amplifiers. Pump-probe measurements at wavelengths corresponding to the slow relative the fast regime of the photonic crystal can provide interesting information about the carrier dynamics. For these measurements a short photonic crystal amplifier, which can be measured in transmission is required (i.e. with access waveguides). If the device is too long, it will not be possible to measure in the absorption regime. The highly dispersive nature of photonic crystal devices requires a longer pulse duration of the pump to achieve a spectrally narrow pulse. Dispersion engineered devices with a constant group index over a broad range of wavelengths would be advantageous for these measurements.

Bibliography

[1] E. Desurvire, "Capacity demand and technology challenges for lightwave systems in the next two decades," *Journal of lightwave technology*, vol. 24, no. 12, pp. 4697–4710, 2006.

[2] T. Baba, "Remember the light," *Nature*, vol. 1, no. 1, pp. 11–12, 2007.

[3] L. Rayleigh, "On the maintenance of vibrations by forces of double frequency, and on the propagation of waves through a medium endowed with a periodic structure," *Philosophical Magazine*, vol. 24, pp. 145–159, 1887.

[4] R. Wood, "On a Remarkable Case of Uneven Distribution of Light in a Diffraction Grating Spectrum," *Philos. Mag.*, vol. 4, pp. 396–402, 1902.

[5] W. Bragg, "The Diffraction of Short Electromagnetic Waves by a Crystal," *Proceedings of the Cambridge Philosophical Society*, vol. 17, pp. 43–57, 1913.

[6] K. Ohtaka, "Energy band of photons and low-energy photon diffraction," *Physical Review B*, vol. 19, no. 10, pp. 5057–5067, 1979.

[7] E. Yablonovitch, "Inhibited spontaneous emission in solid-state physics and electronics.," May 1987.

[8] S. John, "Strong localization of photons in certain disordered dielectric superlattices.," June 1987.

[9] J. V. Sanders, "Diffraction of light by opals," *Acta Crystallographica Section A*, vol. 24, pp. 427–434, July 1968.

[10] J. Zi, X. Yu, Y. Li, X. Hu, C. Xu, X. Wang, X. Liu, and R. Fu, "Coloration strategies in peacock feathers.," *Proceedings of the National Academy of Sciences of the United States of America*, vol. 100, pp. 12576–8, Oct. 2003.

[11] L. Biró, Z. Bálint, K. Kertész, Z. Vértesy, G. Márk, Z. Horváth, J. Balázs, D. Méhn, I. Kiricsi, V. Lousse, and J.-P. Vigneron, "Role of photonic-crystal-type structures in the thermal regulation of a Lycaenid butterfly sister species pair," *Physical Review E*, vol. 67, pp. 1–7, Feb. 2003.

[12] E. R. Brown, C. D. Parker, and E. Yablonovitch, "Radiation properties of a planar antenna on a photonic crystal substrate," *Journal of optical society of America B*, vol. 10, no. 2, pp. 404–407, 1993.

[13] T. F. Krauss, R. M. De La Rue, and S. Brand, "Two-dimensional photonic-bandgap structures operating at near infrared wavelengths," *Nature*, vol. 383, pp. 699–702, 1996.

[14] R. Meade, K. Brommer, A. Rappe, and J. D. Joannopoulos, "Existence of a photonic band gap in two dimensions," *Applied Physics Letters*, vol. 61, pp. 495–497, 1992.

[15] K. M. Ho, C. T. Chan, and C. M. Soukoulis, "Existence of a photonic gap in periodic dielectric structures," *Physical Review Letters*, vol. 65, no. 25, pp. 3152–5, 1990.

[16] T. Lund-Hansen, S. Stobbe, B. Julsgaard, H. Nielsen, T. Sünner, M. Kamp, A. Forchel, and P. Lodahl, "Experimental realization of highly efficient broadband coupling of single quantum dots to a photonic crystal waveguide," *Physical review letters*, vol. 101, no. 11, pp. 1–4, 2008.

[17] K. Aoki, H. T. Miyazaki, H. Hirayama, K. Inoshita, T. Baba, K. Sakoda, N. Shinya, and Y. Aoyagi, "Microassembly of semiconductor three-dimensional photonic crystals.," *Nature materials*, vol. 2, pp. 117–21, Feb. 2003.

[18] J. Li, B. Jia, G. Zhou, and M. Gu, "Fabrication of three-dimensional woodpile photonic crystals in a PbSe quantum dot composite material.," *Optics express*, vol. 14, pp. 10740–5, Oct. 2006.

[19] A. Blanco, E. Chomski, S. Grabtchak, M. Ibisate, S. John, S. Leonard, C. Lopez, F. Meseguer, H. Miguez, J. Mondia, G. Ozin, O. Toader, and van Driel HM, "Large-scale synthesis of a silicon photonic crystal with a complete three-dimensional bandgap near 1.5 micrometres," *Nature*, vol. 405, pp. 437–40, May 2000.

[20] S. Ek, L. Stewart, M. Steel, J. Dawes, and M. Withford, "Artificial Opals for Photonic Crystal Devices," in *SPIE International Committee of Optics 21*, 2008.

[21] M. Notomi, "Manipulating light with strongly modulated photonic crystals," *Reports on Progress in Physics*, vol. 73, p. 096501, Sept. 2010.

[22] S. Combrié, *Etude et réalisation de structures en cristaux photoniques pour les applications de traitement du signal optique*. PhD thesis, 2006.

[23] A. Y. Petrov and M. Eich, "Zero dispersion at small group velocities in photonic crystal waveguides," *Applied Physics Letters*, vol. 85, no. 21, p. 4866, 2004.

[24] G. Jönsson and E. Nilsson, *Våglära och Optik*. Teach Support, 2002.

[25] T. Krauss, "Slow light in photonic crystal waveguides," *Journal of Physics D: Applied Physics*, vol. 40, p. 2666, 2007.

[26] E. Mizuta, H. Watanabe, and T. Baba, "All Semiconductor Low- Photonic Crystal Waveguide for Semiconductor Optical Amplifier," *Japanese Journal of Applied Physics*, vol. 45, no. No. 8A, pp. 6116–6120, 2006.

[27] T. Baba, "Slow light in photonic crystals," *Nature Photonics*, vol. 2, pp. 465–473, Aug. 2008.

[28] P. Colman, C. Husko, S. Combrié, I. Sagnes, C. Wong, and A. De Rossi, "Temporal solitons and pulse compression in photonic crystal waveguides," *Nature Photonics*, vol. 4, no. 12, pp. 862–868, 2010.

[29] M. Notomi, K. Yamada, a. Shinya, J. Takahashi, C. Takahashi, and I. Yokohama, "Extremely Large Group-Velocity

Dispersion of Line-Defect Waveguides in Photonic Crystal Slabs," *Physical Review Letters*, vol. 87, no. 25, pp. 1–4, 2001.

[30] X. Letartre, C. Seassal, C. Grillet, P. Rojo-Romeo, P. Viktorovitch, M. Le Vassor dâĂŹYerville, D. Cassagne, and C. Jouanin, "Group velocity and propagation losses measurement in a single-line photonic-crystal waveguide on InP membranes," *Applied Physics Letters*, vol. 79, no. 15, p. 2312, 2001.

[31] Y. A. Vlasov, M. Oboyle, H. F. Hamann, and S. J. Mcnab, "Active control of slow light on a chip with photonic crystal waveguides," *Nature*, vol. 438, pp. 65–69, 2005.

[32] L. V. Hau, S. E. Harris, Z. Dutton, and C. H. Behroozi, "Light speed reduction to 17 metres per second in an ultracold atomic gas," *Nature*, vol. 397, no. February, pp. 594–598, 1999.

[33] M. Phillips, H. Wang, I. Rumyantsev, N. Kwong, R. Takayama, and R. Binder, "Electromagnetically Induced Transparency in Semiconductors via Biexciton Coherence," *Physical Review Letters*, vol. 91, pp. 1–4, Oct. 2003.

[34] L. a. Coldren and S. W. Corzine, *Diode Lasers and Photonic Integrated Circuits*. 1995.

[35] A. Baca and C. Ashby, *Fabrication of GaAs Devices*. London: The institution of Electrical Engineers, 2005.

[36] A. Alian, G. Brammertz, C. Merckling, A. Firrincieli, W.-E. Wang, H. C. Lin, M. Caymax, M. Meuris, K. De Meyer, and M. Heyns, "Ammonium sulfide vapor passivation of In0.53Ga0.47As and InP surfaces," *Applied Physics Letters*, vol. 99, no. 11, p. 112114, 2011.

[37] S. L. Chuang, *Physics of Optoelectronic Devices*. 1995.

[38] E. S. Semenova, I. V. Kulkova, S. Kadkhodazadeh, M. Schubert, and K. Yvind, "Metal organic vapor-phase epitaxy of InAs/InGaAsP quantum dots for laser applications at 1.5 μm," *Applied Physics Letters*, vol. 99, no. 10, p. 101106, 2011.

[39] H. Zhu, Z. Wang, H. Wang, L. Cui, and S. Feng, "Uniformity enhancement of the self-organized InAs quantum dots," *Journal of Crystal Growth*, vol. 197, pp. 372–375, Feb. 1999.

[40] M. Loncar, T. Doll, and J. Vuckovic, "Design and fabrication of silicon photonic crystal optical waveguides," *Technology, Journal of*, vol. 18, no. 10, pp. 1402–1411, 2000.

[41] L. H. Frandsen, A. V. Lavrinenko, J. Fage-pedersen, and P. I. Borel, "Photonic crystal waveguides with semi-slow light and tailored dispersion properties," *Opt. Express*, vol. 14, no. 20, pp. 9444–9450, 2006.

[42] M. V. Kotlyar, T. Karle, M. D. Settle, L. OFaolain, and T. F. Krauss, "Low-loss photonic crystal defect waveguides in InP," *Applied Physics Letters*, vol. 84, no. 18, p. 3588, 2004.

[43] E. Schwoob, H. Benisty, C. Weisbuch, C. Cuisin, E. Derouin, O. Drisse, G. Duan, L. Legouezigou, O. Legouezigou, and F. Pommereau, "Enhanced gain measurement at mode singularities in InP-based photonic crystal waveguides," *Optics Express*, vol. 12, no. 8, pp. 1569–1574, 2004.

[44] F. Raineri, G. Vecchi, C. Cojocaru, A. Yacomotti, C. Seassal, X. Letartre, P. Viktorovitch, R. Raj, and A. Levenson, "Optical amplification in two-dimensional photonic crystals," *Applied Physics Letters*, vol. 86, p. 091111, 2005.

[45] O. Painter, "Two-Dimensional Photonic Band-Gap Defect Mode Laser," *Science*, vol. 284, no. 5421, pp. 1819–1821, 1999.

[46] B. Ellis, M. Mayer, G. Shambat, T. Sarmiento, J. Harris, E. Haller, and J. Vučković, "Ultralow-threshold electrically pumped quantum-dot photonic-crystal nanocavity laser," *Nature Photonics*, vol. 5, no. 5, pp. 297–300, 2011.

[47] K. Inoshita and T. Baba, "Room-Temperature Lasing Characteristics of Bend and Branch in Photonic Crystal Waveguide," *Japanese Journal of Applied Physics*, vol. 42, pp. 6887–6891, Nov. 2003.

[48] X. Ming-Xin, Z. Wan-Hua, Z. Wen-Jun, C. Wei, L. An-Jin, and W. Hai-Ling, "Slow Light Effect and Multimode Lasing in

a Photonic Crystal Waveguide Microlaser," *Chinese Physics Letters*, vol. 27, p. 024213, Feb. 2010.

[49] K. Kiyota, T. Kise, N. Yokouchi, T. Ide, and T. Baba, "Various low group velocity effects in photonic crystal line defect waveguides and their demonstration by laser oscillation," *Applied Physics Letters*, vol. 88, no. 20, p. 201904, 2006.

[50] K. Inoue, H. Sasaki, K. Ishida, Y. Sugimoto, N. Ikeda, Y. Tanaka, S. Ohkouchi, Y. Nakamura, and K. Asakawa, "InAs quantum-dot laser utilizing GaAs photonic-crystal line-defect waveguide.," *Optics express*, vol. 12, pp. 5502–9, Nov. 2004.

[51] J. Mø rk and T. R. Nielsen, "On the use of slow light for enhancing waveguide properties.," *Optics letters*, vol. 35, pp. 2834–6, Sept. 2010.

[52] J. Joannopoulos, S. Johnson, J. Winn, and R. Meade, *Photonic crystals: molding the flow of light*. 1995.

[53] K. Sakoda, *Optical Properties of Photonic Crystals*. 2001.

[54] S. Johnson and J. Joannopoulos, "Block-iterative frequency-domain methods for Maxwell's equations in a planewave basis," *Opt. Express*, vol. 8, no. 3, pp. 173–190, 2001.

[55] D. Gerace and L. C. Andreani, "Disorder-induced losses in photonic crystal waveguides with line defects.," *Optics letters*, vol. 29, pp. 1897–9, Aug. 2004.

[56] J. Grgić, J. Pedersen, S. Xiao, and N. Mortensen, "Group index limitations in slow-light photonic crystals," *Photonics and Nanostructures - Fundamentals and Applications*, vol. 8, pp. 56–61, May 2010.

[57] S. Hughes, L. Ramunno, J. Young, and J. Sipe, "Extrinsic optical scattering loss in photonic crystal waveguides: role of fabrication disorder and photon group velocity," *Physical review letters*, vol. 94, no. 3, p. 33903, 2005.

[58] N. Le Thomas, H. Zhang, J. Jágerská, V. Zabelin, R. Houdré, I. Sagnes, and a. Talneau, "Light transport regimes in slow

light photonic crystal waveguides," *Physical Review B*, vol. 80, pp. 1–8, Sept. 2009.

[59] A. Parini, P. Hamel, A. De Rossi, S. Combrie, N.-V.-Q. Tran, Y. Gottesman, R. Gabet, A. Talneau, Y. Jaouen, and G. Vadala, "Time-Wavelength Reflectance Maps of Photonic Crystal Waveguides: A New View on Disorder-Induced Scattering," *Journal of Lightwave Technology*, vol. 26, pp. 3794–3802, Dec. 2008.

[60] M. D. Settle, R. J. P. Engelen, M. Salib, a. Michaeli, L. Kuipers, and T. F. Krauss, "Flatband slow light in photonic crystals featuring spatial pulse compression and terahertz bandwidth.," *Optics express*, vol. 15, pp. 219–26, Jan. 2007.

[61] L. Andreani and D. Gerace, "Photonic-crystal slabs with a triangular lattice of triangular holes investigated using a guided-mode expansion method," *Physical Review B*, vol. 73, no. 23, p. 235114, 2006.

[62] S.-i. Takayama, H. Kitagawa, Y. Tanaka, T. Asano, and S. Noda, "Experimental demonstration of complete photonic band gap in two-dimensional photonic crystal slabs," *Applied Physics Letters*, vol. 87, no. 6, p. 061107, 2005.

[63] I. Vurgaftman, J. Meyer, and L. Ram-Mohan, "Band parameters for III-V compound semiconductors and their alloys," *Journal of applied physics*, vol. 89, no. 11, p. 5815, 2001.

[64] C. Monat, B. Corcoran, M. Ebnali-Heidari, C. Grillet, B. J. Eggleton, T. P. White, L. O'Faolain, and T. F. Krauss, "Slow light enhancement of nonlinear effects in silicon engineered photonic crystal waveguides.," *Optics express*, vol. 17, pp. 2944–53, Feb. 2009.

[65] N. A. Mortensen and S. Xiao, "Slow-light enhancement of Beer-Lambert-Bouguer absorption," *Applied Physics Letters*, vol. 90, no. 14, p. 141108, 2007.

[66] K. Kuroda, T. Sawada, T. Kuroda, K. Watanabe, and K. Sakoda, "Doubly enhanced spontaneous emission due to increased photon density of states at photonic band edge fre-

quencies," *Optics Express*, vol. 17, no. 15, pp. 13168–13177, 2009.

[67] Y. Chen, F. Wang, S. Ek, J. Jensen, O. Sigmund, and J. Mø rk, "Modelling of Active Semiconductor Photonic Crystal Waveguides and Robust Designs based on Topology Optimization," in *13'th International Conference on Transparent Optical Networks (ICTON), Stockholm, Sweden*, 2011.

[68] S. Ek, Y. Chen, E. S. Semenova, P. Lunnemann, K. Yvind, and J. Mø rk, "Slow-Light Enhancement of Spontaneous Emission in Active Photonic Crystal Waveguides," in *SPIE Photonics West, San Fransisco, California, USA*, 2012.

[69] W. Nakwaski, "Thermal conductivity of binary, ternary, and quaternary III-V compounds," *Journal of applied physics*, vol. 64, no. 1, pp. 159–166, 1988.

[70] K. Nozaki, S. Kita, and T. Baba, "Room temperature continuous wave operation and controlled spontaneous emission in ultrasmall photonic crystal nanolaser.," *Optics express*, vol. 15, pp. 7506–14, June 2007.

[71] M. Nomura, S. Iwamoto, K. Watanabe, N. Kumagai, Y. Nakata, S. Ishida, and Y. Arakawa, "Room temperature continuous-wave lasing in photonic crystal nanocavity," *Optics Express*, vol. 14, no. 13, pp. 6308–6315, 2006.

[72] H.-G. Park, S.-H. Kim, S.-H. Kwon, Y.-G. Ju, J.-K. Yang, J.-H. Baek, S.-B. Kim, and Y.-H. Lee, "Electrically driven single-cell photonic crystal laser.," *Science (New York, N.Y.)*, vol. 305, pp. 1444–7, Sept. 2004.

[73] M. H. Shih, M. Bagheri, A. Mock, S. J. Choi, J. D. OâĂŹBrien, P. D. Dapkus, and W. Kuang, "Identification of modes and single mode operation of sapphire-bonded photonic crystal lasers under continuous-wave room temperature operation," *Applied Physics Letters*, vol. 90, no. 12, p. 121116, 2007.

[74] H. Lindberg, M. Strassner, E. Gerster, J. Bengtsson, and A. Larsson, "Thermal Management of Optically Pumped

Long-Wavelength InP-Based Semiconductor Disk Lasers," *Quantum*, vol. 11, no. 5, pp. 1126–1134, 2005.

[75] S. Matsuo, A. Shinya, T. Kakitsuka, K. Nozaki, T. Segawa, T. Sato, Y. Kawaguchi, and M. Notomi, "High-speed ultracompact buried heterostructure photonic-crystal laser with 13 fJ of energy consumed per bit transmitted," *Nature Photonics*, vol. 4, no. 9, pp. 648–654, 2010.

[76] R. J. Hussey, R. Driad, G. I. Sproule, S. Moisa, J. W. Fraser, Z. R. Wasilewski, J. P. McCaffrey, D. Landheer, and M. J. Graham, "Thermal Oxidation of III-V Materials and Heterostructures," *Journal of The Electrochemical Society*, vol. 149, no. 10, p. G581, 2002.

[77] S. Bae, J. Kim, C. Park, and Y. Lee, "Characteristics of InAlAs/InP and InAlP/GaAs native oxides," *Solid-State Electronics*, vol. 50, no. 9-10, pp. 1625–1628, 2006.

[78] L. Ottaviano, E. Semenova, M. Schubert, K. Yvind, A. Armaroli, G. Bellanca, S. Trillo, T. N. Nguyen, M. Gay, L. Bramerie, and J.-c. Simon, "High-speed photodetectors in a photonic crystal platform," in *submitted to CLEO USA 2012*, vol. 4.

[79] N.-V.-Q. Tran, S. Combrié, and A. De Rossi, "Directive emission from high-Q photonic crystal cavities through band folding," *Physical Review B*, vol. 79, no. 4, pp. 1–4, 2009.

[80] T. P. White, L. C. Botten, C. Martijn de Sterke, K. B. Dossou, and R. C. McPhedran, "Efficient slow-light coupling in a photonic crystal waveguide without transition region.," *Optics letters*, vol. 33, pp. 2644–6, Nov. 2008.

[81] S. a. Schulz, L. O Faolain, D. M. Beggs, T. P. White, A. Melloni, and T. F. Krauss, "Dispersion engineered slow light in photonic crystals: a comparison," *Journal of Optics*, vol. 12, p. 104004, Oct. 2010.

[82] K. Kawaguchi, M. Ekawa, A. Kuramata, T. Akiyama, H. Ebe, M. Sugawara, and Y. Arakawa, "Fabrication of InAs quantum dots on InP(100) by metalorganic vapor-phase epitaxy for

1.55 μm optical device applications," *Applied Physics Letters*, vol. 85, no. 19, p. 4331, 2004.

[83] S. Anantathanasarn, R. Notzel, P. Vanveldhoven, F. Vanotten, T. Eijkemans, Y. Barbarin, T. Devries, E. Smalbrugge, E. Geluk, and E. Bente, "Stacking, polarization control, and lasing of wavelength tunable (1.55μm region) InAs/InGaAsP/InP (100) quantum dots," *Journal of Crystal Growth*, vol. 298, pp. 553–557, Jan. 2007.

[84] D. Franke, M. Moehrle, J. Boettcher, P. Harde, a. Sigmund, and H. Kuenzel, "Effect of metal organic vapor phase epitaxy growth conditions on emission wavelength stability of 1.55âĂĆμm quantum dot lasers," *Applied Physics Letters*, vol. 91, no. 8, p. 081117, 2007.

[85] Z. G. Lu, J. R. Liu, P. J. Poole, S. Raymond, P. J. Barrios, D. Poitras, G. Pakulski, P. Grant, and D. Roy-Guay, "An L-band monolithic InAs/InP quantum dot mode-locked laser with femtosecond pulses.," *Optics express*, vol. 17, pp. 13609–14, Aug. 2009.

[86] M. Schubert, *Coupled Photonic Crystal Cavity Array Laser*. PhD thesis, Technical University of Denmark, 2010.

[87] T. Chang, "Proximity effect in electron-beam lithography," *Journal of Vacuum Science and Technology*, vol. 12, no. 6, pp. 1271–1275, 1975.

[88] S. Lee and B. D. Cook, "PYRAMID-a hierarchical, rule-based approach toward proximity effect correction. I. Exposure estimation," *Semiconductor Manufacturing, IEEE*, vol. 11, no. 1, pp. 108–116, 1998.

[89] F. Pommereau, L. Legouezigou, S. Hubert, S. Sainson, J. Chandouineau, S. Fabre, G. Duan, B. Lombardet, R. Ferrini, and R. Houdre, "Fabrication of low loss two-dimensional InP photonic crystals by inductively coupled plasma etching," *Journal of applied physics*, vol. 95, no. 2004, p. 2242, 2004.

[90] P. Strasser, R. Wüest, F. Robin, D. Erni, and H. Jäckel, "Detailed analysis of the influence of an inductively coupled plasma reactive-ion etching process on the hole depth and

shape of photonic crystals in InP/ InGaAsP," *Journal of Vacuum Science & Technology B: Microelectronics and Nanometer Structures*, vol. 25, p. 387, 2007.

[91] D. Larsson, *Fabrication and characterization of low-noise monolithic mode-locked lasers*. PhD thesis, Technical University of Denmark, 2007.

[92] D. Flamm, V. Donnelly, and D. Ibbotson, "Basic chemistry and mechanisms of plasma etching," *Journal of Vacuum Science & Technology B: Microelectronics and Nanometer Structures*, vol. 1, no. 1, pp. 23–30, 1983.

[93] C. Gatzert, a. W. Blakers, P. N. K. Deenapanray, D. Macdonald, and F. D. Auret, "Investigation of reactive ion etching of dielectrics and Si in CHF3/O2 or CHF3/Ar for photovoltaic applications," *Journal of Vacuum Science & Technology A: Vacuum, Surfaces, and Films*, vol. 24, no. 5, p. 1857, 2006.

[94] U. Niggebrugge, M. Klug, and G. Garus, "A novel process for reactive ion etching on InP, using CH4/H2," in *Gallium arsenide and related compounds 1985. Proceedings*, vol. 79, pp. 367–372, International Symposium on Gallium Arsenide and Related Compounds 12, Karuizawa, Institute of Physics - Conference Series, 1985.

[95] S. McNevin, "Chemical etching of GaAs and InP by chlorine: The thermodynamically predicted dependence on Cl2 pressure and temperature," *Journal of Vacuum Science & Technology B: Microelectronics and Nanometer Structures*, vol. 4, no. 5, pp. 1216–1226, 1986.

[96] T. Hayes, M. Dreisbach, P. Thomas, W. Dautremont-Smith, and L. Heimbrook, "Reactive ion etching of InP using CH4/H2 mixtures: Mechanisms of etching and anisotropy," *Journal of Vacuum Science & Technology B: Microelectronics and Nanometer Structures*, vol. 7, no. 5, pp. 1130–1140, 1989.

[97] A. Carter, B. Thomas, and D. Morgan, "Dry etching of GaAs and InP for optoelectronic devices," *Optoelectronics, IEE Proceedings J*, vol. 136, pp. 2–5, 1989.

[98] L. Henry and C. Vaudry, "Novel process for integration of optpelectronic devices using reactive ion etching without chlorinated gas," *Electronics Letters*, vol. 23, no. 24, pp. 1253–1254, 1987.

[99] U. Khankhoje, S.-h. Kim, B. Richards, J. Hendrickson, J. Sweet, J. Olitzky, G. Khitrova, H. Gibbs, and A. Scherer, "Modelling and fabrication of GaAs photonic-crystal cavities for cavity quantum electrodynamics," *Nanotechnology*, vol. 21, p. 065202, 2010.

[100] D. Wiersma, "The physics and applications of random lasers," *Nature Physics*, vol. 4, no. 5, pp. 359–367, 2008.

[101] J. Li, T. White, L. Faolain, A. Gomez-Iglesias, and T. Krauss, "Systematic design of flat band slow light in photonic crystal waveguides," *Optics*, vol. 16, pp. 6227–6232, 2008.

[102] P. Colman, *Circuits nanophotoniques pour le traitement tout-optique du signal*. PhD thesis, l'Université Paris, 2011.

[103] B. Adamowicz, M. Miczek, S. Arabasz, and H. Hasegawa, "Rigorous analysis of photoluminescence efficiency for characterisation of electronic properties of InP (1 0 0) surfaces," *Vacuum*, vol. 67, no. 1, pp. 3–10, 2002.

[104] J. Hvam, "Direct recording of opticalâĂŘgain spectra from ZnO," *Journal of Applied Physics*, vol. 49, no. 6, pp. 3124–3126, 1978.

[105] M. KoÌĹrbl, a. GroÌĹning, H. Schweizer, and J. L. Gentner, "Gain spectra of coupled InGaAsP/InP quantum wells measured with a segmented contact traveling wave device," *Journal of Applied Physics*, vol. 92, no. 5, p. 2942, 2002.

[106] R. Costa, a. Melloni, and M. Martinelli, "Bandpass resonant filters in photonic-crystal waveguides," *IEEE Photonics Technology Letters*, vol. 15, pp. 401–403, Mar. 2003.

[107] P. Anderson, "Absence of diffusion in certain random lattices," *Physical Review*, vol. 109, no. 5, p. 1492, 1958.

[108] S. Smolka, H. Thyrrestrup, L. Sapienza, T. B. Lehmann, K. R. Rix, L. S. Froufe-Pérez, P. D. García, and P. Lodahl,

"Probing the statistical properties of Anderson localization with quantum emitters," *New Journal of Physics*, vol. 13, p. 063044, June 2011.

[109] J. Topolancik, B. Ilic, and F. Vollmer, "Experimental Observation of Strong Photon Localization in Disordered Photonic Crystal Waveguides," *Physical Review Letters*, vol. 99, pp. 2–5, Dec. 2007.

[110] T. Suhr, N. Gregersen, K. Yvind, and J. Mø rk, "Modulation response of nanoLEDs and nanolasers exploiting Purcell enhanced spontaneous emission," *Optics express*, vol. 18, pp. 11230– 11241, 2010.

[111] D. Mori and T. Baba, "Dispersion-controlled optical group delay device by chirped photonic crystal waveguides," *Applied Physics Letters*, vol. 85, no. 7, p. 1101, 2004.

[112] T. Baba, "Slow light engineering in photonic crystals," *Journal of Physics D: Applied Physics*, vol. 40, pp. 2659–2665, 2007.

[113] R. Hao, E. Cassan, H. Kurt, X. Le Roux, D. Marris-Morini, L. Vivien, H. Wu, Z. Zhou, and X. Zhang, "Novel slow light waveguide with controllable delay-bandwidth product and utra-low dispersion.," *Optics express*, vol. 18, pp. 5942–50, Mar. 2010.

[114] P. Borel, a. Harpø th, L. Frandsen, M. Kristensen, P. Shi, J. Jensen, and O. Sigmund, "Topology optimization and fabrication of photonic crystal structures.," *Optics express*, vol. 12, pp. 1996–2001, May 2004.

[115] R. Stainko and O. Sigmund, "Tailoring dispersion properties of photonic crystal waveguides by topology optimization," *Waves in Random and Complex Media*, vol. 17, pp. 477–489, Oct. 2007.

[116] F. Wang, J. Jensen, and O. Sigmund, "Robust topology optimization of photonic crystal waveguides with tailored dispersion properties," *JOSA B*, vol. 28, no. 3, pp. 387–397, 2011.

[117] H. Altug, D. Englund, and J. Vukovi, "Ultrafast photonic crystal nanocavity laser," *Nature Physics*, vol. 2, no. 7, pp. 484–488, 2006.

[118] Y. Akahane, T. Asano, and B. Song, "High-Q photonic nanocavity in a two-dimensional photonic crystal," *Nature*, vol. 425, no. October, pp. 4–7, 2003.

[119] T. Baba, D. Mori, K. Inoshita, and Y. Kuroki, "Light Localizations in Photonic Crystal Line Defect Waveguides," *IEEE Journal of Selected Topics in Quantum Electronics*, vol. 10, pp. 484–491, May 2004.

[120] M. Francardi, L. Balet, a. Gerardino, N. Chauvin, D. Bitauld, L. H. Li, B. Alloing, and a. Fiore, "Enhanced spontaneous emission in a photonic-crystal light-emitting diode," *Applied Physics Letters*, vol. 93, no. 14, p. 143102, 2008.

[121] S. Chakravarty, P. Bhattacharya, and Z. Mi, "Electrically injected quantum-dot photonic crystal microcavity light-emitting arrays with air-bridge contacts," *Photonics Technology Letters, IEEE*, vol. 18, no. 24, pp. 2665–2667, 2006.

[122] M. Heuck, S. r. Blaaberg, and J. Mø rk, "Theory of passively mode-locked photonic crystal semiconductor lasers," *Optics Express*, vol. 18, p. 18003, Aug. 2010.

[123] M. Schubert, T. Suhr, S. Ek, E. S. Semenova, J. M. Hvam, and K. Yvind, "Lambda shifted photonic crystal cavity laser," *Applied Physics Letters*, vol. 97, no. 19, p. 191109, 2010.

[124] R. Braive, S. Barbay, I. Sagnes, A. Miard, I. Robert-Philip, and A. Beveratos, "Transient chirp in high-speed photonic-crystal quantum-dot lasers with controlled spontaneous emission," *Optics letters*, vol. 34, no. 5, pp. 554–556, 2009.

[125] U. Mohideen, R. Slusher, F. Jahnke, and S. Koch, "Semiconductor microlaser linewidths," *Physical review letters*, vol. 73, no. 13, pp. 1785–1788, 1994.

[126] J. Grgi, J. R. r. Ott, F. Wang, O. Sigmund, A.-p. Jauho, J. Mø rk, and N. A. Mortensen, "Fundamental limitations to

gain enhancement in periodic media and waveguides," *submitted november 2011*, 2011.

[127] H. Benisty and C. Sotomayor-Torres, "Intrinsic mechanism for the poor luminescence properties of quantum-box systems," *Physical Review B*, vol. 44, no. 19, pp. 8–11, 1991.

[128] J. Urayama, T. Norris, J. Singh, and P. Bhattacharya, "Observation of Phonon Bottleneck in Quantum Dot Electronic Relaxation," *Physical Review Letters*, vol. 86, pp. 4930–4933, May 2001.

[129] R. Heitz, H. Born, F. Guffarth, O. Stier, a. Schliwa, a. Hoffmann, and D. Bimberg, "Existence of a phonon bottleneck for excitons in quantum dots," *Physical Review B*, vol. 64, pp. 1–4, Nov. 2001.

[130] X. Li and H. Nakayama, "Phonon bottleneck in quantum dots: Role of lifetime of the confined optical phonons," *Physical Review B*, vol. 59, no. 7, pp. 5069–5073, 1999.

[131] W. Schäfer and M. Wegener, *Semiconductor optics and transport phenomena*. Springer, 2002.

[132] Z. Wang, *Self-assembled quantum dots*. 2008.

[133] S. Rodt, R. Seguin, a. Schliwa, F. Guffarth, K. Pötschke, U. Pohl, and D. Bimberg, "Size-dependent binding energies and fine-structure splitting of excitonic complexes in single InAs/GaAs quantum dots," *Journal of Luminescence*, vol. 122-123, pp. 735–739, Jan. 2007.

[134] K. L. Hall, G. Lenz, E. P. Ippen, and G. Raybon, "Heterodyne pump - probe technique for time-domain studies of optical nonlinearities in waveguides.," *Optics letters*, vol. 17, p. 874, June 1992.

[135] J. Mø rk and A. Mecozzi, "Response function for gain and refractive index dynamics in active semiconductor waveguides," *Applied Physics Letters*, vol. 65, no. 14, p. 1736, 1994.

[136] K. Hall, G. Lenz, A. Darwish, and E. Ippen, "Subpicosecond gain and index nonlinearities in InGaAsP diode lasers," *Optics communications*, vol. 111, no. 5-6, pp. 589–612, 1994.

[137] M. Poel and J. r. M. Hvam, "Ultrafast dynamics of quantum-dot semiconductor optical amplifiers," *Journal of Materials Science: Materials in Electronics*, vol. 18, pp. 51–55, Mar. 2007.

[138] J. Mø rk and J. Mark, "Physics and Simulation of Optoelectronic Devices III," in *SPIE*, pp. vol. 2399, pp. 146–159, 1995.

[139] M. van der Poel, J. Mø rk, A. Somers, A. Forchel, J. P. Reithmaier, and G. Eisenstein, "Ultrafast gain and index dynamics of quantum dash structures emitting at 1.55 μm," *Applied Physics Letters*, vol. 89, no. 8, p. 081102, 2006.

[140] A. J. Zilkie, J. Meier, P. W. E. Smith, M. Mojahedi, J. S. Aitchison, P. J. Poole, C. N. Allen, P. Barrios, and D. Poitras, "Femtosecond gain and index dynamics in an InAs/InGaAsP quantum dot amplifier operating at 1.55 microm.," *Optics express*, vol. 14, pp. 11453–9, Nov. 2006.

[141] A. J. Zilkie, J. Meier, M. Mojahedi, P. J. Poole, P. Barrios, D. Poitras, T. J. Rotter, C. Yang, A. Stintz, K. J. Malloy, P. W. E. Smith, and J. S. Aitchison, "Carrier Dynamics of Quantum-Dot, Quantum-Dash, and Quantum-Well Semiconductor Optical Amplifiers Operating at 1.55 Âţm," *IEEE Journal of Quantum Electronics*, vol. 43, pp. 982–991, Nov. 2007.

[142] P. Lunnemann, *Slow Light and Pulse Propagation in Semiconductor Waveguides*. PhD thesis, Technical University of Denmark, 2009.